Synthesis Strategies for High Entropy Nanoparticles

Linlin Yang, Ren He*, Jiali Chai, Xueqiang Qi, Qian Xue, Xiaoyu Bi, Jing Yu, Zixu Sun, Lu Xia, Kaiwen Wang, Nilotpal Kapuria, Junshan Li, Ahmad Ostovari Moghaddam, and Andreu Cabot*

L. L. Yang, R. He, J. L. Chai, X. Y. Bi, J. Yu, A. Cabot

Catalonia Energy Research Institute - IREC, Sant Adrià de Besòs, 08930, Barcelona, Spain.

E-mail: renhe@irec.cat and acabot@irec.cat

L. L. Yang, R. He, J. L. Chai, X. Y. Bi

Enginyeria Electrònica i Biomèdica Facultat de Física, Universitat de Barcelona, 08028, Barcelona, Spain.

X. Q. Qi, Q. Xue

College of Chemistry and Chemical Engineering, Chongqing University of Technology, 400054, Chongqing, China.

Z. X. Sun

Key Lab for Special Functional Materials of Ministry of Education, School of Materials Science and Engineering, Henan University, Kaifeng, 475004, Henan, China.

L. Xia, K. W. Wang

ICFO – Institut de Ciències Fotòniques, The Barcelona Institute of Science and Technology, 08860 Castelldefels, Barcelona, Spain.

N. Kapuria

Indiana University, Department of Chemistry 800 E. Kirkwood, CHEM Bloomington, IN 47405-7102, United States of America.

J. S. Li

Institute for Advanced Study, Chengdu University, 610106, Chengdu, China.

A. O. Moghaddam

Department of Materials Science, Physical and Chemical Properties of Materials, South Ural State University, 76 Lenin Ave, 454080, Chelyabinsk, Russia.

A. Cabot

ICREA, Pg. Lluis Companys 23, 08010, Barcelona, Catalonia, Spain.

ABSTRACT

Nanoparticles (NPs) of high entropy materials (HEMs) have attracted significant attention due to their versatility and wide range of applications. HEM NPs can be synthesized by fragmenting bulk HEMs or disintegrating and recrystallizing them. Alternatively, directly producing HEMs in NP form from atomic/ionic/molecular precursors presents a significant challenge. A widely adopted strategy involves thermodynamically driving HEM NP formation by leveraging the entropic contribution but incorporating strategies to limit NP growth at the elevated temperatures used for maximizing entropy. A second approach is to kinetically drive HEM NP formation by promoting rapid reactions of homogeneous reactant mixtures or using highly diluted precursor dissolutions. Additionally, experimental evidence suggests that enthalpy plays a significant role in driving HEM NP formation processes at moderate temperatures, with the high energy cost of generating additional surfaces and interfaces at the nanoscale stabilizing the HEM phase. This review critically assesses the various synthesis strategies developed for HEM NP preparation, highlighting key illustrative examples and offering insights into the underlying formation mechanisms. Such insights are critical for fine-tuning experimental conditions to achieve specific outcomes, ultimately enabling the effective synthesis of optimized generations of these advanced materials for both current and emerging applications across various scientific and technological fields.

Keywords: high entropy alloy, high entropy material, nanoparticle, nanocrystal

Outlook

1. Introduction

High-entropy materials (HEMs) are an emerging and distinct class of compounds typically characterized by the presence of five or more principal elements randomly distributed within the structure. The term 'high-entropy alloy' (HEA) was introduced by Yeh et al. in 2004 when rationalizing the potential stabilization of a solid solution through the entropic contribution to the system's total free energy.[1] The authors postulated that in a solid solution with a sufficient number of elements, the entropy term could be large enough to counterbalance the enthalpy of formation for all possible intermetallic phases. They estimated that combining five elements in equiatomic ratios would be sufficient to overcome the enthalpy of formation for most intermetallic phases. This condition, which was from the beginning relaxed to at least 5 elements with ratios in the range between 5 and 35 at.%, has been empirically observed not to consistently result in the formation of a solid solution. Nevertheless, this criterion has been widely accepted and adopted as the definition for HEAs and later HEMs. Interestingly, while entropy has been shown to play a limited role in stabilizing some HEAs and influencing their functional properties, the catchy term that Yeh et al. brilliantly introduced has persisted and is widely used today to describe a broad array of systems and concepts. These include some counterintuitive categories, such as high-entropy carbons, polymers, single-atom materials, and even materials containing only two or three randomly distributed elements.[2]

HEAs challenged conventional alloy design principles and thus experienced slow development in the early 2000s. However, during the mid-2010s, the field of HEAs experienced a surge in recognition and attention. This was marked by the development of multiple novel alloy compositions, the comprehensive characterization of their properties, and the identification of new applications. Beyond HEAs, other high-entropy compounds began to attract interest, including high-entropy oxides (HEOs),[3] high-entropy phosphides (HEPs),[4] high-entropy sulfides (HESs),[5] high-entropy nitride (HENs),[6] and high-entropy borides (HEBs),[7] among many others.[2c, 8] Simultaneously, significant theoretical and experimental efforts have been dedicated to the investigation of the fundamental science behind HEMs, focused on elucidating their formation and stabilization mechanisms,[9] as well as identifying the factors that contribute to their distinctive functional properties.[10]

The high configurational entropy of HEMs was the first and most prominent characteristic identified in these materials. This high entropy promotes a homogeneous atomic arrangement with a single solid crystal structure, such as body-centered cubic (BCC), face-centered cubic (FCC), or hexagonal close-packed (HCP),[11] reducing the thermodynamic driving force for phase segregation. HEMs are also characterized by sluggish atomic diffusion, contributing to their exceptional mechanical, structural, and chemical stability. The atomic size mismatch among different elements

and the resulting local disorder in the crystal cause subtle lattice distortions, which are influenced by the specific composition and proportions of elements. These lattice distortions impede the movement of dislocations, leading to solid solution strengthening.[12] Additionally, lattice distortion affects the material's response to stress and strain, significantly increasing the strength, and ductility and raising the crack-arresting capability.[13] Moreover, the lattice distortion impacts the electronic properties, particularly the density of states near the Fermi level and the degree of electron localization/delocalization. Lattice distortion can also introduce defects that act as a source or trap of charge carriers, thereby affecting the overall electronic behavior. Beyond these factors, within the so-called 'cocktail effect' a wide range of properties arising from the virtually unlimited potential combinations of elements in HEMs have been encompassed. As a result, these materials exhibit enhanced functional properties, including relatively low thermal conductivity,[14] resistance to wear, oxidation, corrosion, and irradiation,[15] and unique magnetic,[16] electronic,[17] and catalytic performance.[4b, 13c, 18] Furthermore, owing to their complex compositions, HEM properties are also highly tolerant to impurities, which facilitates their production from recycled elements.

Owing to these enhanced performances, HEMs have been applied in diverse fields over the past decade, including catalysis,[13c, 19] electrocatalysis[20], photocatalysis[21], batteries,[22] supercapacitors[23], photovoltaics,[24] memory devices,[25] biomedical applications such as bone implants and coatings,[26] thermoelectrics[14, 27], aerospace,[28] coatings and surface treatments,[29] and nuclear reactors,[30] among many others. In several of these applications, high surface area materials are essential to maximize interactions with the surrounding media. Additionally, the availability of the HEMs in the form of small particles is particularly advantageous for processing. As a result, the development of HEM nanoparticles (NPs) has become a major focus in advanced materials science and engineering communities.[31]

However, producing HEM particles with dimensions in the nanometer-scale regime is a challenging task. Typically, high temperatures are required to maximize the entropic contribution, which is considered essential for stabilizing the multi-component mixtures in HEMs. On the other hand, high temperatures also enhance atomic diffusion and crystal growth, which is detrimental to the synthesis of NPs with controlled parameters. As a result, some of the conventional methods for synthesizing NPs may not be suitable for producing HEM NPs or may require significant optimization, particularly when aiming for precise control over the size, shape, phase, and composition of the HEM NPs. Given their unique atomic compositions, understanding the formation mechanisms associated with different synthesis methods is crucial for tailoring experimental conditions to achieve desired outcomes. Several reviews have been published on the synthesis, properties, and applications of

HEMs across various fields, [2, 8, 31-32] offering readers in-depth insights into specific areas of interest.

In this review, we critically and comprehensively map the main synthesis approaches developed for producing HEM NPs, offering illustrative examples and insights into the underlying formation mechanisms (**Figure 1)**. These methods are categorized based on strategies for achieving HEM formation and stability, preventing phase segregation, as well as controlling particle size, and limiting growth. The majority of the approaches discussed have been successfully applied or hold potential for application across a wide range of HEM systems, demonstrating their versatility and broad applicability in different contexts. Given the inherent complexity in distinguishing between kinetically-driven and thermodynamically-driven HEM formation, the presented examples are classified according to the intended approach. In practice, some synthesis methods employ multiple strategies simultaneously to control NP growth, and in many cases, the actual mechanism behind the formation and stabilization of the HEM phase may differ from the intended or presumed one.

We begin by considering two main categories: top-down and bottom-up approaches. Within the bottom-up methods for directly producing HEM NPs from atomic, ionic, or molecular precursors, we distinguish three primary mechanisms that drive the formation and stability of the HEM phase: (i) entropy, (ii) kinetics, and (iii) enthalpy. Entropy-driven approaches use high-temperature conditions typical of bulk HEM synthesis while limiting particle size by restricting reactant availability. This can be achieved by: (i) extremely shortening reaction times, (ii) immobilizing precursors on high-surface-area supports or within templates before high-temperature reaction, (iii) localizing energy input to confine reactions, or (iv) using milling processes to disrupt crystal growth during reaction. An alternative to the high-temperature processing typically used to enhance the entropic contribution for thermodynamically driven HEM growth is to kinetically drive the process. Kinetic approaches focus on rapidly reacting elements to prevent stabilization into thermodynamically preferred phases. Successful HEM NP formation requires all reagents to react simultaneously, directly forming the HEM phase while avoiding unwanted intermediates. This can be achieved through: i) pre-condensing a random element dispersion into precursor particles followed by moderate temperature crystallization; ii) rapidly triggering reactions via high temperatures, reactive precursors, plasma, or charge injection; iii) using highly diluted precursor solutions to minimize interactions of affine species. The third strategy involves the enthalpy-driven formation of HEM NPs, capitalizing on the substantial impact of surface and interface energies on the overall energy of a NP. As particle size decreases, these energies become increasingly dominant, reaching a critical radius where forming a single-phase HEM NP is more energetically favorable than multiple phases, owing to the high energy cost of generating additional surfaces and interfaces at the nanoscale. Finally, the conclusions and

prospects section highlights key future research directions to advance our understanding of HEM formation mechanisms, properties, and performance, and to expand their applications. These include improving insights into atomic-scale composition, controlling defects and strain, ensuring stability under operational conditions, mastering growth mechanisms, and using high-throughput computational techniques for screening the stability and functional properties across the vast range of possible HEMs.

Figure 1. Schematic overview of the different approaches for synthesizing HEM NPs.

2. Top-down strategies

A straightforward strategy to obtain HEM NPs, when bulk HEMs produced by conventional high-temperature solid-state reaction strategies are available, is to break down the bulk material into smaller pieces or disintegrate and reconstruct it into NPs. The composition and crystal structure of the HEM NPs produced through these top-down approaches generally remain similar to the original bulk material, although some variations may occur, particularly due to chemical contamination and

structural defects introduced during the processing. Additionally, certain elements might be lost during the disintegration process. Top-down methods generally allow high NP production throughput and yields. As a drawback, top-down approaches rely on the use of high-temperature processes to produce the precursor bulk HEM and require additional energy input to break it, which strongly reduces the overall energy efficiency of the process. All top-down methods for producing HEM NPs begin with the synthesis of a bulk HEM target or precursor. From this common starting point, two main pathways emerge for reducing the particle size to the nanoscale. The first pathway involves the direct physical or chemical fragmentation of the bulk HEM into smaller particles, which typically preserves the material's original crystal structure and composition. The second pathway involves the ablation or disintegration of the bulk HEM, followed by its rapid reconstruction into smaller particles, often in a high-energy environment, to maintain the random distribution of elements characteristic of HEMs.

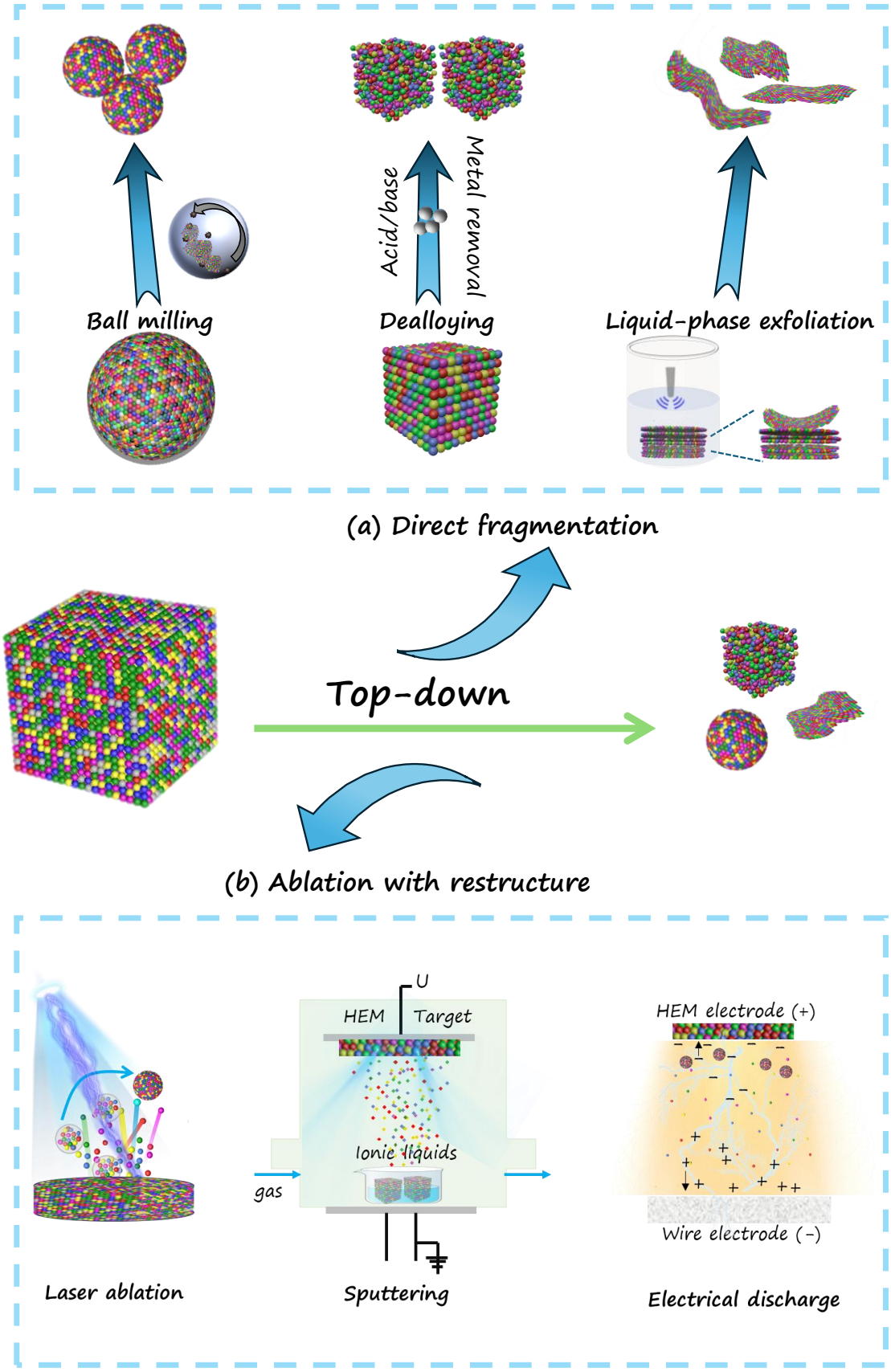

Figure 2. Scheme of the top-down approaches to produce HEM NPs. (a) Fragmentation methods. (b) Ablation methods.

2.1. Fragmentation

The simplest strategy to produce HEM NPs from bulk HEMs is to fragment the material into smaller pieces. This can be achieved through various methods (**Figure 2**): grinding or milling, which breaks the material without controlling the fragmentation planes; exfoliating along specific weak planes to produce NPs with a nanoplate or nanosheet morphology; or selectively dealloying or etching the HEM. Although grinding/milling and selective dealloying can both be used for exfoliation, herein we distinguish these methods based on their impact on composition. We consider milling and exfoliation approaches to fragment the HEM while preserving its original composition, albeit with the potential introduction of impurities. In contrast, dealloying/etching methods intentionally remove one or more elements from the bulk HEM, resulting in HEM nanostructures with altered compositions.

2.1.1. Milling

Several milling strategies can be used to break bulk HEMs into NPs. Ball milling typically involves the use of a cylindrical container where balls are allowed to impact the material to be ground. The final particle size can be to some extent controlled by adjusting the milling time and the size and hardness of the balls, among other parameters. In jet milling, high-velocity jets of gas or steam are used to accelerate particles in a chamber. The accelerated particles collide with each other and are thereby reduced in size. This method is often used for heat-sensitive materials, as it does not generate significant heat. In the same direction, cryomilling involves the use of low temperatures to facilitate the material crushing by making it more brittle while at the same time preventing phase and compositional modifications, e.g. oxidation, triggered by the heat generated during the process.

Numerous types of HEM NPs have been prepared by this top-down approach. For instance, AuAgCuPdPt HEA ingot produced by arc melting and casting method was separated into smaller pieces and cryomilled until finely dispersed NPs.[33] CuAgAuPtPd HEA NPs were obtained by cryomilled HEA ingots in a liquid nitrogen-cooled (at -160 ± 10 °C) environment for 6 h.[34] FeCrMnNiCo and FeCrMnVAl were also produced by arc melting with post cryomilling process. **Figure 3a** shows the schematic of a custom-built cryomill system using a tungsten carbide ball.[35] Kumar et al. used this system to produce $Fe_{0.2}Cr_{0.2}Mn_{0.2}Ni_{0.2}Co_{0.2}$ HEA NPs with the same FCC crystal phase as the ingot and sizes down to 4 nm (**Figures 3b-3d**). In the first step, a diamond saw was used to break the HEA ingot into smaller pieces that were inserted in the milling chamber. This was maintained at a low temperature by inserting liquid nitrogen and it was continuously purged with Ar to further protect the powder from oxidation during milling. As described by the authors, in their HEA NP preparation process using cryomilling, the grain refinement involved three-stages, flattening of particles (sheet formation), fracturing of sheets, and steady-state NP formation (**Figure 3e**). The

flattened powder particles were slightly cold welded but the bond strength of the cold welds was very low and was easy to break. The low temperature increased HEA brittelity and reduced the dynamic recovery of the HEAs, thus accelerating the fracturing of the particles, while also contributing to reduced oxidation. By reducing the milling duration, contamination and oxidation were also reduced.

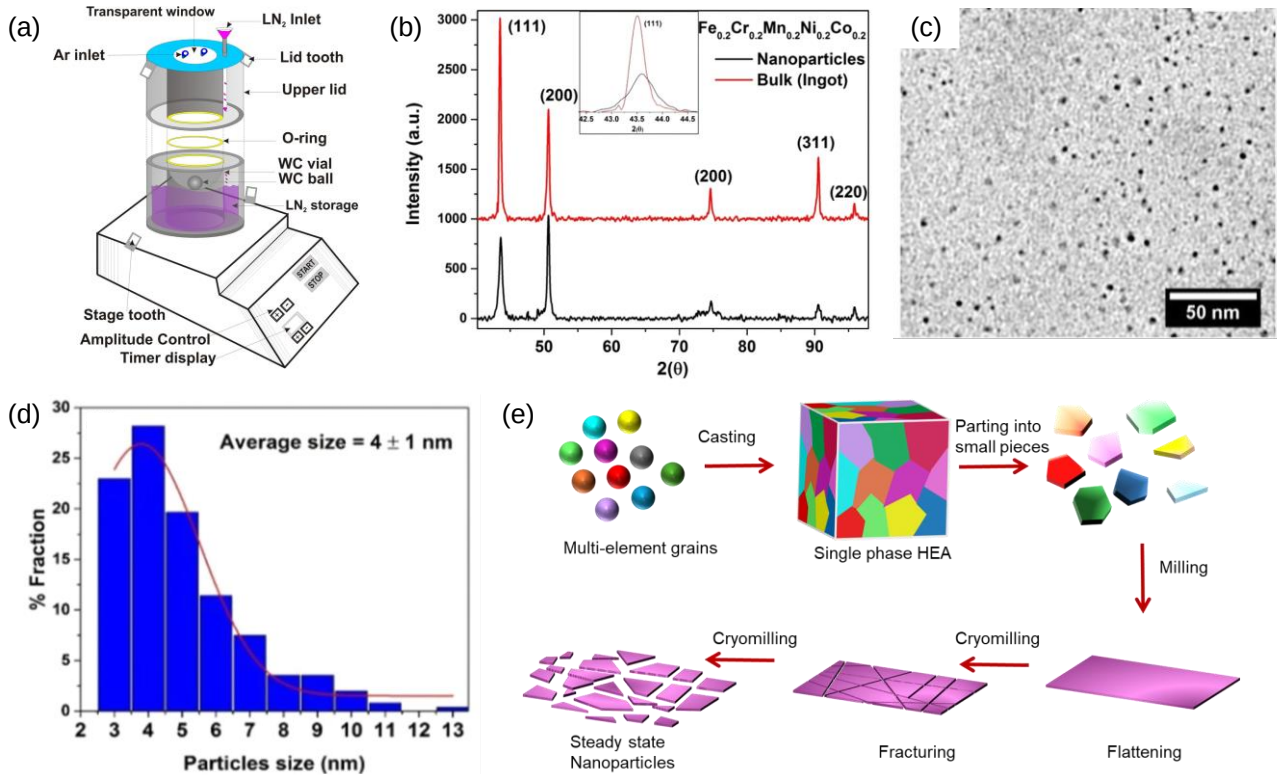

Figure 3. (a) Schematic of a custom-built single tungsten carbide ball cryomill. (b) X-ray diffraction (XRD) pattern of a $Fe_{0.2}Cr_{0.2}Mn_{0.2}Ni_{0.2}Co_{0.2}$ HEA ingot and the derived NPs, showing a single-phase FCC structure. (c) Transmission electron microscopy (TEM) bright field image of NPs stabilized using oleylamine. (d) Size distribution histogram of HEA NPs. Reproduced with permission.[35] Copyright 2018, Springer Science Business Media, LLC, part of Springer Nature. (e) Schematic diagram of the formation of HEA NPs by cryomilling.

2.1.2. Exfoliation

Exfoliation is a widely used strategy to produce nanosheets of layered materials such as graphene, which typically rely on mechanically or chemically separating particularly weakly bonded material layers. This strategy can be used to produce HEM nanosheets from bulk HEMs with a layered crystal phase. At the laboratory level, mechanical exfoliation is frequently accomplished using adhesive tape to peel off layers from a bulk crystal with a weak (Van der Waals) interlayer. Although the Scotch tape method is a straightforward approach to preparing 2D materials for research purposes, it suffers from obvious disadvantages such as low yield, incontrollable layer thickness, and high reliance on the experimenters, reducing its reliability, controllability, and reproducibility. Shear exfoliation and ball milling are higher throughput mechanically-aided strategies to selectively break the materials

through particular crystallographic planes. Besides, liquid phase exfoliation involves dispersing the bulk material in a liquid medium and using ultrasonication (or vigorous shaking) to exfoliate the material into nanosheets. The choice of solvent is crucial as it needs to provide a balance between interacting with the material to promote exfoliation and not re-aggregating the exfoliated nanosheets. Chemical exfoliation is based on the use of chemicals to weaken the forces holding the layers of the bulk material together, allowing them to be easily separated into thinner layers. This can be achieved through intercalation, where molecules or ions are inserted between the layers of the material, or by using solvents that interact with the surface of the material to separate the layers. Electrochemical exfoliation uses an electric current to drive the exfoliation process. The material is used as an electrode in an electrolyte solution, and the application of current causes ions from the electrolyte to intercalate into the material, leading to exfoliation[36].

As an example, Ying et al. synthesized a series of 17 van der Waals layered HEMs, named HEXs in analogy with the MAX phases used to produce MXenes, including dichalcogenides, halides, and phosphorus trisulfides.[37] These layered materials were easily exfoliated to produce HEM nanosheets with the thinnest thicknesses of 2.5 nm. They found that it is the comparable electronegativity rather than the ionic radii that permits the acquisition of the single phase by analysis of the 17 types of HEMs.[37] Qu et al used a liquid-phase exfoliation technique to exfoliate the bulk HES within N-methyl pyrrolidine solution for 24 h under sonication and produced 2D HES nanosheets with a thickness of 3 nm.[38] As shown in **Figure 4**, the synthesized MoWReMnCrS HES nanosheets displayed a structure consistent with the 2H-MoS_2 phase and showed homogenous element distribution.

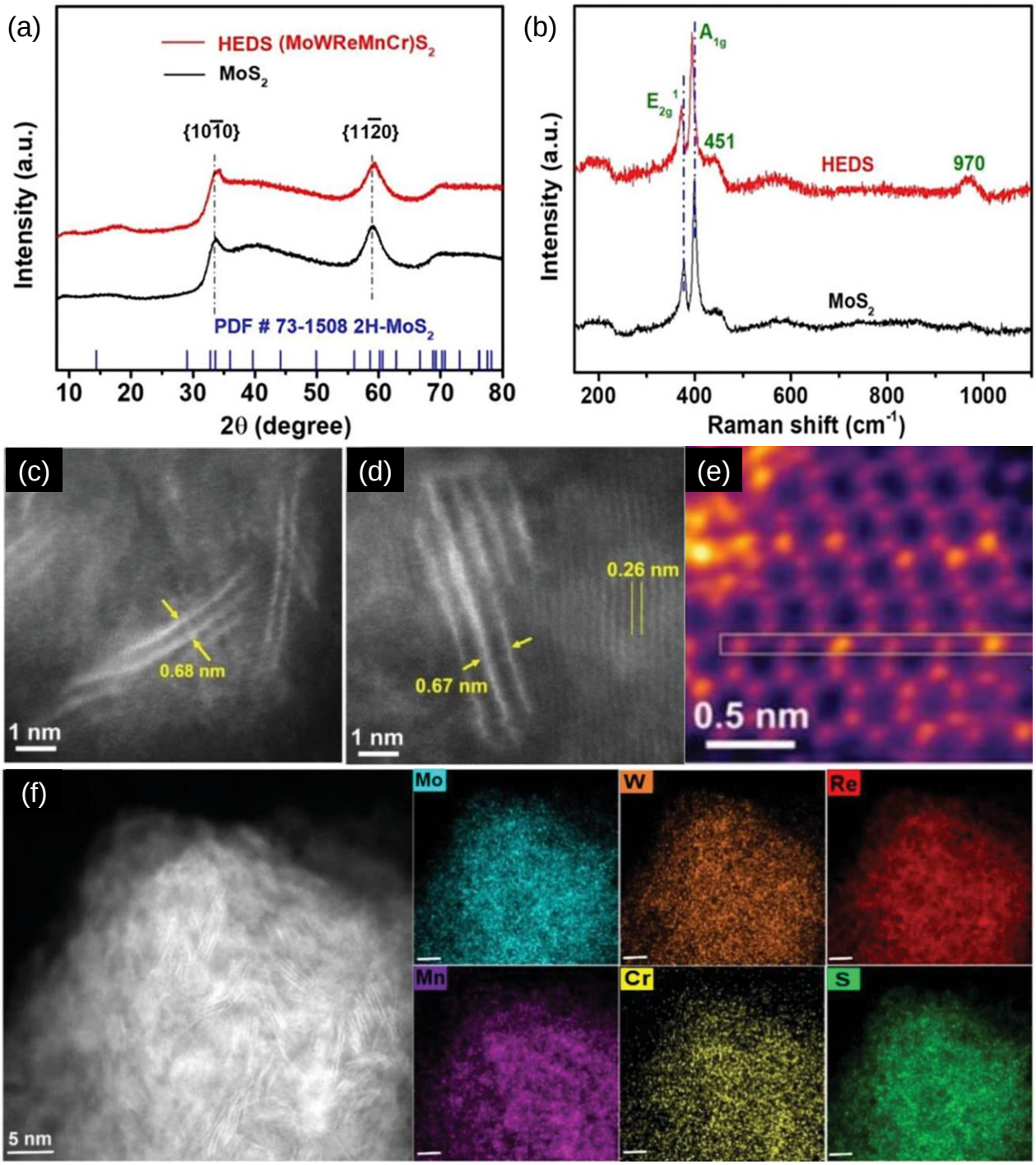

Figure 4. (a) XRD pattern and (b) Raman spectra of MoS_2 and MoWReMnCrS HES nanosheets. (c, d) High-angle annular dark field-scanning TEM (HAADF-STEM) images showing the interlayer distances between atomic planes and (e) planar view atomic structure of a MoWReMnCrS HES nanosheet. The inset in (e) shows the variation in pixel intensity along the area marked in the green box. (f) STEM image and energy dispersive X-ray spectroscopy (EDS) mappings of different elements in MoWReMnCrS HES nanosheets. Reproduced with permission.[38] Copyright 2023, Advanced Science published by Wiley-VCH GmbH.

2.1.3. Dealloying/etching

HEM NPs, generally with nanosheet morphology, can be also produced through the selective dissolution or etching of one or more elements from the bulk HEM, breaking it down into smaller

pieces while retaining the remaining composition. This process exploits differences in the electrochemical redox potential of the constituent elements, or their reactivity and chemical affinity with particular species. Thus the dealloying/etching typically takes place in a solution under an applied potential or in the presence of corrosive chemicals such as acids, or species that exhibit affinity to particular elements to drive their solvation.[39] This strategy is particularly effective with HEAs that contain noble metals such as Ir, Rh, Ru, Ag, Au, and Pt owing to their relatively high chemical stability. Conversely, active transition metals like Co, Fe, Ti, and Mn are prone to oxidation, forming oxides or hydroxides during dealloying in alkaline aqueous solutions for instance.[40] Therefore, careful control of these active metals is necessary when employing the dealloying method to produce HEM nanostructures.

A prototypical case of selective etching of one element to produce HEM nanosheets is that of high entropy MXenes from the selective etching of the A element (e.g. Al, Si, Ga, Sn) from a high entropy MAX phase.[41] As an example, $TiVNbMoC_3$ and $TiVCrMoC_3$ 2D high entropy MXene were synthesized by Nemani et al.[42] from the HF etching of a high entropy TiVNbMoAlC MAX phase produced by annealing a mixture of the metals at 1600 °C for 4 h (**Figure 5**). As a result, accordion-like high entropy MXene NPs were obtained. To further delaminate the exfoliated high-entropy MXenes into few-layer or single-layer 2D MXene nanosheets, the powders were further treated with tetramethylammonium hydroxide (TMAOH). To avoid using the toxic and dangerous HF, Yang's group used a similar process but using an HCl/LiF mixture to etch the Al species in the synthesized high entropy MAX phase to get the TiVZrNbTaC MXenes.[43]

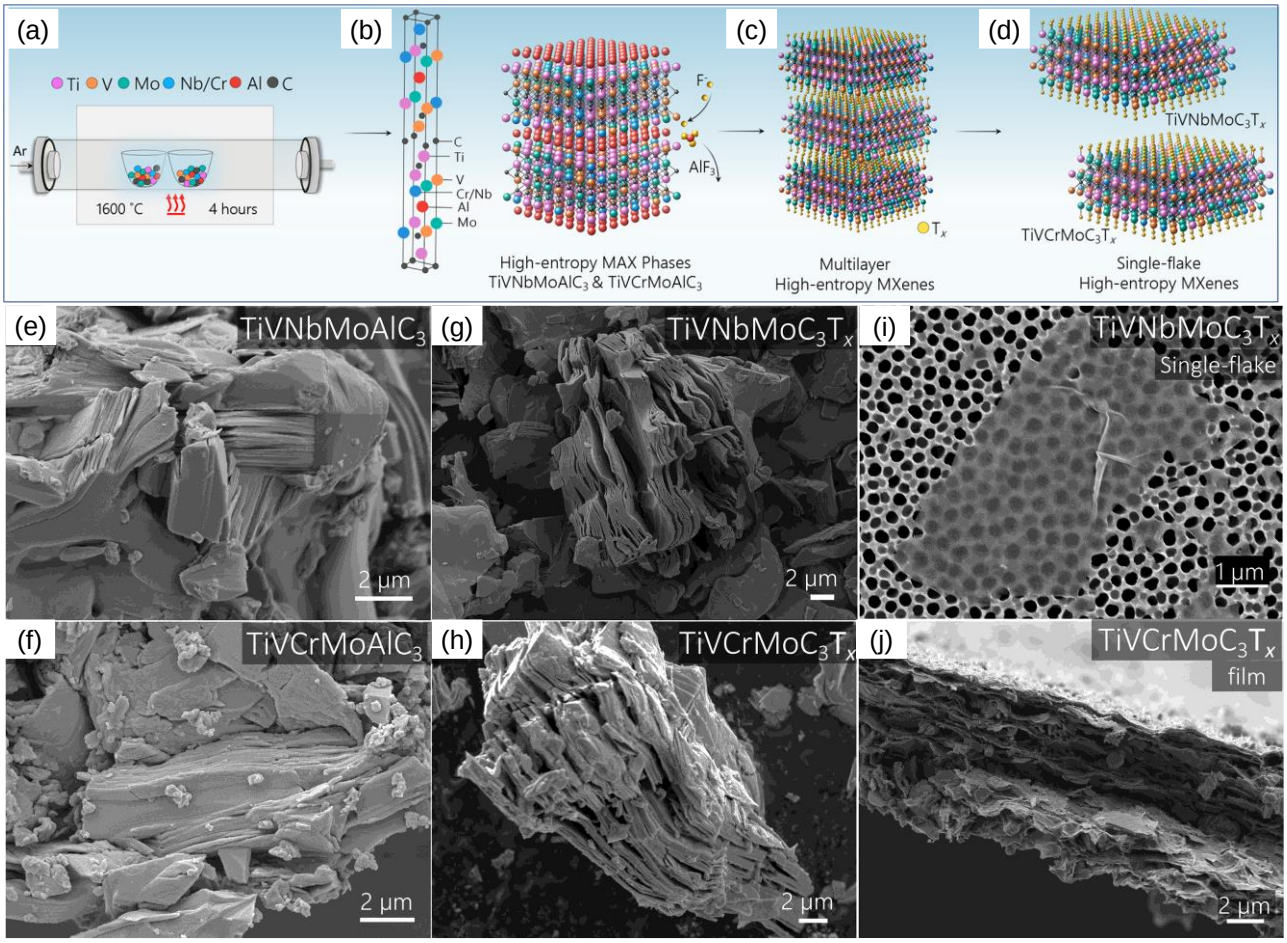

Figure 5. Schematic of the synthesis of high-entropy MAX and MXenes. (a) Reactive sintering of high-entropy MAX phases. (b) MAX phase unit cell (left) of $M_1M_2M_3M_4AlC_3$. The synthesized MAX phases in an M_4AlC_3 MAX structure (right). (c) Selective etching of the Al layers by HF acid to synthesize multilayer high-entropy MXenes. The surface terminations on the basal planes of MXenes (T_x) are shown in yellow. (d) Delamination of multilayer MXenes is completed via organic molecule intercalants, which leads to the formation of single flakes of high-entropy MXenes $TiVNbMoC_3T_x$ and $TiVCrMoC_3T_x$. (e, f) Scanning electron microscope (SEM) micrographs of high-entropy MAX and MXenes for (e) $TiVNbMoAlC_3$ and (f) $TiVCrMoAlC_3$. (g, h) Etched multilayer MXene powders of (g) $TiVNbMoC_3T_x$ and (h) $TiVCrMoC_3T_x$ with accordion-like morphologies. (i) Single flake of $TiVNbMoC_3T_x$ MXene on an alumina substrate. (j) Vacuum-assisted filtered film of $TiVCrMoC_3T_x$ MXene. Reproduced with permission.[42] Copyright 2021, American Chemical Society.

The dealloying strategy can also be employed to produce nanostructured and nanoporous HEMs beyond nanosheets from the sacrificial removal of specific elements in non-layered HEMS.[44] As an example, Jin et. al synthesized AlNiCoRuMo HEO/HEA nanowires through a de-alloying strategy.[44b] The metal powers of Ni, Co, and Ru were first melted using an induction-melting furnace under Ar protection, and then they were melted again with another Mo metal powders and a higher amount of Al powders in quartz and then injected into a rotating copper roller to produce the alloy strip. As shown in **Figure 6**, the obtained powders showed two phases of $Al_3NiCoRuMo$ and pure Al phase in the form of nanowires. Then, the obtained alloy strip was chemically etched in 0.5 M NaOH solutions to selectively remove most aluminum and produce the nanostructured HEA powders. During this

dealloying process, the pure Al phase was totally removed and spinel oxides were formed on the surface of the HEA. The obtained AlNiCoRuMo HEO/HEA solid nanowires were rather rugged and contained ultrafine nanopores/nanoholes.

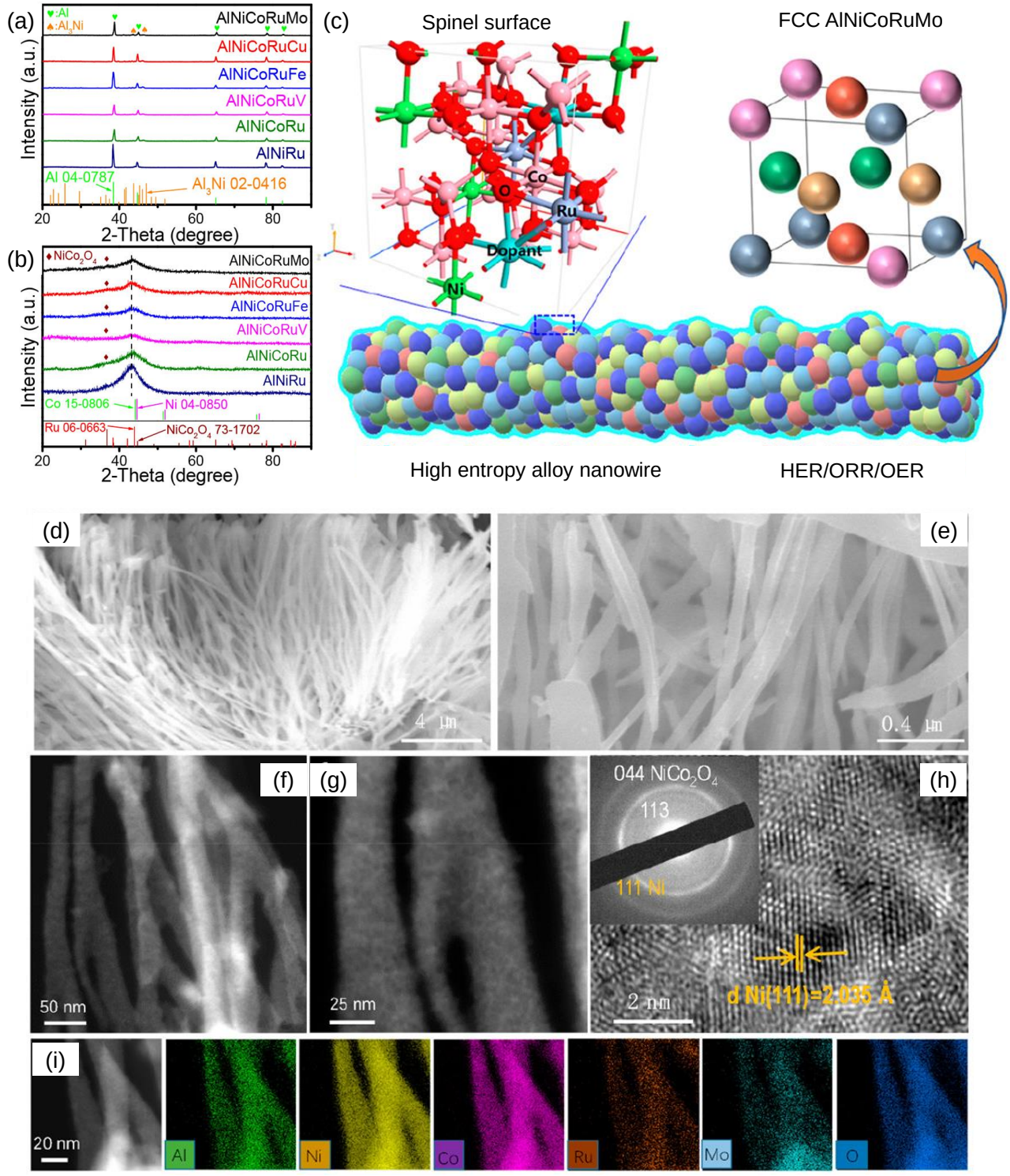

Figure 6. (a, b) XRD patterns of the precursor alloys before (a) and after (b) etching in 0.5 M NaOH solution. The standard positions of Al, Al_3Ni, Ni, Co, Ru, and $NiCo_2O_4$ are included for comparison. (c) The spinel crystal structure of the synthesized AlNiCoRuMo nanowires. (d, e) SEM, (f, g) HAADF-STEM, (h) high-resolution TEM (HRTEM), and (i) STEM-EDS mapping images of the

dealloyed AlNiCoRuMo nanowires. Reproduced with permission.[44b] Copyright 2020, American Chemical Society.

2.2. Ablation

Ablation strategies involve disintegrating a target bulk HEM into atoms or clusters by applying a physical shock, and then rapidly reconstructing it into a nanostructured HEM with the same or similar composition as the target material. Ablation strategies are widely recognized as a promising method to synthesize HEM NPs because of their high energy density and rapid heating/cooling process, which can effectively prevent phase separation during bulk HEM processing. These strategies include electrical discharge ablation using an electric arc, laser ablation that uses an electromagnetic pulse, and sputtering or ion beam ablation using ions to break the precursor bulk HEM into little pieces (**Figure 2**). The process must maintain the random element distribution characteristic of the HEM. Therefore, either moderate energies should be used to avoid generating secondary phases, or high temperatures should be reached to preserve the high entropic term that a priori stabilizes the HEM phase.

2.2.1. Electrical discharge ablation

Electrical discharge ablation strategies involve generating an electric arc or sparks between two electrodes made of the HEM to be ablated into NPs.[45] The intense heat from the process, often reaching temperatures of several thousand degrees Celsius, vaporizes the HEM from the electrodes. The vaporized material, comprising atoms, ions, or clusters, rapidly cools down and condenses into NPs as it moves away from the high-temperature region. The NPs are subsequently collected either on filters, a liquid medium, or a solid substrate, depending on the desired application and subsequent processing needs. This technique can be used to produce a wide range of materials, including metallic alloys and ceramics, and can be performed in either a vacuum, inert, or reactive gas environment. NPs produced through this method are known for their high purity, assuming a high-purity target is used, though they can exhibit a wide size distribution. Spark discharge, while similar to arc discharge, differs in that the temperature at the spark point is high but more localized and overall lower. Spark discharge is known for producing NPs with a narrower size distribution compared to arc discharge and is considered more controllable.

As an example, Niu et al. synthesized sub-10 nm (MoWVNbTa)C NPs using the electrical discharge ablation method (**Figure 7a**).[45] The bulk (MoWVNbTa)C served as the positive electrode, with a Mo wire as the negative electrode. The process involved plasma discharge generating temperatures above 10,000 °C, melting and vaporizing the bulk material's surface, forming expanding bubbles that rapidly quenched in dielectric liquid to create HEM NPs (**Figure 7b)**. The vaporization and quenching cycle occurred 2,000–500,000 times per second, resulting in 4 nm HEM NPs with

dense surface defects due to the non-equilibrium conditions (**Figures 7c-h**). The NPs retained the FCC structure of the bulk material. Similarly, Wu et al. synthesized 20 nm CoCrFeNiPt and $CoFeNiCr_{0.5}Pd_{0.8}$ HEA NPs via spark discharge using HEA electrodes.[46] The process involved etching, evaporation, and ejection of material through 50 μs direct current pulses from a 500 W power supply, followed by recondensation in cold water containing polyvinylpyrrolidone (PVP) to prevent agglomeration. The preferential evaporation of Co, Cr, Fe, and Ni over higher-boiling-point Pt highlighted the challenge of achieving uniform elemental distribution when constituent elements have differing boiling points.

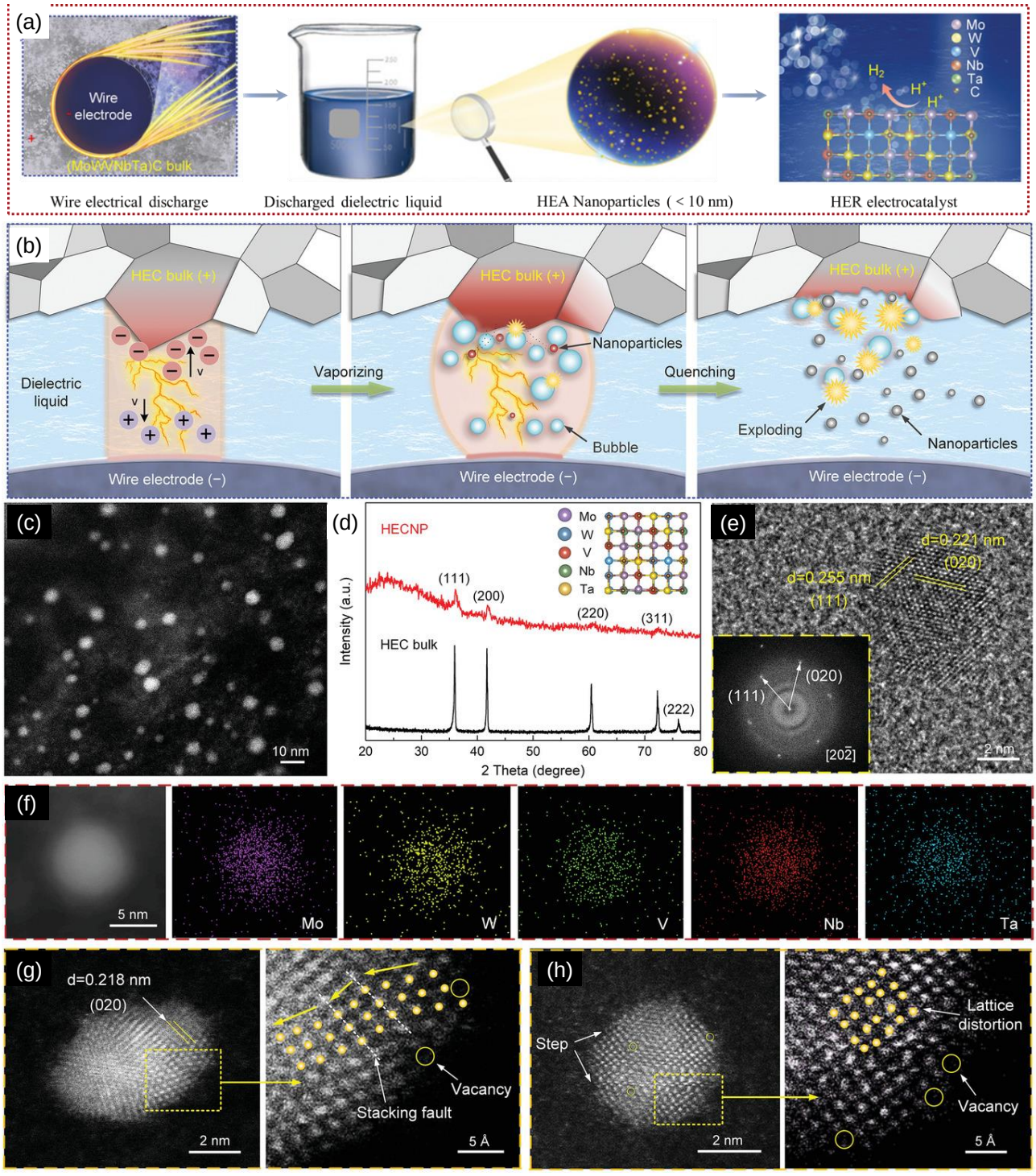

Figure 7. (a) Scheme of the process used to produce HEM NPs by electrical discharge ablation. (b) Cartoon of the formation mechanism of the NPs. Red and grey represent the NP at high temperatures and after quenching, respectively. (c) HAADF-STEM image of the (MoWVNbTa)C NPs. (d) XRD pattern of (MoWVNbTa)C bulk and NPs. The inset shows a schematic illustration of the elemental distribution in the lattice. (e) HRTEM image of (MoWVNbTa)C NPs and its corresponding selected area electron diffraction (SAED) pattern. (f) HAADF-STEM image and corresponding elemental mapping. (g, h) HAADF images of (MoWVNbTa)C NPs and their local enlarged views. Reproduced with permission.[45] Copyright 2022, Wiley-VCH GmbH.

2.2.2. Laser ablation

The laser ablation method for producing HEM NPs uses ultrashort, high-power laser pulses to

dissociate a bulk HEM into small pieces. NPs are generated in a gaseous or a liquid environment and are collected with filters, in liquids, or on top of a substrate. In a gaseous environment, the laser targets a small area of the target surface, heating it to generate a vapor plume that reaches temperatures up to tens of thousands of K and pressures of 2-15 GPa.[47] The plume rapidly expands, generating a pressure shockwave and cooling down in a nanosecond time scale. During this ultrarapid cooling, the ablated material condenses, allowing HEM NPs to nucleate and grow. The swift process kinetically stabilizes the HEM phase. In a liquid environment, stronger confinement of the expanding plasma plume takes place, and higher temperatures, pressures, and densities are reached within the generated cavitation bubble. Besides, the intense energy of the laser also heats the surrounding liquid, potentially initiating chemical reactions between the plume plasma and the heated liquid, thus adding complexity to the NP formation process.[48]

As an example, Waag et al. synthesized 3 g of colloidal CoCrFeMnNi HEA NPs in ethanol by laser ablating a HEA target of identical composition.[49] As depicted in **Figure 8**, the process began with the generation of a plume through laser irradiation. This was followed by the formation of a cavitation bubble due to the ablation of hot atoms, ions, and clusters from the HEA target, which then underwent a rapid cooling process. Ultimately, the cavitation bubble collapsed, releasing the HEA NPs into the liquid solution. While the CoCrFeMnNi NPs displayed a crystalline FCC phase and a uniform elemental distribution, they exhibited varied average sizes, in the range from 8 to 90 nm. The authors attributed these size variations to different particle formation mechanisms: smaller NPs formed from nucleation and condensation within a low-density mix of ablated metal species and supercritical liquid, while larger NPs originated from a dynamic molten layer on the target's surface. Jahangiri et al. noted that NP size and morphology could be controlled by adjusting laser parameters such as power, frequency repetition, and ablation rate, as well as by the ionic effects of the solvent. For instance, in experiments with HfNbTaTiZr HEA NPs synthesized using a femtosecond laser (120 fs), higher ablation fluence resulted in larger NPs due to increased nuclei formation.[50] Additionally, the choice of solvent impacted the NPs' size and distribution, with water producing larger and more variably sized NPs compared to ethanol and hexane.[50]

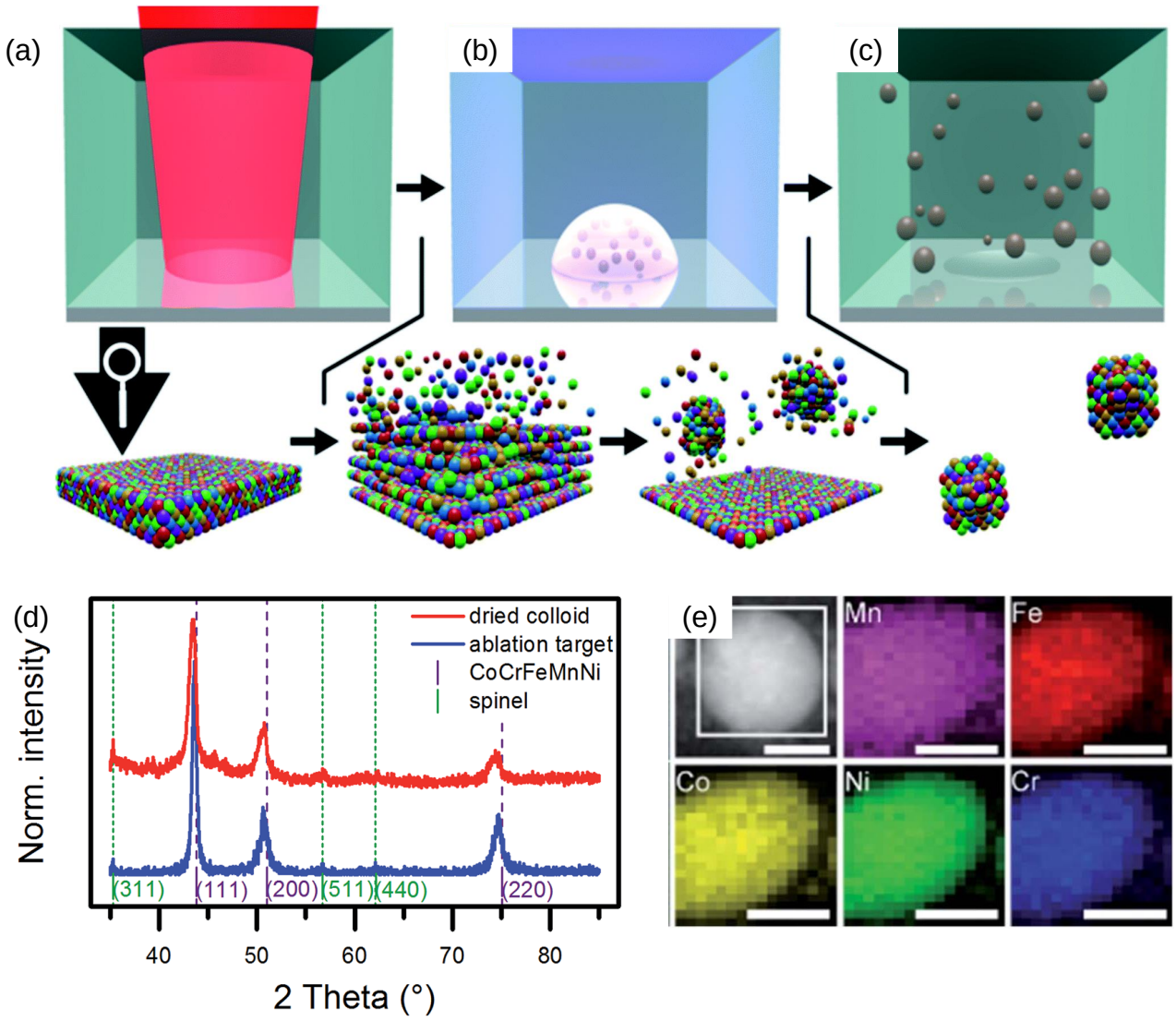

Figure 8. Scheme of the synthesis process by laser irradiation in liquid solution. The synthesis method consisted of the following stages: (a) ultrashort-pulsed laser irradiation of the bulk HEA target. (b) The atomization/ionization of the bulk causes the formation of a plume, and subsequent nucleation and condensation of the ablated matter in the vapor phase of the liquid. (c) The colloidal HEA NPs electrostatically stabilized in ethanol. (d) XRD of the ablation target (blue line) and a dried colloid produced in ethanol (red line). (e) STEM image and elemental maps of Co, Cr, Fe, Mn, and Ni for a single NP. The scale bar is 25 nm. Reproduced with permission [49] from CC- BY.4.0. open access publications.

2.2.3. Sputtering

Sputtering is a widely used physical vapor deposition technique for producing thin films. It involves bombarding a target with high-energy ions, causing atoms to eject from the target and form a plasma, which then condenses on a substrate. The atoms then condense on a substrate to create a film. Recently, this method has been adapted to synthesize NPs within an ionic liquid environment. Ionic liquids, known for their low vapor pressures, act as a medium for the nucleation and growth of the NPs and as stabilizer controlling their size and shape.

As an example of the application of this strategy for the synthesis of HEM NPs, Garzón-Manjón

et al. produced CrMnFeCoNi NPs in a 1-butyl-3-methylimidazolium bis(trifluoromethylsulfonyl)imide ([Bmim][Tf]2N) ionic liquid through conventional direct current magnetron sputtering and high-power impulse magnetron sputtering (HiPIMS) techniques using a CrMnFeCoNi HEA target.[51] Amorphous CrMnFeCoNi NPs were initially produced by direct current magnetron sputtering and were transformed into BCC and FCC phases upon electron beam irradiation and post-heating processes in vacuum. In contrast, 3.2 ± 0.5 nm BCC CrMnFeCoNi NPs could be directly obtained through HiPIMs due to their high plasma density and a high ionization fraction of the sputtered species (**Figure 9a**). Despite using targets with equiatomic ratios, the NPs' composition from direct current sputtering varied due to the ionic liquid's surface barrier effects. HiPIMS, generating higher energy species with an ion energy distribution up to 100 eV, overcame this barrier, producing NPs with a composition closer to the target's equiatomic ratio. By adjusting HiPIMS' pulse parameters, the energy and flux impacting NP nucleation, microstructure, and crystallization processes can be controlled. Furthermore, the authors investigated how the properties of ionic liquids, such as molecular chain length and structure, impact the catalytic performance of the obtained CrMnFeCoNi NPs for oxygen reduction reaction.[52] They found that sputtered atoms could alter the hydrogen bonding network within the ionic liquid, leading to variations in electrostatic and van der Waals interactions. These changes result in diverse NP growth mechanisms, yielding different crystal structures and sizes (**Figure 9b**).

Sputtering was also used by Wang et al. to produce HEA nanosheets using a polymer surface buckling-enabled exfoliation (PSBEE) method.[53] As shown in **Figure 9c**, the process begins with the preparation of a polyvinyl alcohol (PVA) hydrogel through 3D printing. This gel features surface striations aligned with the printing direction, which are then smoothed out using a hot press process. Subsequently, a thin film of a HEA, e.g. FeCoNiCrNb and ZrCuAlNi, is deposited onto the surface of the PVA hydrogel via sputtering from a bulk HEA target. After deposition, the composite is immersed in water, causing the PVA to swell. This swelling leads to the exfoliation of the 2D HEA film, which then floats in the water. The resulting HEA nanosheets are up to 50 nm thick with lateral dimensions reaching 10 mm (**Figure 9d-g**).

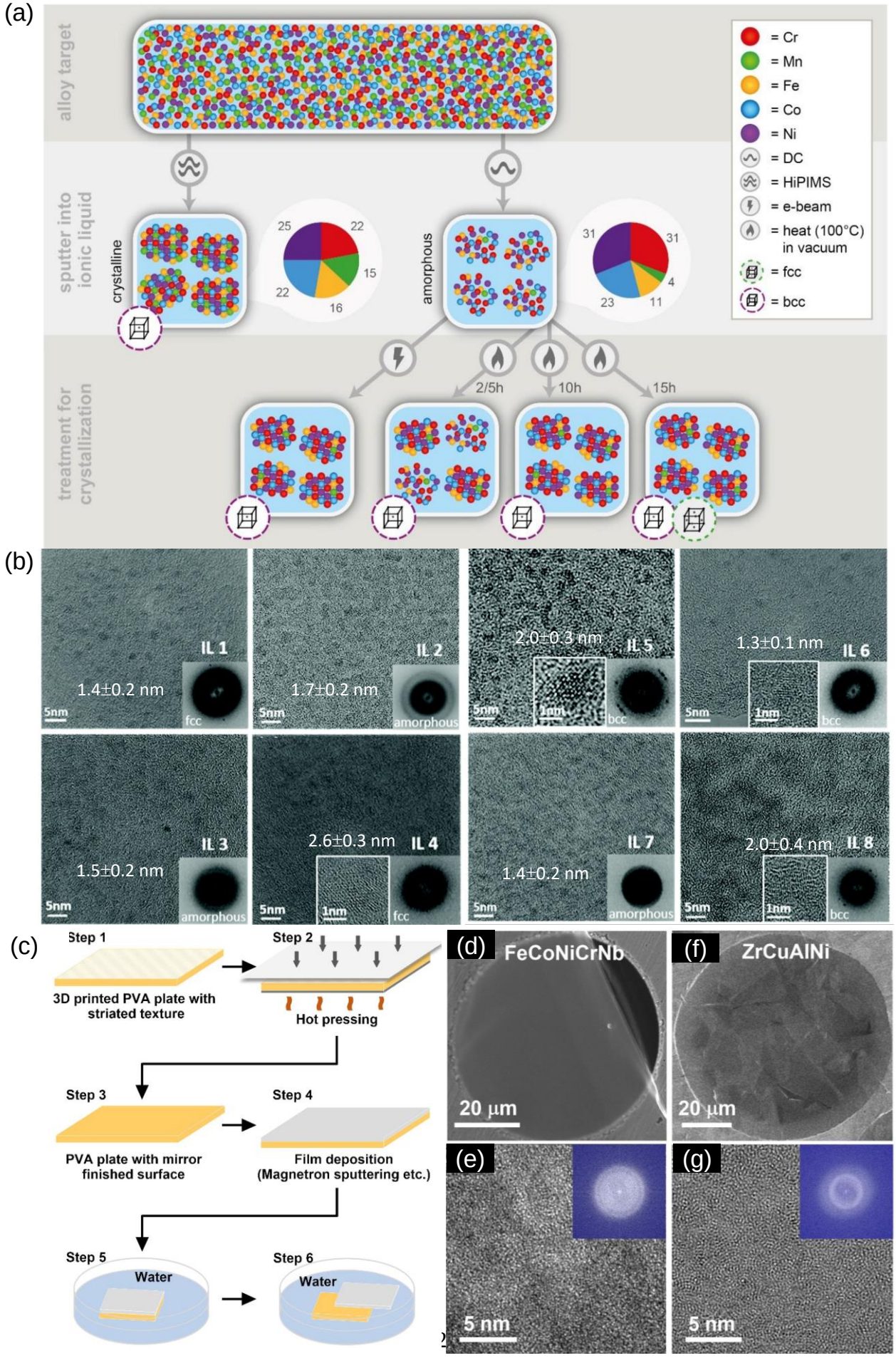
(a)
alloy target
sputter into ionic liquid
crystalline
amorphous
= Cr
= Mn
= Fe
= Co
= Ni
= DC
= HiPIMS
= e-beam
= heat (100°C) in vacuum
= fcc
= bcc
25
22
15
16
22
31
31
4
23
11
treatment for crystallization
2/5h
10h
15h
(b)
IL 1
1.4±0.2 nm
fcc
IL 2
1.7±0.2 nm
amorphous
2.0±0.3 nm
IL 5
bcc
1.3±0.1 nm
IL 6
bcc
IL 3
1.5±0.2 nm
amorphous
2.6±0.3 nm
IL 4
fcc
IL 7
1.4±0.2 nm
amorphous
2.0±0.4 nm
IL 8
bcc
5nm
1nm
(c)
Step 1
3D printed PVA plate with striated texture
Step 2
Hot pressing
Step 3
PVA plate with mirror finished surface
Step 4
Film deposition (Magnetron sputtering etc.)
Step 5
Water
Step 6
Water
(d)
FeCoNiCrNb
20 μm
(f)
ZrCuAlNi
20 μm
(e)
5 nm
(g)
5 nm

Figure 9. (a) Schematic overview of the different routes used to synthesize amorphous and crystalline multinary CrMnFeCoNi NPs through conventional direct current magnetron sputtering and HiPIMS techniques. Reproduced with permission [51] from CC- BY.4.0. open access publications. (b) HRTEM images of CrMnFeCoNi NPs sputtered in 8 different ionic liquids. The insets show the zoom-in on the crystalline NPs and the fast Fourier transform (FFT) patterns with the deduced crystal structure. Reproduced with permission [52] from CC- BY.4.0. open access publications. (c) Synthesis of 2D metals with the method of PSBEE. (d, f) SEM images of FeCoNiCrNd (d) and ZrCuAlNi (f) film. (e, g) HRTEM images and FFT pattern of FeCoNiCrNd (e) and ZrCuAlNi (g) film. Reproduced with permission.[53] Copyright 2020, Elsevier Ltd.

3. Bottom-up

Bottom-up methods directly produce HEM NPs through the reaction of ionic, atomic, or molecular species. These approaches are generally more energy efficient than top-down methods, as they usually involve fewer steps and leverage the shorter-range atomic order inherent in NPs, thus avoiding the substantial energy required to produce and subsequently break down bulk materials. However, a key challenge in the bottom-up synthesis of HEM NPs lies in balancing the *a priori* conflicting requirements for HEM phase formation and NP size stabilization.

Achieving a stable HEM phase often requires high temperatures to maximize the entropic contribution, while producing NPs with tuned particle size demands moderate temperatures to restrict atomic diffusion and limit crystal growth. Indeed, NPs are inherently metastable: they are susceptible to dissolution when their radii fall below a critical size, yet are prone to grow uncontrollably when they exceed that threshold. To restrict such growth, it is essential to manage the supply of reactants to the NPs, minimize Ostwald ripening by limiting atomic diffusion, and prevent NP aggregation and coalescence by inhibiting particle interactions. Therefore, selecting the appropriate high-temperature conditions that promote HEM phase formation while simultaneously restricting NP growth requires a delicate balance. Beyond high-temperature processes that focus on entropy-driven formation and stabilization of HEM phases, the synthesis of HEM NPs can also be kinetically driven at lower temperatures. These kinetically driven NPs are stabilized by the high energy barrier required for full redistribution of the constituent atoms. Additionally, the high energy cost of generating the additional surfaces and interfaces associated with the segregation of multiple phases may play a significant role in both the synthesis and stabilization of HEM NPs. Therefore, three general bottom-up strategies can be distinguished for producing HEM NPs, depending on whether HEM phase formation is governed by entropy, kinetics, or enthalpy (**Figure 10**).

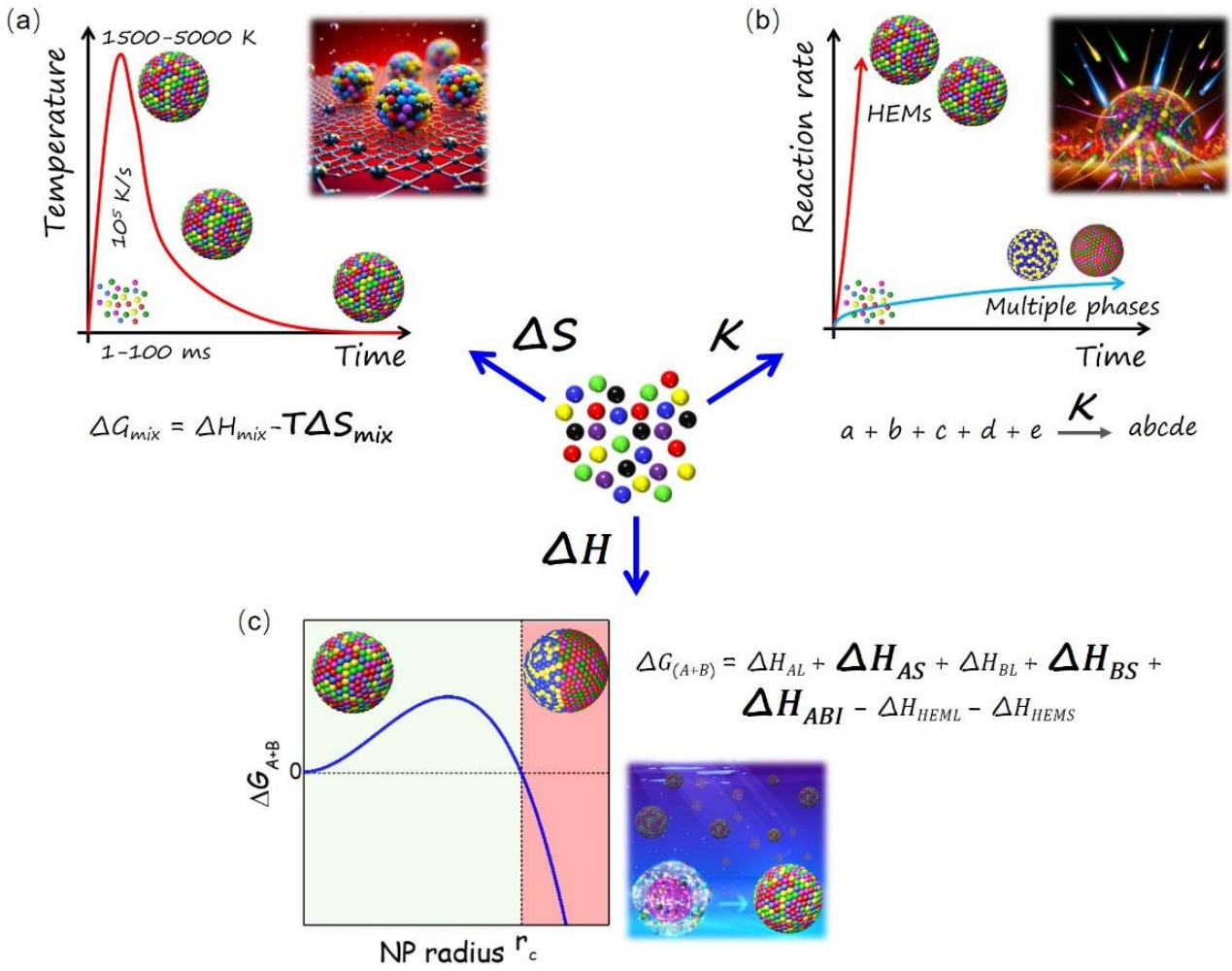

Figure 10. Scheme of the three main bottom-up strategies to directly produce HEM NPs from a mixture of atomic, ionic, or molecular precursors: (a) entropy-driven; (b) kinetics-driven; and (c) enthalpy-driven.

The first strategy employs the high-temperature conditions commonly used in bulk HEM synthesis while controlling particle size by limiting reactant availability and preventing nanoparticle Ostwald ripening and coalescence. This size limitation can be achieved in several ways: (i) shortening the reaction time to reduce diffusion distances; (ii) restricting precursor mobility by dispersing atomic/ionic/molecular precursors onto high-surface-area supports, within polymers, templates, or nanoreactors such as solvent droplets before initiating high-temperature crystallization; (iii) localizing the energy input to confine the reaction volume; and (iv) combining high-energy HEM formation with milling processes to disrupt large crystal growth.

The second strategy relies on kinetically driving HEM NP production, where atoms are prevented from arranging into their thermodynamically preferred configurations due to insufficient time or energy. This approach avoids the need for a significant entropic contribution, i.e. high temperatures. It requires a homogeneous dispersion of reactants, achievable using a suitable medium

such as a solvent where precursors are dissolved, a gas where gaseous or ionic reactants are combined, or a solid with simultaneous milling to overcome mass transport limitations. Three main approaches can be used for this strategy: (i) preassembling different components at low temperatures, followed by annealing at moderate temperatures that are sufficient for precursor reaction and HEM formation while remaining low enough to prevent phase segregation; (ii) simultaneous assembly and reaction of precursors via rapid, concurrent reduction or reaction of a homogeneous distribution of primary elements, achieved by rapid heating, the addition of a strong chemical reductant/reactant or injecting charge at a proper potential; and iii) using highly diluted solutions to minimize collisions and interactions between species that have the highest affinity for one another, thereby reducing phase segregation and promoting uniform element distribution.

A third strategy involves the enthalpy-driven formation of HEM NPs, which capitalizes on the significant contribution of surface and interface energies to the total energy of a NP. As particle size decreases, the influence of these energies becomes increasingly dominant, leading to a critical radius below which the formation of a single-phase HEM NP becomes more favorable than the formation of multiple phases, which would involve larger cumulative surface and interface energies. In such cases, the reduction of interfacial energy can drive the merging of phases into a homogenous HEM structure, stabilizing the NP. While pinpointing the precise mechanism behind HEM phase formation is highly challenging, and reports of enthalpy-driven synthesis schemes for HEM NPs are very rare, there are clear examples where enthalpy seems to play a dominant role. These include processes involving the sequential addition of elements into pre-formed nuclei, the transformation of heterostructured or binary NPs into HEM phases through phase merging, or the integration of additional elements via ion exchange or galvanic replacement, typically at or near ambient temperatures. These cases highlight the role of enthalpy in driving HEM NP formation, even under conditions where high-temperature entropic stabilization is not feasible.

Most examples provided here are categorized according to the rationale behind the design of the synthesis process. However, it is important to recognize the complexity in distinguishing between kinetically-driven and thermodynamically-driven HEM formation, thus several examples presented across sections could overlap or be mislocated. For instance, the high temperatures and ultrafast reactions typically associated with entropy-driven HEM NP synthesis (Section 3.1) could, in practice, be kinetically driven (Section 3.2), with the resulting HEM NP stability being mainly dictated by surface and interphase enthalpies (Section 3.3).

3.1. Entropy-driven HEM formation limiting NP growth

The first bottom-up strategy designed for producing HEM NPs mirrors the methods initially

developed for bulk HEMs, where entropy is considered the primary driver for HEM phase formation. In this approach, high temperatures are employed to maximize the mixing entropy in the Gibbs free energy equation ($\Delta G_{mix} = \Delta H_{mix} - T\Delta S_{mix}$).[54] However, to prevent excessive particle growth, strategies must be implemented to restrict reactant supply and minimize particle interactions. These strategies include ultrafast processing to limit growth time, highly dispersing or confining reactants to control the available material for NP growth, localizing energy input, and combining HEM formation with particle fragmentation to maintain nanoscale dimensions (**Figure 11**).

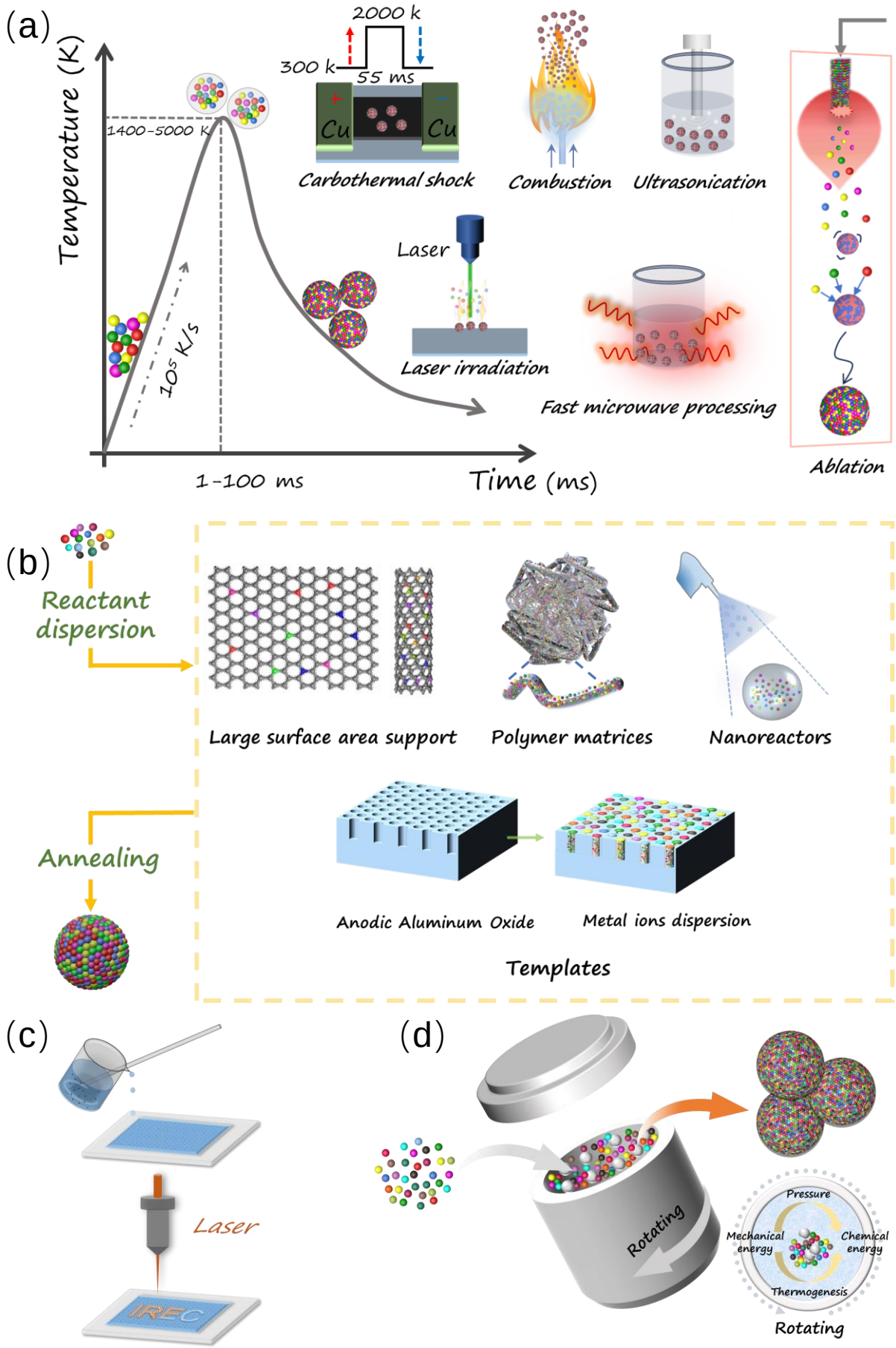

Figure 11. Scheme of the high-temperature processing strategies used to produce HEM NPs limiting

NP growth (a) using ultrafast thermal processing, (b) dispersing the reactants, (c) localizing energy input, and (d) mechanochemical method.

3.1.1. Short reaction times: Ultrafast thermal processing

To produce HEM NPs with a uniform distribution of five or more elements, a commonly used approach, adapted from methods for bulk HEM synthesis, involves applying very high reaction temperatures followed by rapid cooling. This method leverages the entropic term in the Gibbs free energy to stabilize a random distribution of elements, as initially proposed by Yeh et al.[55] To limit atomic diffusion and prevent excessive particle growth, the thermal annealing duration must be extremely brief, and cooling must be ultrafast to lock in the single-phase, random atomic distribution achieved at high temperatures. These elevated temperatures are not only crucial for maximizing entropy contributions but also play a vital role in overcoming the eventual insolubility of different elements, thereby promoting the formation of a uniform solid solution. Moreover, high temperatures reduce the critical radius for stability and promote rapid nucleation, enabling the formation of smaller particles if growth is effectively blocked. Several strategies have been developed to achieve ultrafast thermal processing. These include rapid Joule heating of supported precursors, laser pulses, ultrasound or microwave irradiation, discharge applications, and fueled self-propagating reactions. For these processes to succeed, high thermal conductivity is critical to ensure rapid heat transfer during both heating and cooling stages, particularly for the quick quenching of the high-temperature phase. Additionally, large surface areas for efficient heat exchange are essential, aligning well with the nanostructured nature of the materials produced.

3.1.1.1. Carbothermal shock

The carbothermal shock (CTS) method relies on the ultrafast heating and cooling of a material via Joule heating, typically achieved by passing current through a conductive carbon substrate. This method can achieve rapid heating and cooling rates of up to 10^5 K/s, helping to lock in the high temperature/entropy atomic distribution. By adjusting the shock duration, the size and distribution of the NPs can be controlled. CTS has been successfully applied to synthesize a wide range of HEM NPs, typically supported on carbon, as this approach relies on substrates that are both electrically and thermally conductive to effectively transfer the heat.[56] Carbon supports offer several additional advantages, including facilitating the reduction of metal precursors during HEA formation. While controlled-atmosphere systems have been developed to introduce various gas precursors, enabling the synthesis of non-metallic HEMs like oxides, phosphides, and chalcogenides, adapting this strategy for such materials remains challenging. It requires precisely controlled conditions and carefully selected precursors to ensure compatibility with the carbon support.[3d, 5a] The main drawback of the CTS method lies in its scalability. Scaling up to produce large volumes of material

is not straightforward, posing a challenge for industrial applications. Additionally, the use of gas-releasing precursors can introduce mass transfer limitations, further complicating the process. Despite these obstacles, the CTS method remains a highly effective approach for rapidly synthesizing HEM NPs with tunable properties, making it an excellent tool for laboratory-scale investigations of their unique characteristics.

As an example, Yao et al. developed a CTS method to produce HEAs containing two to eight metal elements (**Figure 12**).[57] In this process, different metal salts were mixed and loaded onto a conductive carbon support. The mixture then underwent a rapid thermal shock in a glovebox at 2,000 K for 55 ms, with heating and cooling ramp rates of 10^5 K/s. Similarly, Xie et al. synthesized CoMoFeNiCu HEA NPs with different Co/Mo ratios using the CTS method. Metal precursors loaded on carbon nanofibers (CNFs) were heated up to 2000-3000 K at ramp rates of 10^5 K/s for 55 ms.[56] The resulting CoMoFeNiCu HEA NPs exhibited a size of 22 nm, with an FCC crystal structure and noticeable lattice distortions. Additionally, Cui et al. produced (CrMnFeCoNi)S_x by this method using thiourea as the sulfur source. [5a] The CTS method also allows for tuning the architecture of the HEM NP. For instance, Zeng et al. developed a two-step CTS method to prepare core-shell NPs supported on carbon black.[58]

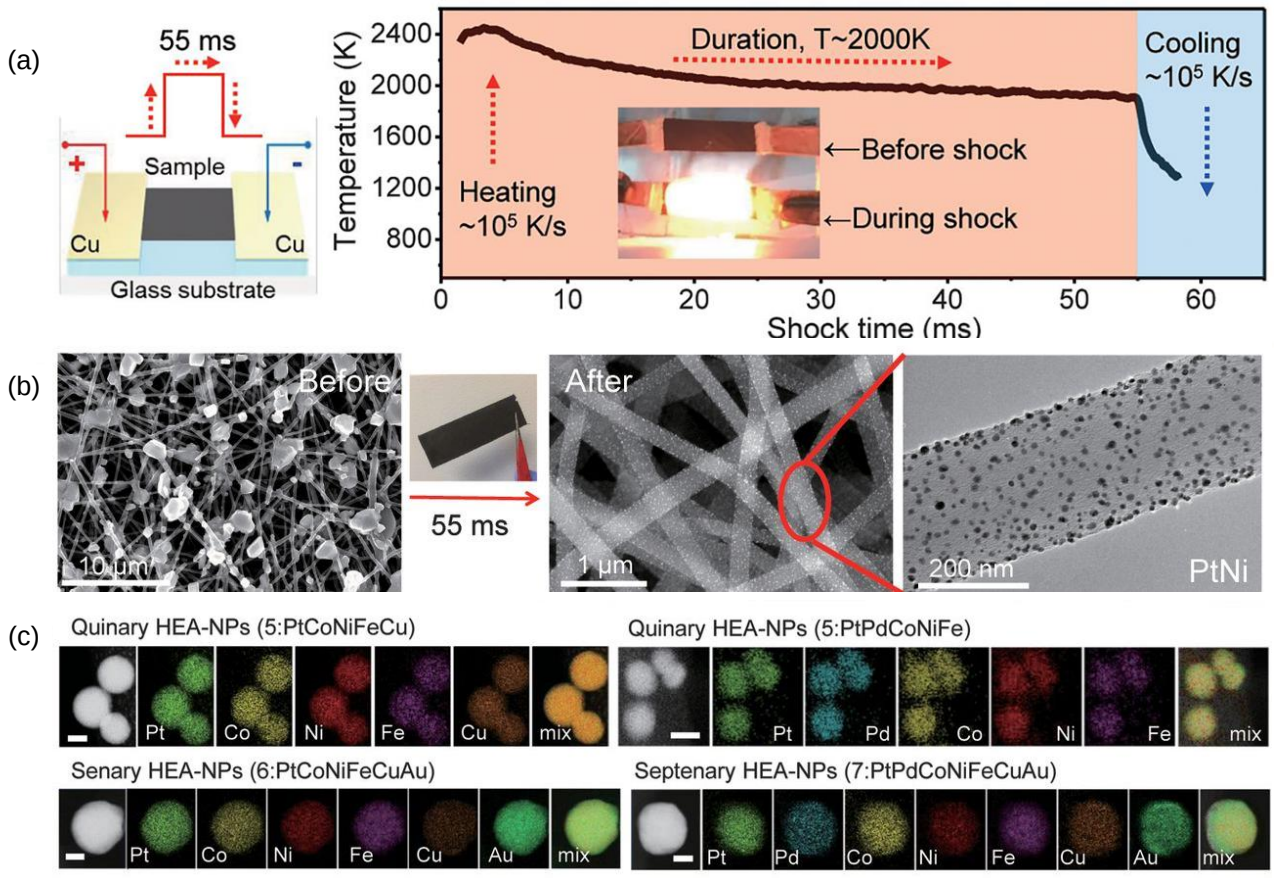

Figure 12. (a) Sample preparation and temperature evolution during the 55-ms thermal shock. (b)

SEM images of microsized precursor salt particles on the CNFs before thermal shock and the well-dispersed NPs obtained after CTS. (c) HAADF images and STEM elemental maps of HEA-NPs produced by CTS. Scale bar, 10 nm. Reproduced with permission [57] from CC- BY.4.0. open access publications.

3.1.1.2. Laser irradiation

Rapid laser pulses offer an alternative approach for generating thermal shocks by delivering concentrated bursts of energy within an extremely short time, leading to ultrafast heating rates. Additionally, the localized pulsed excitation facilitates rapid cooling, helping to preserve the high-temperature/entropy atomic configuration. However, similar to other thermal shock techniques, scaling up this method poses significant challenges. Besides, the localized nature of the laser pulse can lead to uneven laser absorption both laterally and in depth, resulting in temperature variations and, consequently, inhomogeneous products. Thus, achieving uniformity across larger scales remains a significant challenge.

As an example, Li et al. combined the dispersion of the precursor in CNFs as large-area support with ultrarapid thermal processing using laser pulses to produce AuPdFeCuNi HEM NPs.[6a] As shown in **Figure 13**, in this process, metal precursor salts were first dissolved in ethanol and uniformly coated onto the CNF surface. The salt-coated CNF was then irradiated with a laser, where the incident laser energy was predominantly absorbed by the metal salts, leading to photothermal-induced melting. The melted products underwent carbothermal reduction, forming globular liquid metal droplets that minimized their surface energy on the nonwetting CNF surface, accompanied by the release of gaseous byproducts. These droplets subsequently crystallized, resulting in the formation of HEM NPs. The study demonstrated that both composition and phase structure could be modulated by adjusting the laser irradiation time. For instance, with an irradiation time of 0.25 ms, the AuPdFeCuNi HEA NPs formed were approximately 14 nm in size with an FCC crystal structure. However, extending the irradiation time to 2.5 ms resulted in the growth of AuPdFeCuNi NPs into faceted truncated shapes with diameters ranging from 30 to 60 nm, exhibiting both FCC and BCC phases.

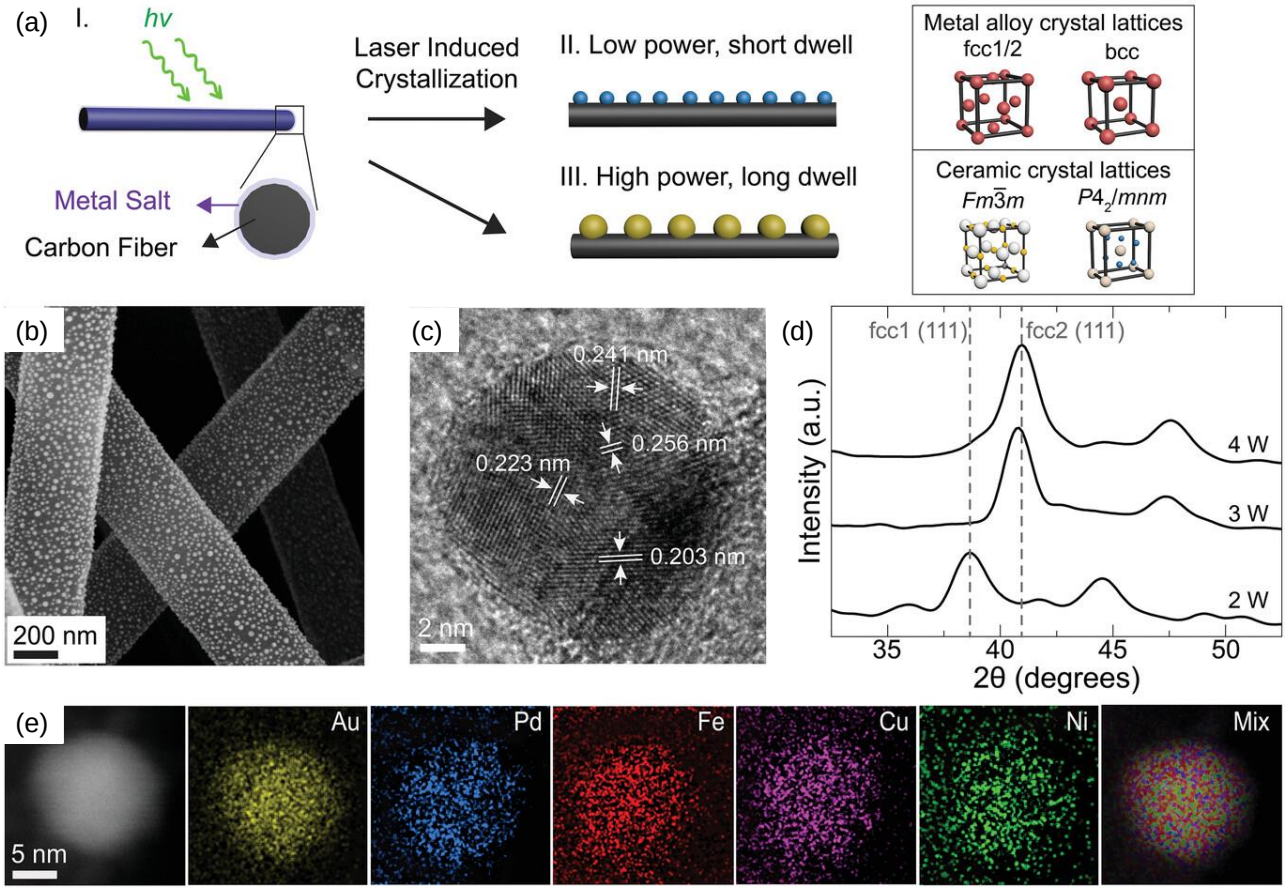

Figure 13. (a) Schematic of the laser-induced synthesis of HEA NPs on CNF scaffolds. (b) SEM, (c) HRTEM, and (d) wide-angle X-ray scattering (WAXS) and (e) HAADF-STEM and EDS elemental mapping micrographs of AuPdFeCuNi HEAs. Reproduced with permission.[6a] Copyright 2023, Wiley-VCH GmbH.

3.1.1.3. Fast microwave processing

Microwave heating is another effective method for delivering large amounts of thermal energy within short timeframes, typically seconds. By inducing high-frequency oscillation of dipole molecules within the material, microwave heating generates internal friction that rapidly and uniformly produces heat throughout the sample. During this fast heating process, metal salts can decompose into liquid metals, which then solidify into HEM NPs through rapid quenching. For efficient microwave heating, the material or its support must have appropriate dielectric properties, sufficient charge carrier density, magnetic properties, and/or defects to effectively absorb microwave energy. Similar to other irradiation-based strategies, the material's properties influence the maximum thickness that can be effectively treated, as energy absorption decreases with depth. Additionally, heat dissipation becomes more challenging when dealing with large volumes, as maintaining uniform temperature distribution can be difficult. However, a unique advantage of microwave heating is its ability to deliver localized energy transfer within relatively large volumes, especially in non-absorbing solvents. This characteristic makes microwave heating a promising thermal shock method

for scaling up production. However, thermal dissipation within a non-absorbing media may be a limitation in reaching high temperatures. For this reason, microwave processing is typically employed using solid supports.

As an example, Qiao et al synthesized PtPdFeCoNi HEA NPs using the microwave heating method achieving uniform NPs with an average size of ~12 ± 5 nm (**Figure 14 a-d**).[59] In this process, a piece of reduced graphene oxide (rGO) with enough defects can effectively adsorb the microwave to achieve 1850 K in 160 ms, thus enabling the rapid decomposition of precursors into liquid metal (**Figure 14e**). The system was then rapidly cooled at a rate of 6×10^4 K/s upon turning off the microwave, ensuring the formation of single-phase HEA NPs.

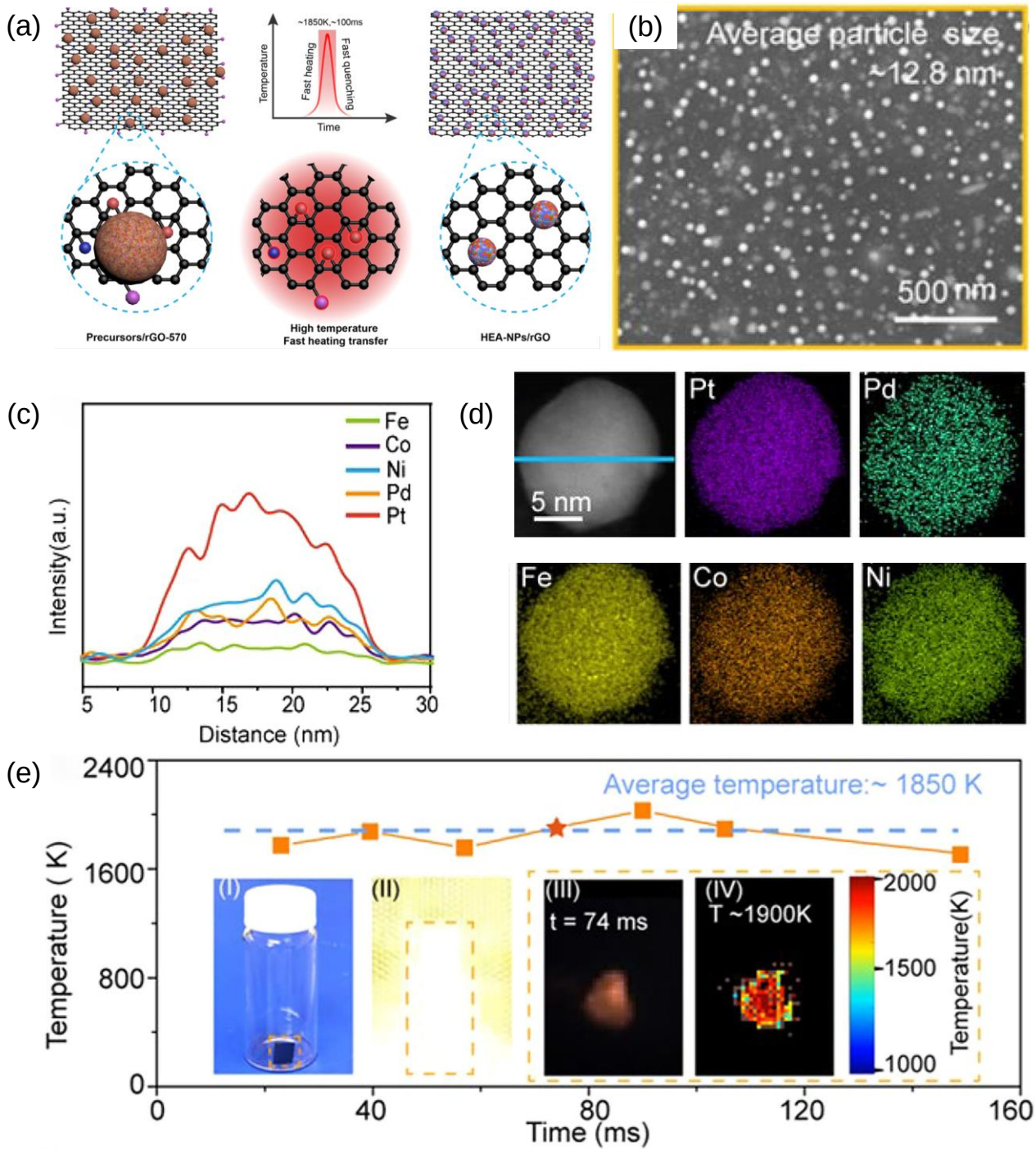

Figure 14. (a) Schematic illustration of the formation of HEA NPs on rGO by microwave heating. (b) SEM image of the HEA NPs on the rGO film. (c) EDS line scan along the blue line across the PtPdFeCoNi HEA NP, (d) HAADF-STEM image and STEM-EDS elemental mapping of a PtPdFeCoNi HEA NP. (e) Temperature profile of the film during microwave heating. Reproduced with permission.[59] Copyright 2021, American Chemical Society.

3.1.1.4. Combustion synthesis

Combustion synthesis operates at the interface of liquid and gas-phase methods, utilizing the high energy released by a rapid, self-sustaining exothermic reaction to achieve temperatures in the range of 1000-2000 K, with heating rates up to 70 K/s.[60] In this approach, a fuel, often glycine, and

an oxidizer, such as nitrates, are introduced into the precursor solution, generating combustion waves that propagate quickly through the reaction front triggering the reaction. As the fuel is consumed, the resulting porous structure rapidly cools, preserving nanoscale features.[61] Combustion synthesis offers the advantage of using water as media for precursor dissolution, lowering costs and reducing environmental impact and toxicity. Glycine not only fuels the reaction but also complexes with metal cations, enhancing solubility and preventing selective precipitation upon water evaporation. The even distribution of the fuel within the precursor mixture ensures uniform heating, enabling high production yields and throughput, though residual carbon is often a challenge. A specific variant, flame spray pyrolysis, combusts a fine spray of the precursor solution, achieving even faster cooling rates for better control over particle formation. [62]

Numerous examples of the synthesis of HEM nanomaterials have been reported (**Figure 15**).[63] For instance, Zhu et al. produced single-phase rock salt (MgCoNiCuZn)O HEO NPs by the combustion synthesis method using nitrate salts as the precursor in a glycine aqueous solution.[64] Upon evaporating all the water to obtain a slurry, a vigorous combustion reaction occurred, reaching temperatures up to 1500 K. Similarly, Lin et al. applied this method to synthesize $(FeMnCoNiZn)_3O_4$ using glycine as both complexing agent and fuel.[65] The nitrate salts and glycine mixture was stirred and dried at 70 °C to form a gelatinous state, which was then placed in a 200 °C oven to self-combust into a fluffy, porous precursor, followed by calcination at 900 °C for 30 min to yield a $(FeMnCoNiZn)_3O_4$ nanopowder.

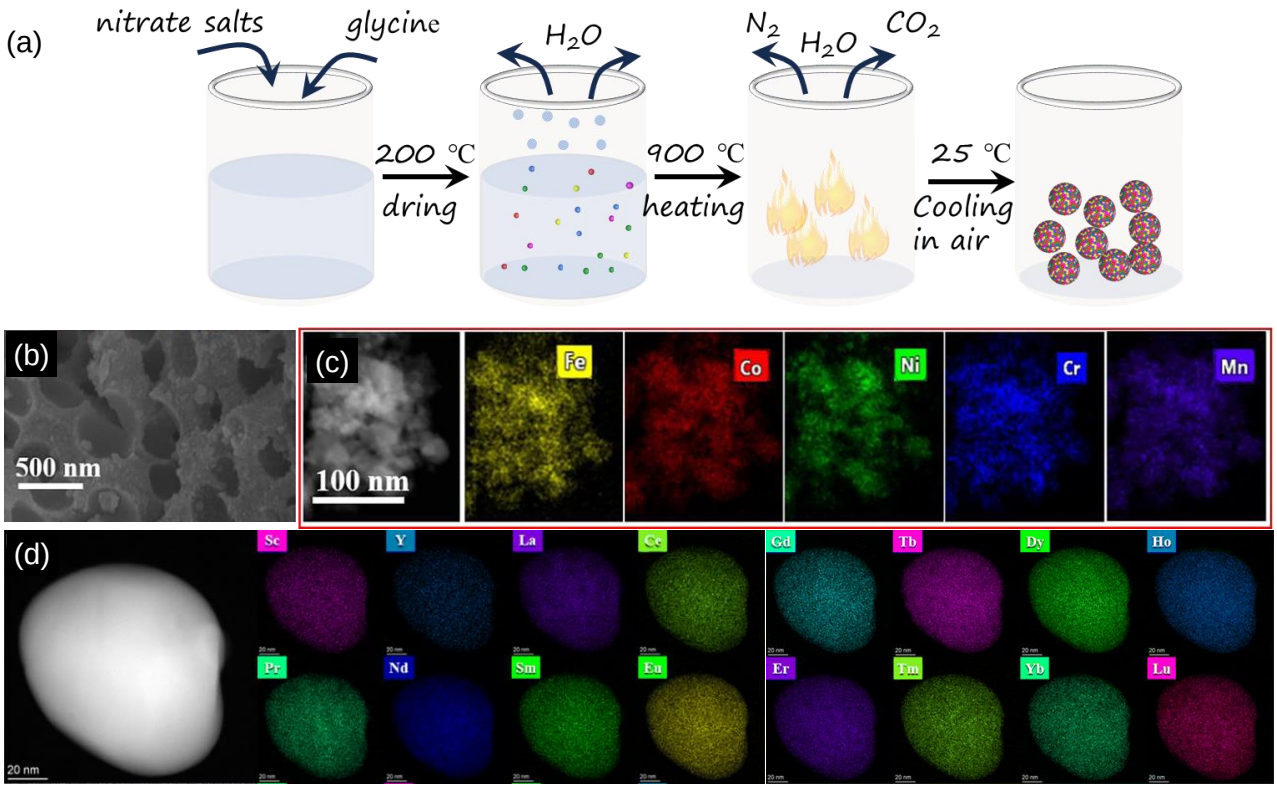

Figure 15. (a) Scheme of the combustion synthesis of a nanostructured HEM. (b) SEM image, and (c) STEM-EDS mapping of the nananostructured HEO. (b) and (c) are reproduced with permission.[63a] Copyright 2023, Elsevier B.V. (d) HAADF STEM and EDS elemental mapping of the produced material. Reproduced with permission.[63b] Copyright 2023, the Royal Society of Chemistry.

3.1.1.5. Ultrasonication

In an ultrasound process, acoustic cavitation generates extremely high temperatures in small, localized regions for brief durations. This phenomenon involves the formation, gradual enlargement, and rapid implosive collapse of microscopic bubbles. Upon collapse, these bubbles produce pressures around 2,000 atmospheres and temperatures approaching 5,000 K in tiny, localized zones, all occurring in less than a nanosecond.[66] This instantaneous release of massive energy can trigger precursor decomposition and reaction with minimal mass transport, enabling NP nucleation while minimizing their growth.[67]

As an example, Liu et al. used the ultrasonication-assisted wet chemistry method to produce 3 nm PtAuPdRhRu HEA NPs.[68] Under intense ultrasonication irradiation, Pt^{4+}, Au^{3+}, Pd^{2+}, Rh^{3+}, and Ru^{3+} ions were co-reduced in ethylene glycol (EG), which acted as both the reductant and solvent. A subsequent moderate-temperature annealing step completed particle crystallization while avoiding phase segregation. To simplify the process, Okejiri et al. developed a one-step method where the metal ions were co-reduced in an alcohol-based ionic liquid without additional heat treatment.[69] The ionic liquid functioned as both a reductant and a protective agent, effectively limiting particle growth (**Figure 16**).[70]

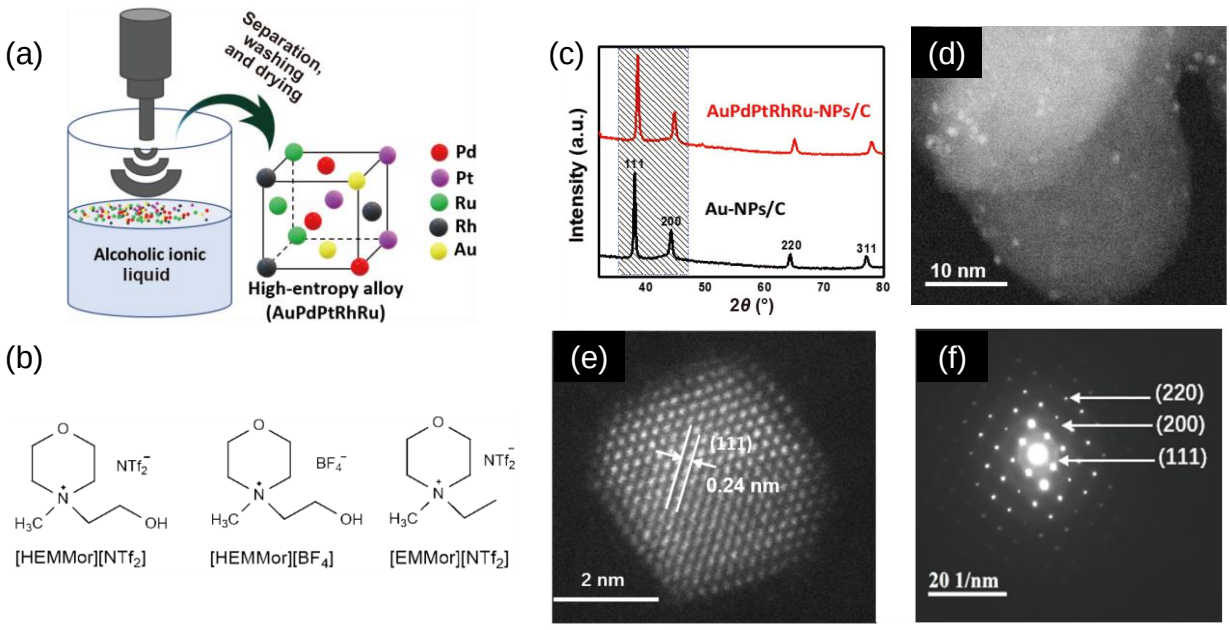

Figure 16. (a) Schematic illustration of the synthesis of HEA NPs via ultrasonication promoted by an alcoholic ionic liquid. (b) Structure of the ionic liquids. (c) XRD patterns of the AuPdPtRhRu-

NPs/C and the gold standard (Au-NPs/C). (d) STEM image of HEA-NPs/C at a higher resolution. (e) HR-STEM image of HEA-NPs/C showing a lattice fringe spacing of 0.24 nm consistent with (111) plane of an FCC structure. (f) SAED pattern of HEA-NPs/C displaying a Debye-Scherrer ring pattern consistent with a polycrystalline FCC lattice. Reproduced with permission.[69] Copyright 2021, Tsinghua University Press and Springer-Verlag GmbH Germany, part of Springer Nature.

3.1.1.6. Ablation

Ablation reactions can be used to produce HEM NPs not only from homogeneous HEM precursors as discussed in Section 2, but also from multiphase or multiple targets. In the bottom-up approach, ablated elements combine within the generated plasma or spark to form HEM NPs. Ablation processes rapidly generate a high-energy plasma that reaches ultrahigh temperatures and undergoes rapid cooling when it contacts a liquid medium or solid support, which allows for the formation of entropy-stabilized HEM phases while minimizing NP growth.

As an example, Mao et al. synthesized HEA NPs with five and six elements using the arc discharge method.[71] Metal powders of Al, Co, Cr, Cu, Fe, and Ni with varying Al ratios were compressed on a graphite crucible (anode), while a graphite needle served as the cathode. An arc was generated at 100 A, 10^{-3} Pa vacuum, in an ArH atmosphere for 15 min to evaporate the powders, which then recondensed on the chamber's inner surface. The resulting NPs were spherical with a uniform size of 110-180 nm (**Figure 17 a-c**). They also produced HEAs with up to 21 elements by using extremely high evaporation temperatures and ultrafast cooling.[72] Similarly, Feng et al. synthesized 55 types of NPs, from binary to HEAs, by quenching a microsecond-long oscillatory spark metal vapor.[73] Alternating electrode vaporization and controlled oscillatory sparks allowed precise tuning of metal feed composition (**Figure 17 d-e**). Rapid quenching (10^7-10^9 K/s) retained single-phase compositions, enabling customizable alloy mixing by adjusting spark parameters and electrode materials.

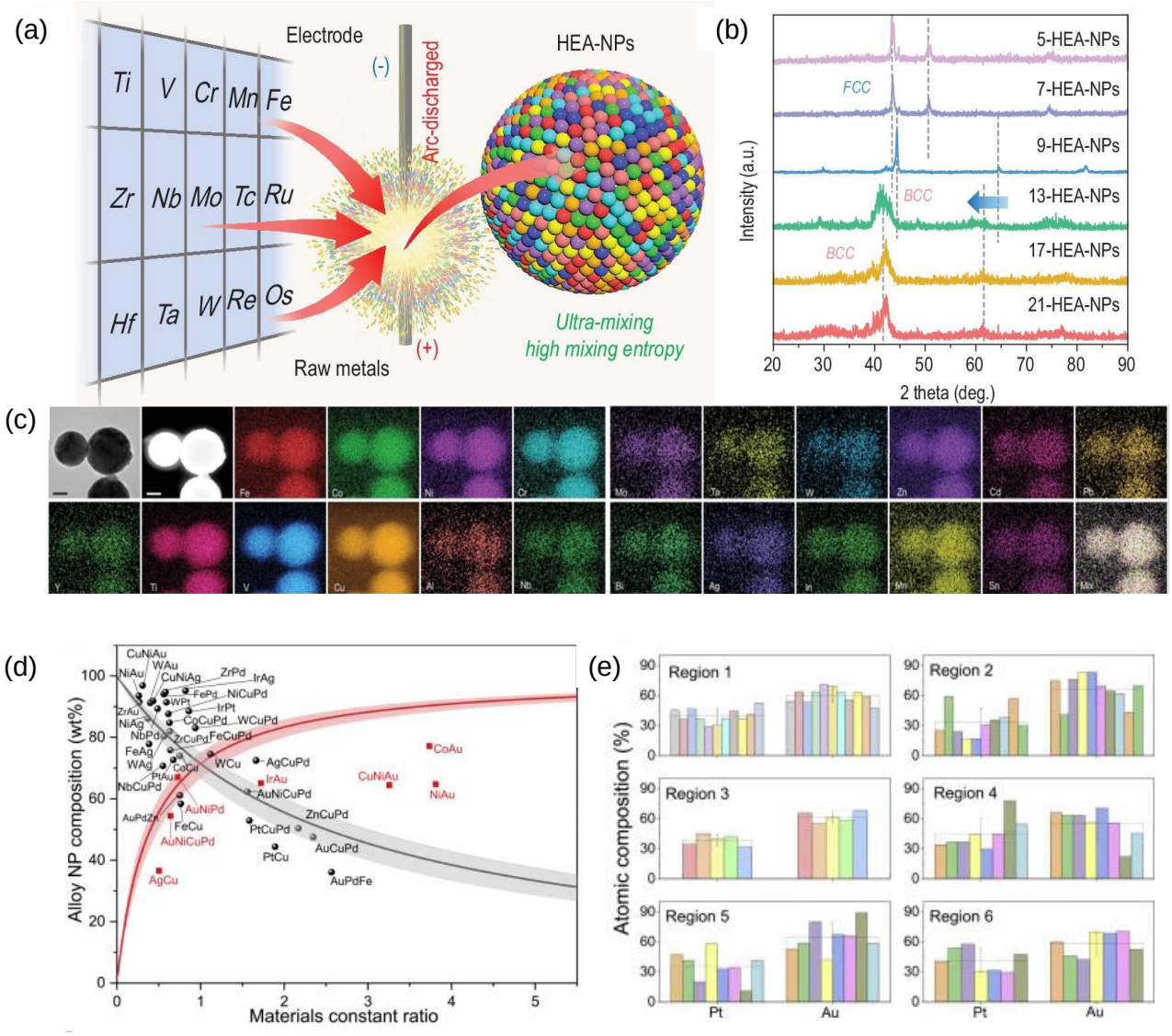

Figure 17. (a) Schematic of the arc-discharged approach for synthesizing different HEA-NPs. (b) XRD patterns of the HEA-NPs with different composited elements. (c) TEM-EDS maps of 21-HEA-NPs (FeCoNiCrYTiVCuAlNbMoTaWZnCdPbBiAgInMnSn), scale bars: 50 nm. Reproduced with permission [72] from CC- BY.4.0. open access publications. (d) Composition of various alloy NPs (wt %) from the measurements (scatters) and model predictions (curves). (e) EDS compositional (atom %) uniformity. Each bar represents the elemental composition of an NP in the given region, and error bars indicate the standard deviation of the number of measured NPs. Reproduced with permission.[73] Copyright 2020, Elsevier Inc.

3.1.2. Reactant dispersion

A second strategy commonly used to limit NP growth at the high temperatures needed for maximizing entropy in HEM formation is to restrict the reactant supply by diluting or dispersing the precursor. In this approach, the formation of large particles is similarly constrained by mass transport, as discussed in the previous section. However, the limitation here arises not from restricted diffusion time but from the increased diffusion distances that prevent the accumulation of reactants, thereby limiting particle growth. In this approach, the concentration of ionic, atomic, or molecular precursors

within the reacting volume must be reduced to prevent not only growth from atomic incorporation but also Ostwald ripening and particle aggregation. This can be achieved by dispersing the precursors on the surface of porous materials, within a solid matrix (e.g., a polymer), or in a confined liquid environment (e.g., aerosol droplets). In surface supports and solid matrices, mass transport is restricted by interactions between the relevant species and the host material. However, in a liquid environment, the high diffusivities of the precursors may necessitate confining the liquid volume by forming small droplets or using templates to prevent uncontrolled growth. It is worth noting that these two strategies, minimizing reaction time and dispersing reactants, are often used together, as seen in many examples discussed earlier. Here, we focus on different dispersion techniques, providing additional examples. While ultrafast thermal processing is not strictly necessary with well-dispersed precursors, high temperatures remain essential for forming the entropy-driven HEM phase, and rapid cooling is crucial to preserve it.

3.1.2.1. Large surface area support

The most commonly used approach to limit NP growth by restricting reactant supply at the high temperatures typically required for entropy-driven HEM formation is dispersing the precursor on a support with a large surface area. Common supports include high surface area and porous carbons such as graphene, graphene oxide (GO), carbon nanotubes (CNTs), N-rich mesoporous carbon sheets, as well as zeolites, metal-organic frameworks (MOFs), and polymers.[74] To further limit reactant diffusivity, the precursor can be anchored or even integrated into the support, such as metal ions within MOFs. Additionally, support selection depends on the intended application. Since NP growth is constrained by the available reactant, ultrafast thermal processing is not required, which enhances scalability. However, the temperature, heating rate, and duration of the post-annealing process remain critical factors in controlling the final NP size and composition.

As an example, Feng et al. proposed a simple anchoring and alloying method to produce CoNiCuMgZn HEA NPs using 2D GO as both a template and reductant for the growth of mixed metal precursors.[75] As shown in **Figure 18**, metal acetate salts were mixed with GO and dissolved in an EG solution, and then the solution was stirred continuously at 170 °C with a reflux condenser for 3 h. In this process, the mixed metal precursors connected with the oxygen-containing groups of GO by electrostatic interaction, and the precursors were uniformly spread on both sides of GO sheets. Then the as-prepared metal precursors/GO composites were annealed at 900 °C under N_2 atmosphere. Benefiting from the pinning effect between the graphene sheet and metal ions, the HEA NPs uniformly anchored on graphene without excessive aggregation. The size of CoNiCuMgZn HEA NPs could be tuned from 40-200 nm by adjusting the added amount of the metal acetates.

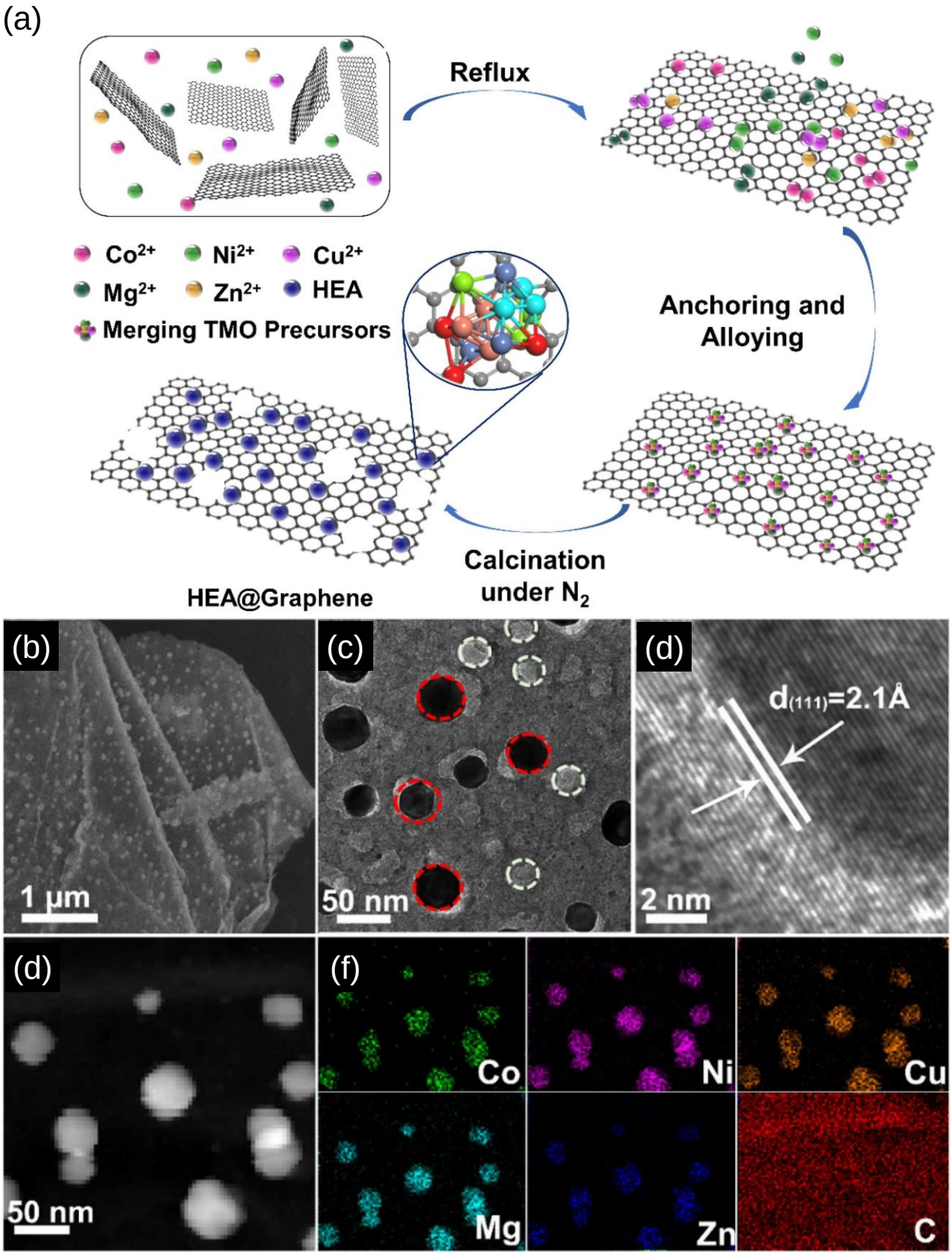

Figure 18. (a) Schematic representation of the formation mechanism of 2D holey HEA@Graphene composites through the anchoring and alloying approach. (b) SEM image, (c) TEM image (red circle: HEA grains, white circle: holes on graphene), (d) HRTEM image, (e) the HAADF-TEM image and (f) corresponding element mappings of CoNiCuMgZn HEA NPs. Reproduced with permission.[75]

3.1.2.2. Polymer matrices

To constrain NP growth by limiting the amount of reacting precursor available at each nucleation site during high-temperature synthesis of HEM NPs, reactants can be also dispersed within the volume of a solid matrix, typically a polymer. Additionally, the polymer can be nanostructured to enhance specific performance characteristics while simultaneously improving precursor dispersion. Techniques such as electrospinning and electrohydrodynamic jet printing enable the production of ultrafine fibers and fiber-based patterns by using an electric field to draw and stretch a polymer solution or melt.[59, 76] These methods can be used to synthesize HEM NPs and even nanofibers by incorporating diverse metal cations into the nanofibers during electrospinning, followed by a post-calcination step at the appropriate temperature for HEM formation.[77]

As an example, Li et al. synthesized TiHfNbTaMoN nanofibers via electrospinning followed by calcination under NH_3 atmosphere at 600-1000 ºC for 2h (**Figure 19**), resulting in an FCC structure with uniformly dispersed metal elements.[78] Wei et al. demonstrated that the annealing temperature could influence the crystal phase of HEM nanostructures produced by electrospinning: temperatures between 900-1100 ºC yielded defective fluorite-structured $((La_{0.25}Nd_{0.25}Sm_{0.25}Gd_{0.25})_{0.75}Yb_{0.25})_2Zr_2O_7$, while temperatures above 1100 ºC led to the formation of a pyrochlore structure.[79] Additionally, the size of the NPs anchored on the nanofibers could be controlled by adjusting the annealing temperature.[80]

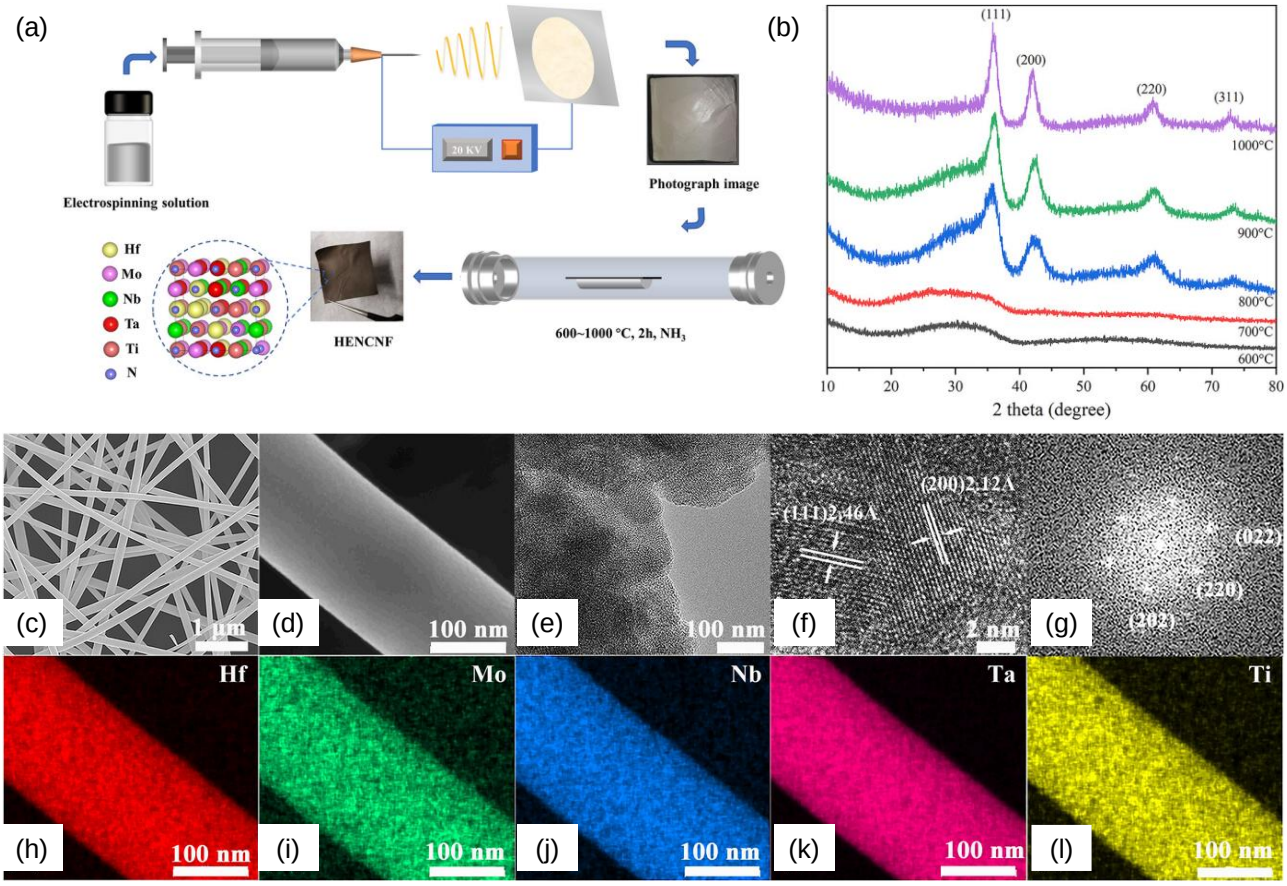

Figure 19. (a) Schematic diagram of the synthesis of high entropy nitride ceramic fibers. (b) XRD, (c-d) TEM images, (e-f) HRTEM image, (g) FFT pattern, and (h-l) EDS elemental mappings of TiHfNbTaMoN nanofibers. Reproduced with permission.[78] Copyright 2020, John Wiley and Sons.

3.1.2.3. Templates or nanoreactors

The amount of reactant involved in the synthesis of a HEM NP can also be limited by confining its growth within small volumes using templates. Templates have been widely employed to control the growth of various nanostructured materials. Hard templates, in particular, are ideal for HEM synthesis as they can withstand the high temperatures typically required, making them effective candidates for producing HEM nanostructures by restricting reactant supply. However, the need for post-process template removal adds complexity to the synthesis of porous HEOs.–

Hou et al. used soluble NaCl as a hard template to synthesize perovskite-type $Zr_{0.5}(NiFeCuMnCo)_{0.5}O_x$. NaCl was added to metal chloride salts and the anions exchanged during balling and subsequent calcination at 500 °C. Finally, the NaCl template could be removed by washing with deionized water and ethanol, the remaining pores with a specific surface area of up to 84 $m^2 g^{-1}$.[81] Wei et al. also used NaCl as a hard template to disperse the metal chlorides, then the solution was dried and annealed to produce FeCoNiCrMn with an FCC structure.[82] Xu et al. used SiO_2 as a removable hard template to synthesize Pd_1(CeZrHfTila)O HEO, which was later etched away using a NaOH aqueous solution.[83] Zhao et al. synthesized high-entropy rare-earth monosilicate NPs with

particle sizes of 60 nm and 200 nm by using SiO_2 templates of different sizes.[84] Rare metal oxides, combined with urea and SiO_2, were dissolved and dispersed in HNO_3, and the solution was then evaporated to form a gel. This gel underwent annealing at 1473–1673 K to achieve the single HEM phase (**Figure 20**).

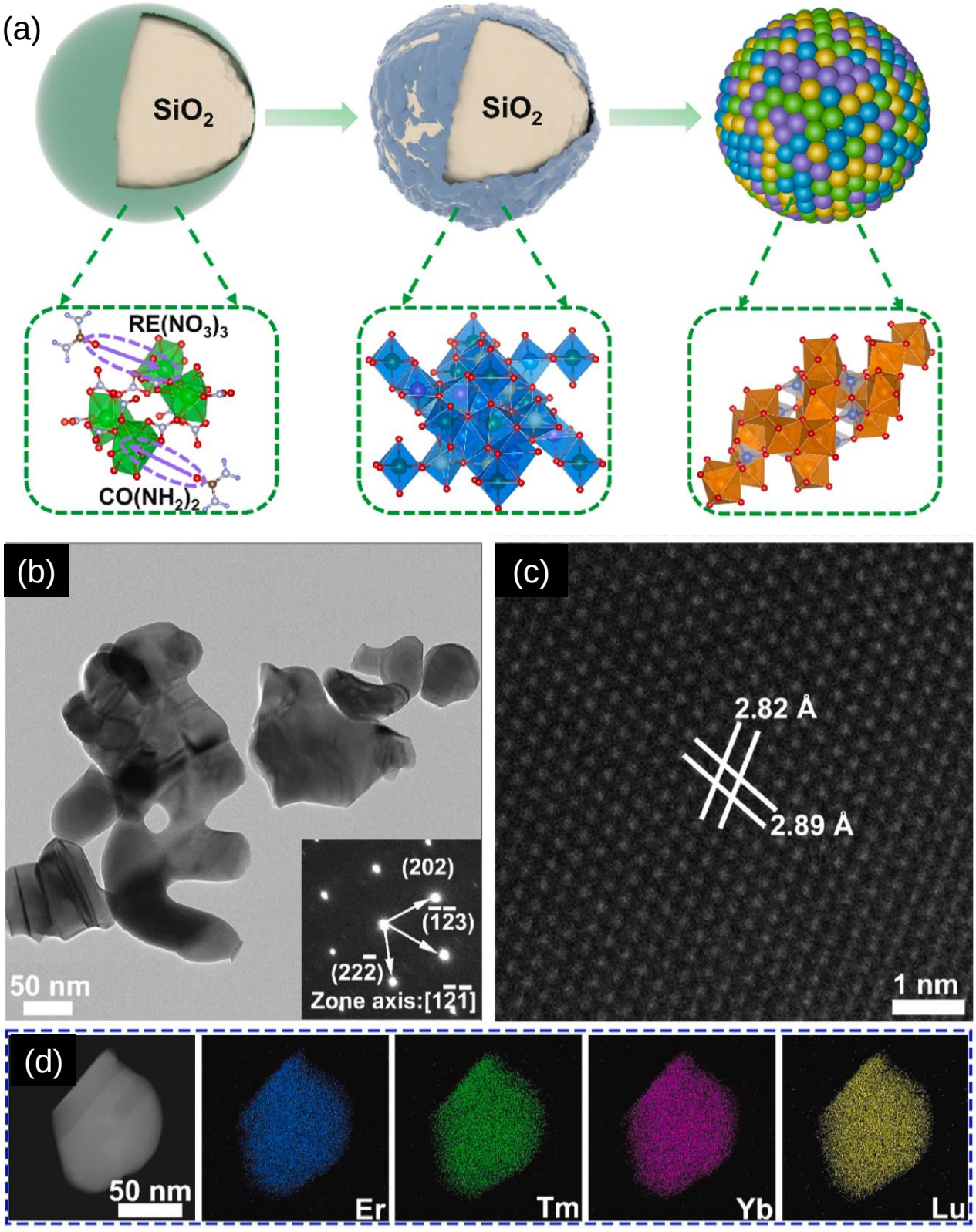

Figure 20. (a) Schematic diagram of the template synthesis process to produce high-entropy rare-earth monosilicate NPs. (b) TEM image and corresponding SAED pattern. (c) HRTEM image. (d) STEM image and corresponding EDS compositional mappings. Reproduced with permission.[84] Copyright 2024, Elsevier Ltd and Techna Group S.r.l.

3.1.2.4. Nanoreactors

A similar and frequently undistinguished strategy to limit reactant supply involves its phase separation within micro- or nanoreactors. While templates can function as nanoreactors, the template approach primarily involves physically confining particle growth by the template walls, which often also directs particle shape. The amount of precursor involved in the NP growth is constrained by the confined space but not necessarily by its initial location. In contrast, in nanoreactors, particle size is controlled not by the reactor's walls but by the fixed amount of precursor initially available within this reactor, without any external replenishment during the process. In nanoreactors, the size and shape of the NP can vary significantly from the dimensions of the nanoreactor itself because the particle size is determined by the amount of precursor available, rather than the physical boundaries of the reactor.

In nanoreactors, the reactant is contained in small portions of a gas, liquid, or solid media that are dispersed within an immiscible media in the same or different state. As an example, phase separation can be achieved by gas bubbles within a liquid as generated by sonochemical activation described above in the section on ultrafast processing, but also with aerosol droplets suspended in a gas phase or small polymer beads dispersed on a support for instance. These small volumes of material are then subjected to a high-temperature annealing to form the HEM NPs. While ultrarapid thermal processing is not strictly necessary to prevent NP growth, rapid heating and particularly cooling are frequently used as they are favored by the isolated small volumes of material in play. In aerosols, typically aqueous solutions containing different metal salts are nebulized into small droplets smaller than 1 μm, which act as a nanoreactor with very low thermal mass loss, and then subjected to a rapid heating and quenching process. In liquid aerosol droplets, atomic-level mixing of multiple immiscible elements can be easily attained. The dynamic drying of the small droplet enhances the interaction between different metal atoms, and avoids the thermal and mass transfer gradients, thus facilitating the formation of HEM NPs. The aerosol can be produced within a heated media to react the precursor as in the examples above, or can incorporate a fuel for self-combustion. This second direction, the flame spray pyrolisis, was discussed in the previous section.

As an example, Yang et al. developed a scalable method for synthesizing HEA NPs using an aerosol droplet-mediated approach with a rapid tube furnace heating and quenching process (**Figure 21 a-c**).[85] Metal precursors were mixed with water to form aerosol droplets, which were dried in

Ar/H_2 and subjected to thermal shock at 1100 °C for 3 s, followed by rapid quenching at 10^5 K/s. This process produced NiCoCuFePtPd HEA NPs with a uniform composition and an average diameter of ~60 nm. Similarly, Phakatkar et al. synthesized $(Mn, Fe, Ni, Cu, Zn)_3(O)_4$ HEO NPs via flame spray pyrolysis at 1900 °C with an average size of 17 nm, uniform elemental distribution and a spinel structure (**Figure 21 d-g**). [86] The precursor solutions were mixed with ethanol and metal chloride salts to generate aerosol droplets using a twin fluid nozzle. These droplets were then exposed to a propane torch flame with a propane flow rate of 4.2 L/min and an air/propane ratio of 24:1. The high flame temperature facilitated the formation of crystalline, homogeneous NPs.[87] The short residence time helped maintain nanoscale particle size.[88] The vaporized metal then instantaneously reacted with the oxygen available in the environment to form the respective gaseous metal oxides[89] and then led to the nucleation of solid metal oxide NPs.

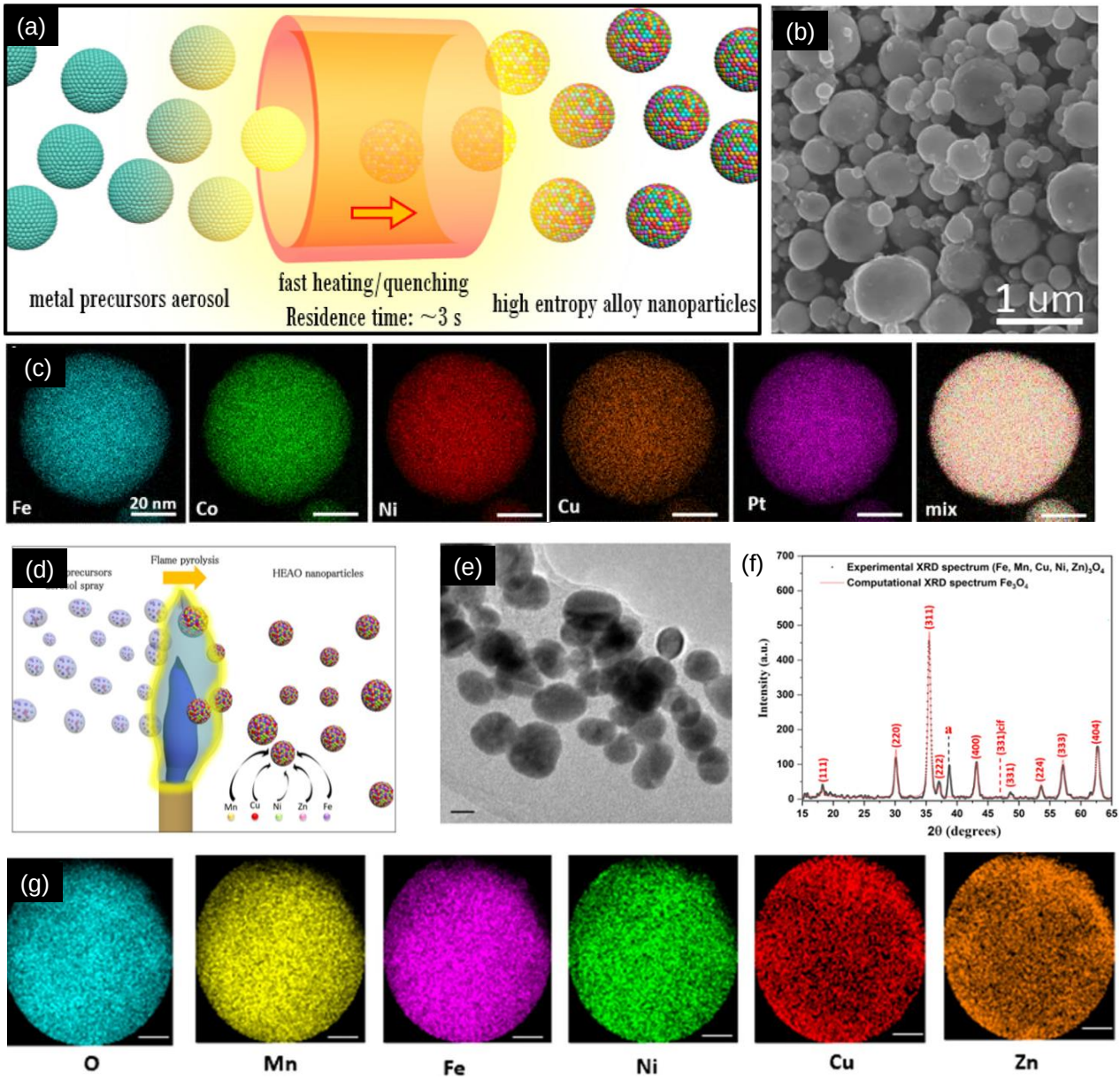

Figure 21. (a) Schematic of the evolution of aerosol droplets during the high-temperature treatment. (b) SEM image of HEA NPs. (c) EDS mappings for a single HEA NPs. Reproduced with permission.[85] Copyright 2020, American Chemical Society. (d) Schematic representation of HEO NPs synthesis process. (e) Low-magnification TEM micrograph (scale bar represents 10 nm). (f) XRD pattern analysis of HEO NPs along with the Rietveld refinement confirming the spinel phase. (g) STEM-EDS mapping of single HEO NPs (scale bar represents 10 nm). Reproduced with permission.[86] Copyright 2021, American Chemical Society.

Another example of phase separation within nanoreactors involves dispersing the precursor within small polymer bids. Scanning-probe block copolymer lithography (SPBCL) uses polymeric nanoreactors to synthesize structurally and chemically diverse NPs. The process involves two main steps: First, dip-pen nanolithography (DPN) or polymer pen lithography (PPL) is used to precisely deposit attoliter-scale volumes of ink to create arrays of block copolymers on hydrophobic substrates, forming nanoreactors. Second, these nanoreactors undergo thermal treatment. During annealing, metal precursors within the polymer matrix aggregate and reduce, while the polymer decomposes, resulting in the formation of individual NPs from each dome-like feature.[90]

3.1.3. Localized energy input

Another approach to limit the amount of reactant involved in NP growth at high temperatures is to reduce the reaction volume by strongly localizing the energy supply. This method eliminates the need for physical confinement of the reactant or NP growth within the walls of a template or nanoreactor, thereby potentially simplifying the process by eliminating the complexity associated with generating and eventually removing the template or reactor. Techniques such as laser irradiation or electron beam exposure can achieve this, as seen in direct electron-beam writing. This strategy typically produces supported particles or patterned structures on a substrate.

As an example, Hegde et al. produced $Ni_{0.24}Co_{0.23}Cu_{0.24}Fe_{0.15}Cr_{0.14}$ HEO NPs using a one-step femtosecond laser direct writing (FsLDW) process (**Figure 22).**[91] A solution-based precursor ink was deposited on a substrate, dried, and then illuminated by a femtosecond laser, transforming the dried ink into HEO/alloy NPs while bonding them to the substrate. This method is versatile, applicable to a wide range of oxides and alloys, and enables binder-free electrode fabrication in ambient conditions without the need for controlled environments or high-temperature treatments. The localized laser energy precisely transforms and bonds materials without substrate damage. Similarly, Yang et al. produced CoCrFeNiAl high entropy ceramics (HECs) by pulsed laser scanning on mixed salt solutions deposited on substrates like indium tin oxide (ITO), Ni foam, and carbon cloth.[92] The laser, operating at 2W with 200 kHz repetition and 100 ns pulse duration and heating and cooling rates of 10^7 and 2.5×10^6 K/s, provided sufficient energy to break metal nitrate bonds, allowing metal ions to rapidly combine with oxygen to form HECs. Increasing the number of laser scans led to larger

HEC NPs due to enhanced solid diffusion.

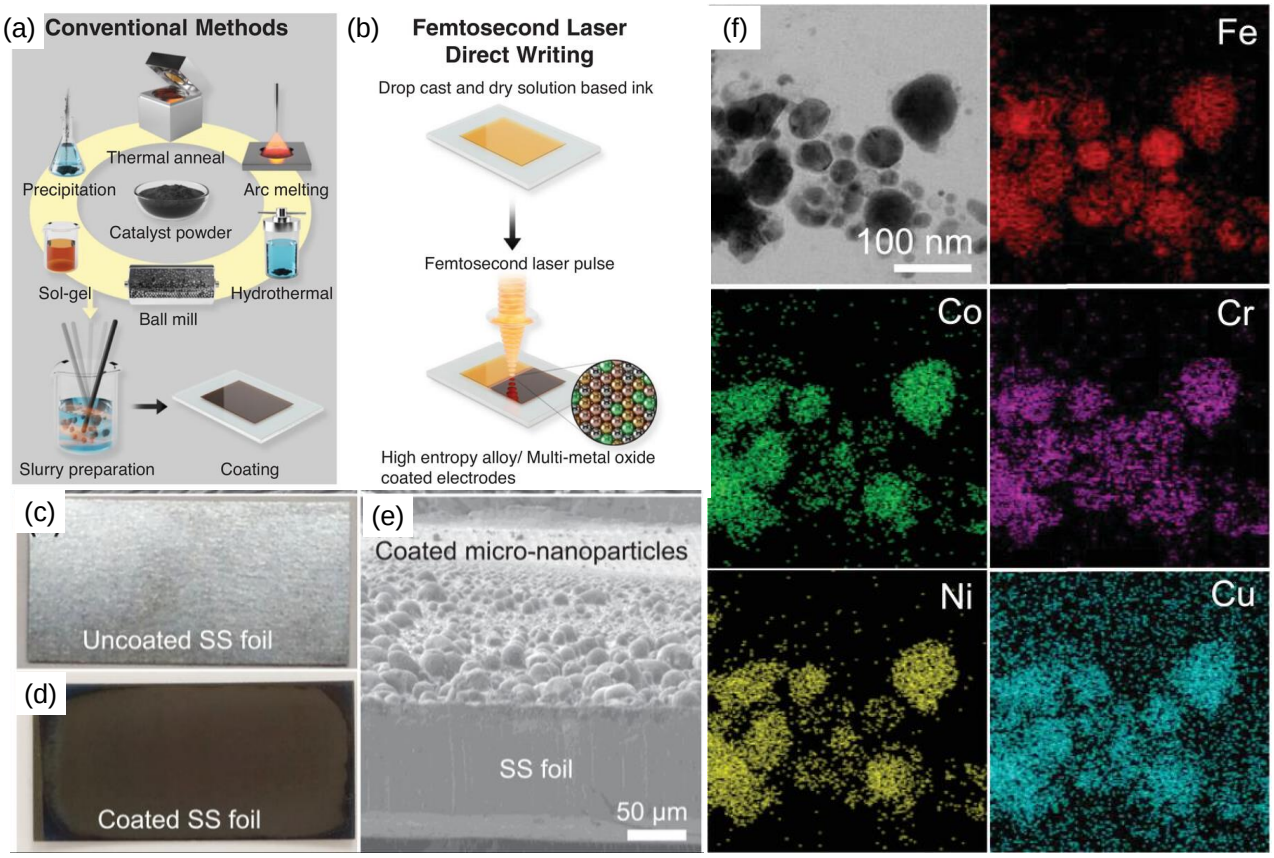

Figure 22. (a) Conventional processes of electrode fabrication and (b) with the FsLDW method. (c,d) Field emission-SEM images of FsLDW pattern on (c) bare stainless steel foil, and (d) Stainelss steel foil coated with Ni by FsLDW. (e) Cross-section SEM view of the stainless steel foil coated with Cu using FsLDW. (f) STEM image, and corresponding STEM-EDS elemental mapping images of Ni, Co, Cu, Fe, and Cr of HEAs. Reproduced with permission.[91] Copyright 2022, Wiley-VCH GmbH.

3.1.4. Simultaneous milling: mechanochemical

An alternative approach to limit particle growth during HEM formation at high temperatures, and thereby maintain particles in the nanometer scale, involves incorporating a milling process during the reaction. In this approach, known as mechanochemical synthesis, the HEM forms through the incorporation of different elements while particles are constantly mechanically eroded or broken in a process that reaches temperatures above 1000 ºC.[93] The mechanical forces involved in particle fragmentation not only prevent the formation of large particles but also induce chemical reactions between precursor materials. This method offers several advantages, including high levels of mixing and homogenization of constituent elements, reduced environmental impact, potential scalability, and the ability to combine and react a wide range of materials without solubility limitations. Ball milling is commonly used for the synthesis of HEM materials, where elements with disparate properties, including different atomic sizes, electronegativities, and melting points, are mixed to create HEMs that wouldn't form through conventional methods. During ball milling, strong collisions and friction

occur between the balls and reactants, leading to repeated welding and breaking processes, which form bonds and result in uniform mixing of the atoms. Overall, the milling process provides energy to react, limits particle size, and homogenizes composition. As drawbacks, mechanochemical approaches generally require a long milling time and can introduce impurities or contamination from the milling tools as well as atmospheric oxygen and nitrogen. Besides, it does not allow control of the particle morphology.

As an example, amorphous Ge-Sn-Sb-Si-Fe-Cu-P high entropy phosphides with sizes around 100 nm were synthesized by high-energy mechanical ball milling.[94] Pure metals and phosphorus were milled continuously for 15 h at 400 rpm in a glove box to prevent oxidation. Similarly, spherical $(CoNiMnZnFe)_3O_3$ HEOs with sizes of 100-200 nm were produced by ball milling different metal powders for 60 h at 500 rpm (**Figure 23**).[95] Ball milling is also often combined with other techniques to obtain HEM NPs. Ashwini et al. combined ball milling with sonication-assisted exfoliation to synthesize NiFeCrCoCu HEA NPs loaded on graphene.[96] Additionally, FeCoNiCuZn HEA was produced by high-frequency electromagnetic field-assisted ball milling at 200-300 kHz, 800 W power, and 258 rpm for 120 h.[97]

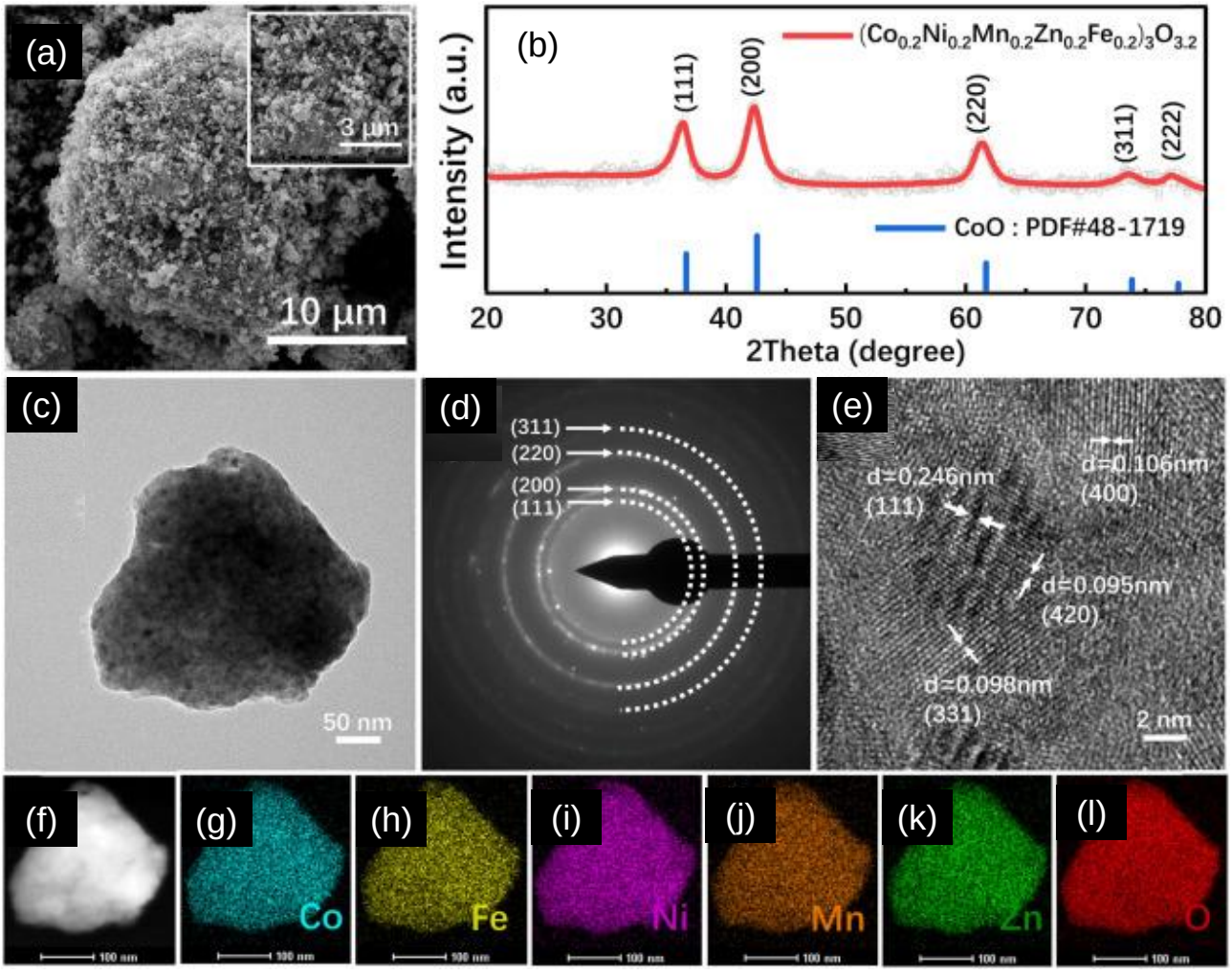

Figure 23. (a) SEM image; (b) XRD pattern; (c) TEM image; (d) SAED pattern; (e) HRTEM image; (f) HAADF-STEM image and (g–l) elemental mappings of Co, Fe, Ni, Mn, Zn and O elements in $(CoNiMnZnFe)_3O_3$ HEOs NPs. Reproduced with permission.[95] Copyright 2021, Elsevier B.V.

3.2. Kinetics-driven HEM formation

An alternative to the high-temperature processing typically used to enhance the entropic term for thermodynamically driven HEM growth is to kinetically drive the process. Kinetically driven approaches focus on rapidly reacting different elements to prevent the system from settling into more thermodynamically stable phases. For successful HEM NP formation, it is crucial that all reagents encounter each other and react simultaneously, enabling the direct formation of the HEM phase while bypassing unwanted intermediate phases. Kinetic control of HEM NP formation can be achieved through three main approaches: i) pre-condensing a random element dispersion into precursor particles followed by crystallization at moderate temperatures; ii) fast triggering the reaction of a homogeneous dispersion of elements through high reaction temperatures, rapid addition of a highly reactive precursor or strong reducing agent, applying a reducing plasma, or injecting charge at a suitable potential; iii) using a highly diluted precursor solution to minimize the probability of interaction of affine species. Some mechanochemical processes could be also considered in this section, but since they were discussed in the previous chapter, they are omitted here.

Despite the potential for kinetically driven HEM NP formation during rapid thermal annealing, the present section will not revisit the high-temperature processes discussed earlier. Instead, it will focus on examples where mixing entropy likely plays a minimal role. Specifically, it will touch on the rapid heating rates achievable through fast-moving bed pyrolysis, but the main emphasis will be on solution-based strategies. The most evident examples of kinetically-driven HEM formation involve synthesizing HEM NPs in solution, where NP growth is constrained by moderate temperatures and the natural phase separation between evolving nuclei in the liquid phase (**Figure 24**). These conditions allow for controlled, simultaneous reactions that favor the formation of HEM NPs without the need for high entropic contributions. The primary challenge, instead, lies in balancing the reactivity and interaction of the different precursors.[98]

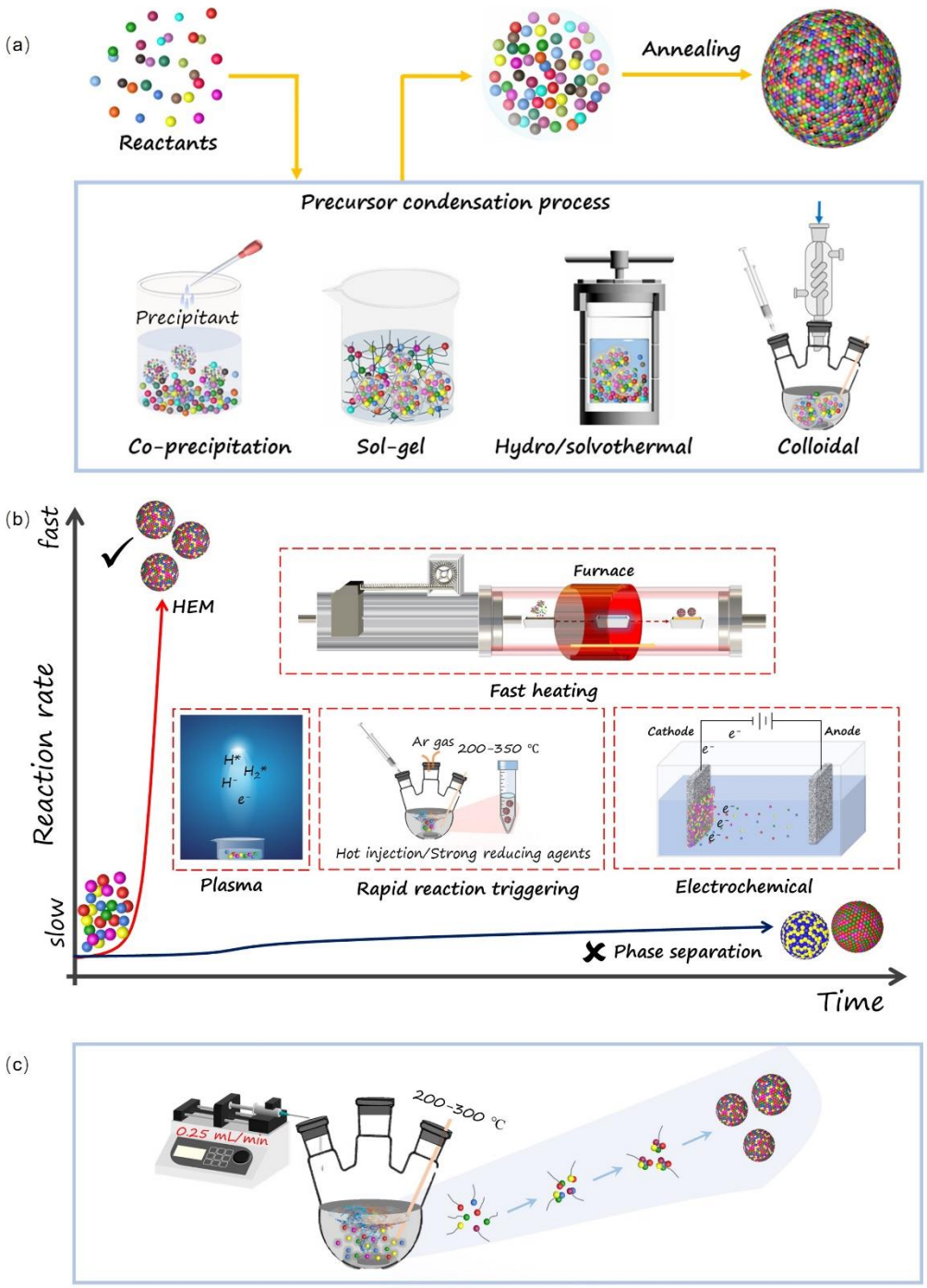

Figure 24. HEM NPs produced strategy by kinetic-driven process. (a) Condensing the different elements into precursor NPs with different methods, followed by a crystallization treatment at a moderate temperature, preventing NP growth and phase separation. (b) Fast reaction at moderate temperature. (c) Using a highly diluted solution to minimize precursor collisions.

3.2.1. Precursor condensation with post-annealing

HEM NPs can be synthesized by first condensing different elements into precursor NPs at low temperatures, followed by a moderate-temperature crystallization step that prevents particle growth and phase separation. The element condensation usually occurs in a liquid medium, offering better element mobility than solid-state processes and greater control compared to rapid gas-phase methods.

The subsequent thermal treatment does not need to be ultrafast as the HEM phase is considered to be kinetically formed and stabilized by the high energy barrier for atomic reorganization within the particle. Additionally, this annealing process is typically conducted on solid-state nanopowder, not requiring a support, which enables large-scale production of unsupported NPs. High crystallization temperatures are also unnecessary since the elements are already randomly organized within the NPs; in fact, high temperatures could lead to unwanted phase segregation and particle growth/fusion. During thermal annealing, NP growth is restricted by limited ion diffusion in the solid phase at the moderate temperatures used. Various wet-chemistry techniques, such as co-precipitation, sol-gel, and colloidal synthesis, can be employed to produce the precursor NPs. Condensation can be triggered by gently heating a homogeneous precursor solution, adjusting pH, or introducing chelators, reactants, or reducing agents.[99] Heating can be applied using heating mantles, oil baths, or microwave radiation. The synthesis can be performed in batches or continuously in flow reactors, with the resulting NPs stabilized in solution using surfactants or precipitated. Additionally, pressure can be applied within hydrothermal/solvothermal reactors. Numerous examples exist in the literature of HEA NP preparation using these solution-based methods followed by post-annealing.[100]

As an example, Talluri et al. produced $(CoCrFeMnNi)_3O_4$ HEO NPs via co-precipitation followed by crystallizaton at 750 °C for 30 min.[101] Metal precursors were dissolved in water and precipitated using ammonia, with the product then calcined. Lai et al. produced HEP NPs using a sol-gel method, where metal chlorides, $NH_4H_2PO_4$, and citric acid were mixed, dried into a gel, and then annealed in a two-step process: first at 300 °C in a 5% H_2/Ar atmosphere, followed by 900 °C heating. The resulting phosphide NPs were around 300 nm with a hexagonal M_2P phase (**Figure 25 a,b**).[100d] Kheradmandfard et al. used microwave irradiation to prepare MgCuNiCoZnO HEO NPs by dissolving metal nitrates in water, making the solution alkaline, and then irradiating it at 850 W for 3 min, followed by annealing at 950 °C (**Figure 25c**).[100e] In this process, the metal ions initially formed primary amorphous HEO particles under microwave irradiation, which then crystallized during the subsequent annealing step.

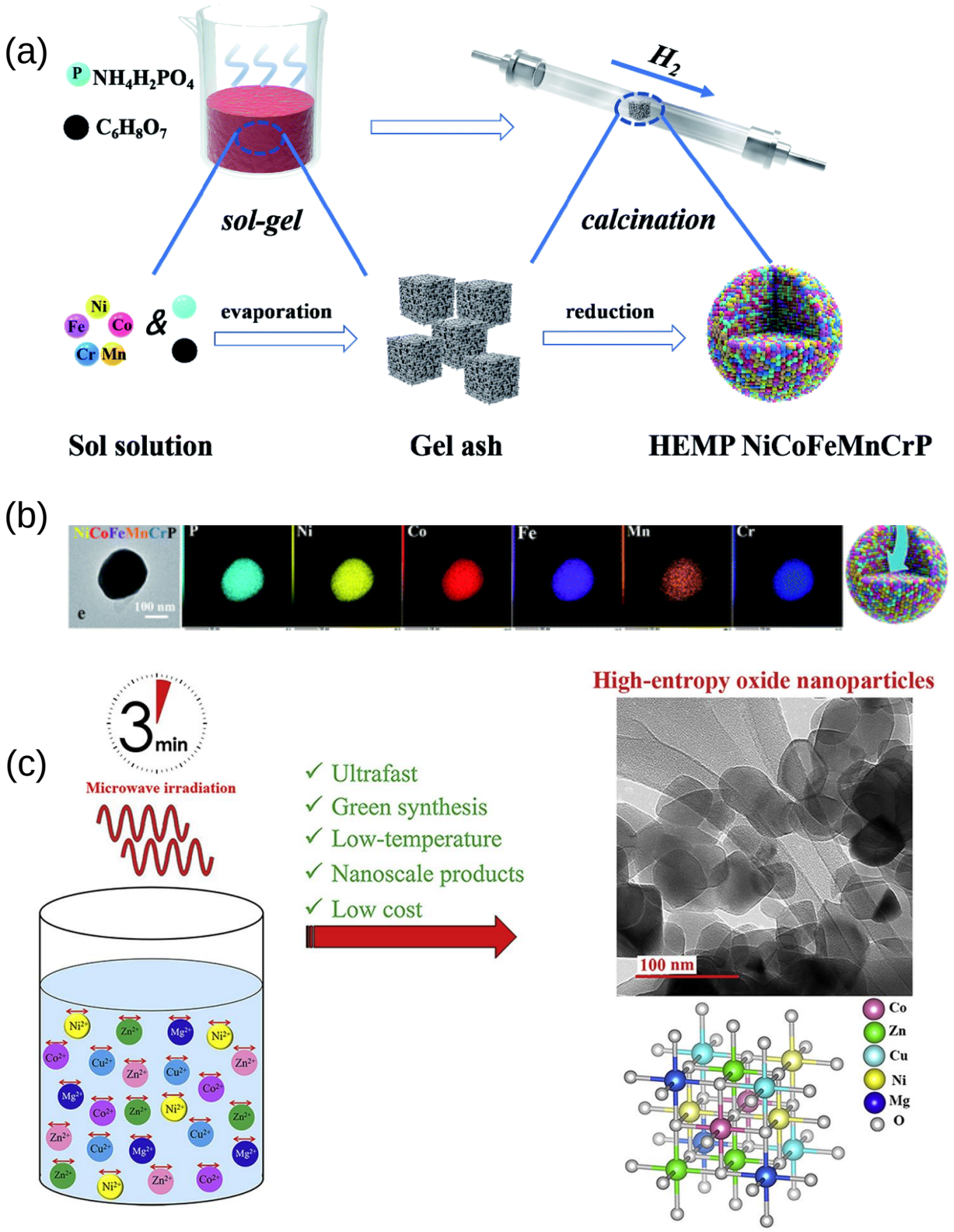

Figure 25. (a) The synthesis process of NiCoFeMnCrP NPs through the sol–gel method and calcination reduction strategy. (b) TEM images and the corresponding element mapping images of NiCoFeMnCrP NPs. Reproduced with permission.[100d] Copyright 2013, American Chemical Society. (c) Schematic illustration of the synthesis process of MgCuNiCoZnO HEO NPs using microwave irradiation. Reproduced with permission.[100e] Copyright 2021, Elsevier.

3.2.2. Fast reaction at moderate temperatures

Crystalline HEM NPs can also be produced directly at moderate temperatures without the need for a two-step pre-condensation and crystallization process. To kinetically drive low-temperature HEM crystallization while preventing secondary phase formation, it is crucial that all elements are homogeneously dispersed and react rapidly and simultaneously. This can be achieved with metal components that have similar redox potentials to ensure simultaneous co-reduction, or with carefully selected precursors with matching reactivity to achieve uniform co-reaction. Besides, the co-reduction/reaction can be forced through rapid heating, strong reducing agents, including a reducing plasma, or charge injection at an appropriate potential.

3.2.2.1. Fast heating of a solid precursor mixture: Fast-moving bed pyrolysis

As noted earlier, the fast thermal processing approaches described in section 3.1 meet the criteria for kinetically driven HEM NP growth by supplying sufficient energy to kinetically trap the random atomic distribution within the precursor mixture. However, those methods will not be revisited here. An example of kinetically-driven HEM NP formation through relatively rapid heating of a homogeneous solid precursor mixture, here the fast-moving bed pyrolysis (FMBP) method is considered. In FMBP, mixed precursors are simultaneously reacted by quickly placing them into a pre-heated reactor or tube furnace. A simultaneous reduction process may be necessary. The temperatures in FMBP are typically below those required for a substantial entropic contribution. These moderate temperatures avoid substantial NP growth. Additionally, precursors are often dispersed on high surface area supports to further minimize particle growth and aggregation. However, as in Section 3.2.1, while rapid heating is required for the simultaneous reaction of precursors, the annealing process does not need to be ultrashort, as the HEM phase is considered to be kinetically formed and stabilized by the high energy barrier for atomic reorganization within the particle.

As an example, Gao et al. synthesized quinary to denary HEA NPs loaded on different supports (GO, Al_2O_3, zeolite, carbon black) using the FMBP strategy.[102] As shown in **Figure 26**, metal precursors were first loaded onto the support via wet impregnation. The loaded samples were placed in a quartz boat outside the furnace zone, preheated to 923 K under Ar. The quartz boat was rapidly pushed into the furnace within 1 second, and the reaction proceeded for 120 min. Heat transfer simulations showed that the precursors on GO reached 920 K within 5 seconds, with minimal heat loss (~3 K) due to the quartz boat. This rapid heating allowed simultaneous pyrolysis, forming small nuclei clusters and preventing phase separation. In contrast, when using a fixed bed pyrolysis reactor with a slower heating rate (20 K/min), the precursors reduced sequentially due to varying reduction potentials, leading to phase-separated NPs.

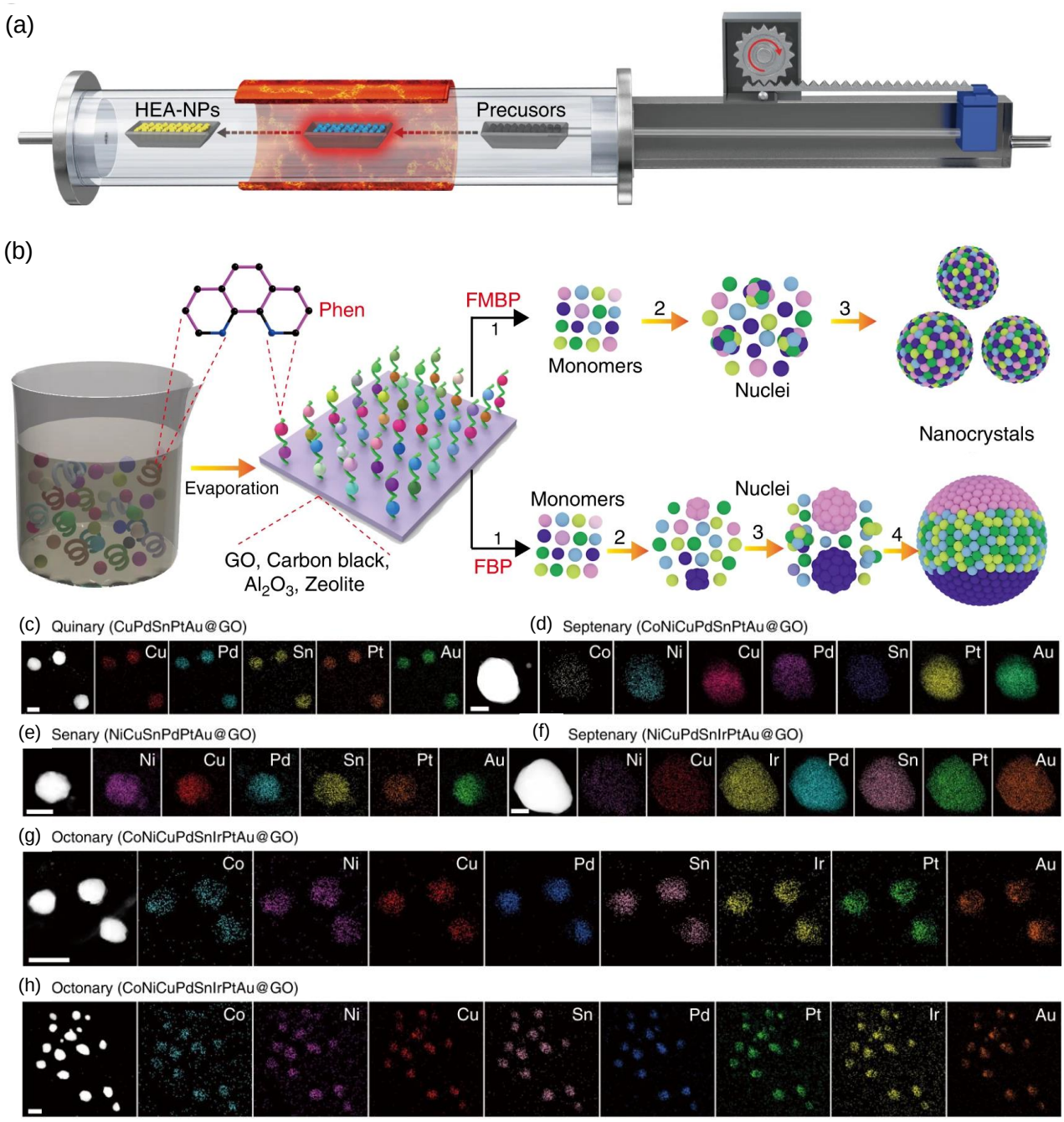

Figure 26. (a) Schematic diagram of the FMBP experimental setup used to produce HEA NPs. (b) Schematic diagrams for the synthesis of homogeneous and phase-separated HEA NPs by FMBP and fixed bed pyrolisis strategies. (c-h) HAADF and elemental maps for (c) the quinary (CuPdSnPtAu), (d) senary (NiCuPdSnAuPt), (e) septenary (CoNiCuPdSnPtAu), (f) septenary (NiCuPdSnIrPtAu), (g) octonary (CoNiCuPdSnIrPtAu) and (h) denary (MnCoNiCuRhPdSnIrPtAu) alloy. Scale bar (c–e, g, h) 50 nm, (f) 20 nm. Reproduced with permission [102] from CC- BY.4.0. open access publications.

3.2.2.2. Rapid triggering of reaction in solution

The direct formation of HEM NPs in solution, without a post-annealing step, allows for greater control over NP characteristics. In this context, colloidal synthesis strategies are especially effective, making them the focus of this section. At the relatively low temperatures used in solution-phase methods, the simultaneous reaction of different elements particularly relies on selecting compatible

precursors that can co-react or co-reduce.[103] This process is facilitated by using strong reactants, reducing agents, or sufficient thermal energy to initiate the simultaneous reaction. In colloidal synthesis, this is often achieved through the hot injection of either the precursor or the reductant.[104]

One of the pioneering works on the colloidal synthesis of HEM NPs using a kinetically driven approach was conducted by Singh et al, who produced CrFeCoNiCu NPs in a mixture of oleic acid and oleylamine, using lithium triethylborohydride as a strong reducing agent to achieve the simultaneous incorporation of all elements into the growing NPs.[104a] Yu et al. produced PtPdFeCoNi HEA NPs with the size of 12±4 nm by using metal acetylacetonates as the precursors, oleylamine and L-ascorbic (L-AA) as the reduction regent by a hot injection at 280℃ (**Figure 27 a-e**).[104b] Wu et al. used the hot injection of reactants to synthesize noble metal HEAs, including RuRhPsOsIrPt[105], IrPdPtRhRu[106], and even up to RuRhPdAgOsIrPtAu NPs[107]. They injected an equimolar mixture of metal precursor solutions into a preheated trimethylene glycol (TEG) solution containing PVP as a stabilizer at 230 ℃. Sun et al. synthesized AuAgCuPtPd HEA NPs by co-reduction of metal salts with sodium borohydride in the presence of thiolated polymer ligands at room temperature.[108]

Broge et al. investigated the formation process of Pt-Ir-Pd-Rh-Ru HEA NPs using *in situ* X-ray scattering and TEM techniques.[109] The reduction temperatures of the individual metal precursors for Pt, Ir, Pd, Rh, and Ru were 200°C, 350°C, 150°C, 250°C, and 200°C, respectively. Temperature played a critical role in synthesizing single-phase Pt-Ir-Pd-Rh-Ru HEA NPs. At higher temperatures (⩾300 °C), HEAs with a secondary phase were obtained, while lower temperatures resulted in inhomogeneous elemental distributions. A narrow temperature window around 200 °C was found to be optimal for producing a homogeneous HEA. The formation process was studied at 200°C for 77 min, during which only Pt, Pd, and Ru initially precipitated. These early-formed nuclei catalyzed the reduction of the remaining metal ions, facilitating the growth of the HEA. The unit cell parameter remained unstable for the first 10 min, indicating the nucleation process. After 10 min, the unit cell parameter stabilized, suggesting that the composition of the growing crystalline NPs remained consistent as all five metal precursors precipitated at constant rates.

Beyond batch-based synthesis, HEM NPs can also be produced using flow reactors. Flow chemistry offers advantages over traditional batch methods, such as faster mixing of reductants and precursors and precise control over the reaction conditions, leading to better selectivity and reproducibility. This method allows for the dissolution of multiple cations in separate solutions, which are then precisely mixed via designed flow pathways, ensuring uniformity in the nucleation and growth stages. As an example, Minamihara et al. developed a continuous-flow system to produce HEA NPs by flowing metal precursors and reducing agents separately, allowing them to react at a

controlled mixing point, thus ensuring the simultaneous supply of constituent atoms during nucleation and growth (**Figure 27 f, g**).[110] Using this approach, they synthesized ultra-small IrPdPtRhRu HEA NPs with an average size of just 1.32 nm, corresponding to around 50 atoms per particle.

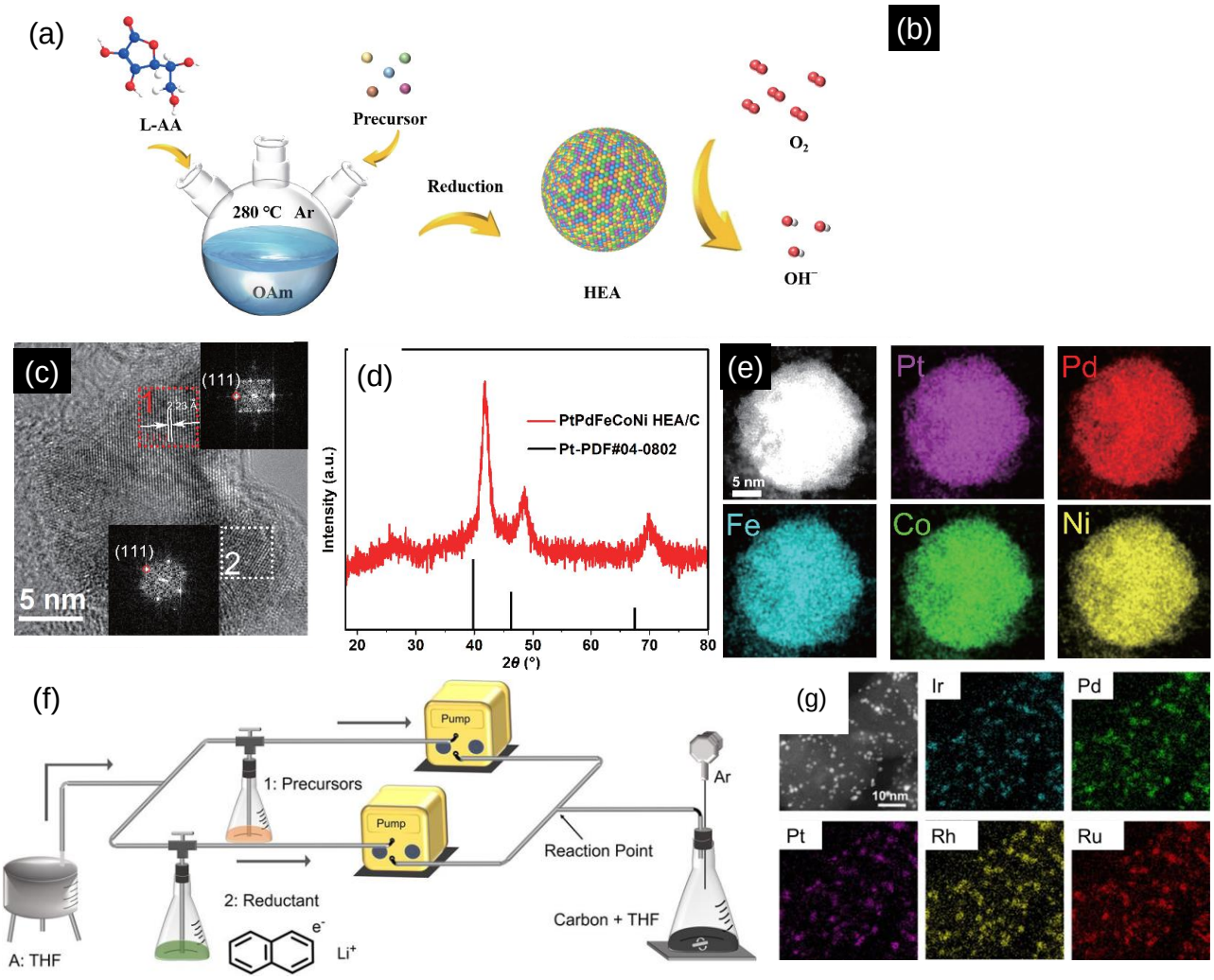

Figure 27. (a) Scheme of the synthesis of PtPdFeCoNi HEA NPs. (b) TEM image of PtPdFeCoNi HEA NPs. The inset shows the corresponding SAED pattern. (c) HRTEM image of PtPdFeCoNi HEA NPs. Regions 1 and 2 represent different crystal domains and insets show the corresponding FFT patterns. (d) XRD pattern, and (e) STEM-EDS mapping images of PtPdFeCoNi HEA NPs. Reproduced with permission.[104b] Copyright 2022, Tsinghua University Press. (f) Schematic of the developed continuous-flow reactor. (g) HAADF-STEM image of the IrPdPtRhRu HEA NPs produced and corresponding EDS maps. Reproduced with permission.[110] Copyright 2022, American Chemical Society.

3.2.2.3. Plasma as a strong reducing agent

A plasma can serve as a powerful reducing agent, facilitating the rapid and kinetically controlled reduction of a homogeneously dispersed mixture of multiple elements to produce HEM NPs. The reactants can be supported in a solid phase or dissolved within an ionic liquid, in a wet plasma reduction set-up.[111] In the wet plasma reduction setup, the combination of plasma technology with

ionic liquids offers several advantages. The ionic liquid not only acts as a solvent that stabilizes the reactants but also enhances the mass transport properties, ensuring that the reactants remain well-dispersed and accessible for interaction. Moreover, the unique characteristics of plasma, including its high-energy density and reactive species generation, facilitate the breaking of chemical bonds in the reactants, leading to efficient reduction. The kinetic control provided by the plasma environment ensures that the nucleation and growth of HEM NPs occur under favorable conditions, resulting in HEM NPs with desirable size, morphology, and compositional uniformity.

As an example, Wu et al. synthesized PtCrTaVFeAl HEA NPs using hydrogen cold plasma as a reduction agent at ambient conditions (**Figure 28 a-f**).[112] The process involved dissolving metal precursors in deionized water, followed by vacuum treatment to remove moisture. The dried mixture was then loaded into a custom dielectric barrier discharge reactor, purged with Ar gas for 20 min to eliminate residual oxygen, and then flushed with H_2 gas for an additional 15 min. The mixture was subjected to hydrogen cold plasma at atmospheric pressure for 10 min at 90 W. The reactive species generated in the hydrogen plasma, including H-, H_2*, and H*, rapidly reduced the metal ions to zero-valent metal atoms, enabling instant and simultaneous nucleation. This burst nucleation, followed by random atomic deposition, ensured uniform atomic mixing across different elements, leading to the formation of HEA NPs. The NP size could be modulated by adjusting the plasma power. Similarly, Lee et al. developed a mild and environmentally friendly plasma ionic liquid reduction strategy to produce IrPdPtRhRu HEA NPs (**Figure 28g**).[111] Metal precursors were dispersed in 2 mL of an ionic liquid ([BMIM]TF_2N) to create a homogeneous suspension. The mixture was then exposed to an atmospheric plasma, with a gas flow of 5 L/min Ar and 0.1 L/min H_2, under a radio frequency (RF) power of 225 W for 15 min. In this setup, argon ions (Ar^+), hydrogen radicals (H^*), and electrons (e^-) in the plasma acted as powerful reducing agents, enabling the simultaneous reduction and incorporation of different elements into the HEA structure.

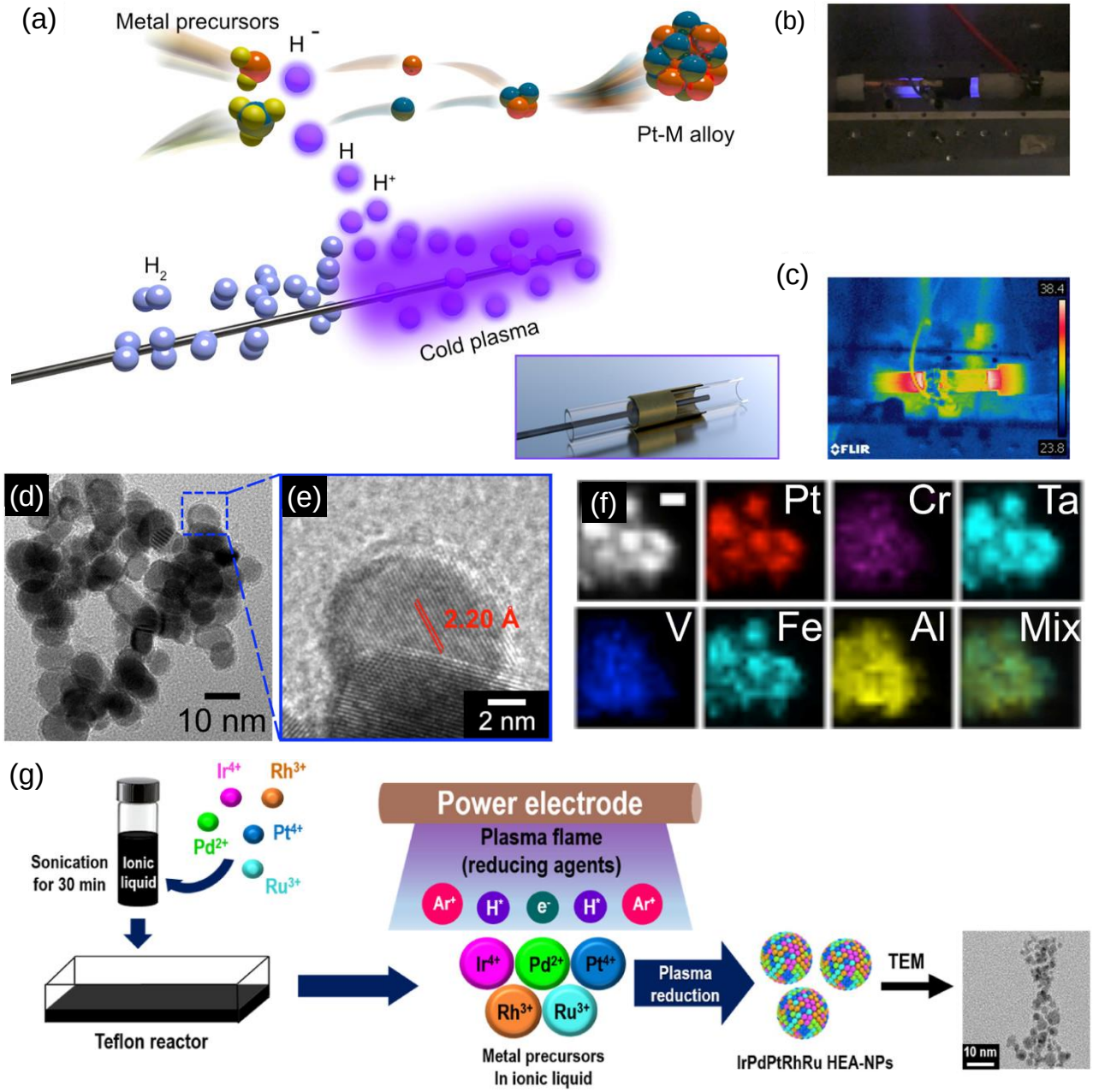

Figure 28. (a) Schematic illustration of hydrogen cold plasma synthesis of HEA NPs. The inset shows a dielectric barrier discharge reactor. (b) Plasma generator in operation, emitting glowing H_2 cold plasma. (c) Infrared thermal image of the dielectric barrier discharge reactor taken after 10 s of operation. (d) TEM, (e) HRTEM, and (f) STEM-EDS elemental mappings of PtCrTaVFeAl HEA NPs. The scale bar in the STEM image is 5 nm. Reproduced with permission.[112] Copyright 2021, American Chemical Society. (g) Schematic illustration of the synthesis process of IrPdPtRhRu HEA NPs using a wet plasma reduction method. Reproduced with permission.[111] Copyright 2022, Elsevier Inc.

3.2.2.4. Electrochemical deposition

Another approach to trigger a rapid reaction of a homogeneous dispersion of element precursors, kinetically driving the formation of HEM NPs, is to simultaneously reduce all the precursor ions electrochemically, i.e. injecting charge at a proper potential. In the electrochemical approach, metal

salts are dissolved in an electrolyte solution, and an electric potential is applied between a substrate (cathode) and a separate electrode (anode). Positive metal ions migrate toward the cathode and are reduced, forming clusters and eventually NPs on the cathode surface. Key factors such as applied voltage, current density, temperature, and electrolyte composition influence the size, shape, and composition of the resulting NPs. This method offers a straightforward route to synthesize HEMs, particularly those containing high melting point elements, making it a versatile technique for HEM production.[113]

For example, Ritter et al. synthesized MnCaFeNiMg high entropy metal hydroxide and oxide NPs via electrodeposition at various current densities (10, 116, and 232 mA/cm^2) at room temperature using Cu foil as the cathode and a carbon rod as the anode, with metal salts in water as the electrolyte.[114] As shown in **Figure 29 a-c**, the synthesis occurs in two steps: first, water was reduced to H^+ and OH^- at the cathode; then, these ions combined with metal ions to form high entropy hydroxide, then with post-calcination process transformed hydroxides into HEO NPs. Dong et al. synthesized FeCoNiMnZn high-entropy metal-organic framework (HE-MOF) NPs by coordinating all metal ions simultaneously with organic ligands via electrodeposition.[115] Mixed metal salts and 2-methylimidazole (HmIM) in a methanol-H_2O solution served as the electrolyte. The reaction at -2.5 V vs. $E_{Ag/AgCl}$ for 400 s produced amorphous HE-MOF NPs sized 60-120 nm. At high potential, H_2O and HmIM deprotonated at the cathode, forming mIM^- and OH^-, which enabled random coordination of metal ions to form HE-MOFs.

The cathodic electrodeposition method for producing NPs faces three major challenges. First, preferential nucleation at energetically favorable sites results in uneven coverage on the electrode surface, leading to inconsistencies in NP size, distribution, and composition. Second, overlapping diffusion layers between adjacent NPs further accentuate to size polydispersity. Third, variations in the electrodeposition potentials of different metal precursors cause stoichiometric discrepancies, as some metals are deposited in higher concentrations than others.[116] To address these challenges, Glasscott et al. introduced a nanodroplet-mediated electrodeposition technique, confining metal salt precursors within water nanodroplets to localize nucleation and growth.[117] The process involves a rapid electro-shock event lasting around 100 ms, enabling the simultaneous reduction of up to eight metal salts into high-entropy metallic glasses with precisely controlled stoichiometric ratios (**Figure 29 d-g**).

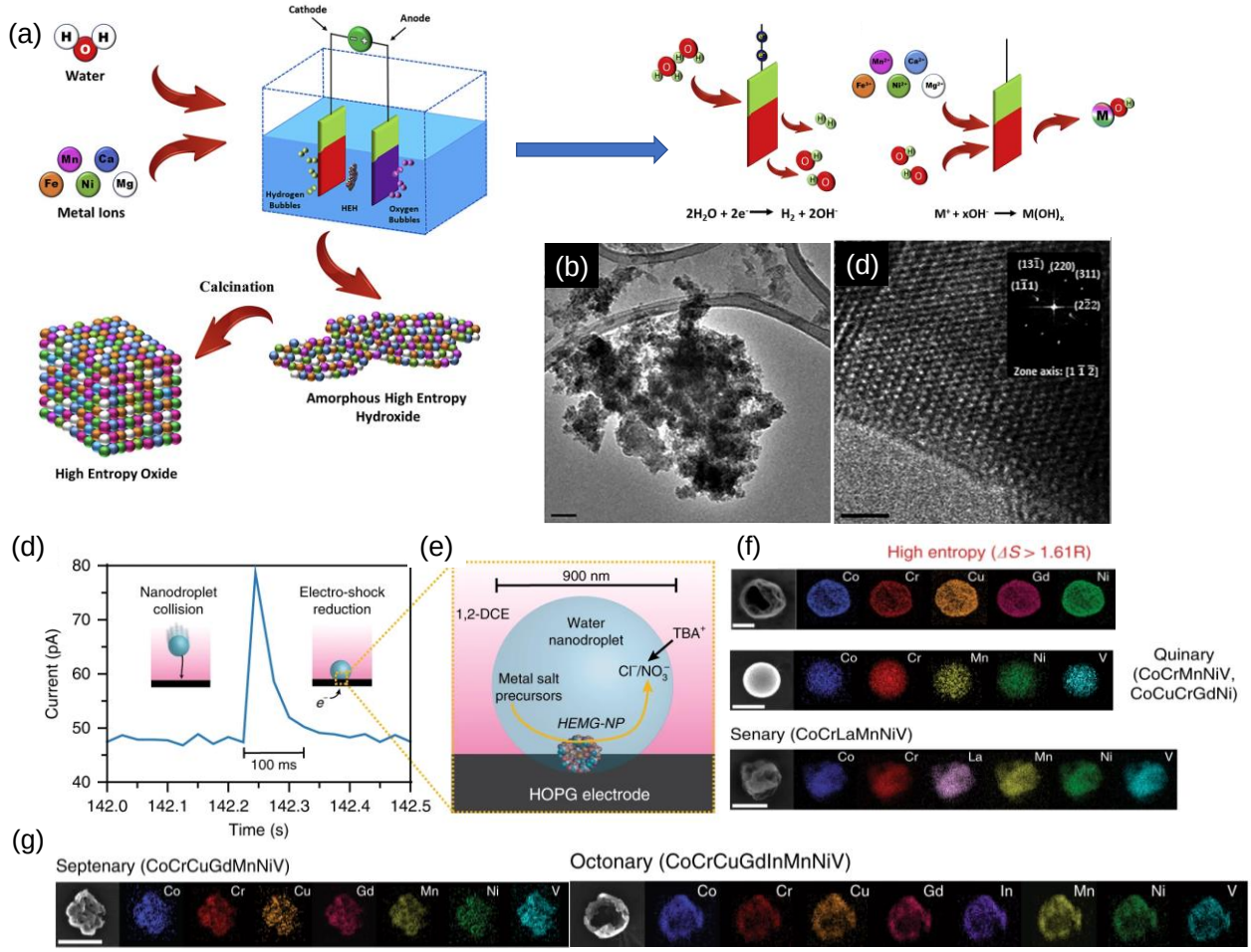

Figure 29. (a) The proposed mechanism for the formation of MnCaFeNiMg metal hydroxide and oxides NPs under high current density. (b) HRTEM image of MnCaFeNiMg metal hydroxide NPs (scale bar, 50 nm). (c) HRTEM of calcined MnCaFeNiMg HEO NPs at 800 °C for 3 h in air (scale bar, 2 nm) with inset of an FFT analysis indicating the selected planes corresponding to the spinel cubic metal oxide crystal structure. Reproduced with permission [114] from CC- BY.4.0. open access publications. (d) Current transient corresponding to the collision of a single nanodroplet onto a carbon fiber ultramicroelectrodes (r_{UME} = 4 µm) biased at −0.4 V vs. Ag/AgCl. Nanodroplet contents are fully (>98%) reduced within 100 ms, facilitating disordered co-deposition of various metal precursors. (e) Representation of a nanodroplet collision event highlighting the rapid NP formation at the water/substrate interface and the charge balance. (f) EDS images of HEM NPs (ΔS > 1.61 R) of quinary and senary alloys. (g) EDS images of HEM NPs (ΔS > 1.61 R) of septenary and octonary alloys. Reproduced with permission [117] from CC- BY.4.0. open access publications.

3.2.3. Highly diluted solutions to minimize precursor collisions

An alternative to triggering a rapid reaction of different precursors is to prevent phase segregation by reducing collisions between atoms of the same or highly affine elements. In this scheme, counterintuitively, the synthesis of HEM NPs can be kinetically driven by maintaining the reactants separated through highly diluted precursor solutions. This can be achieved by slowly injecting the precursors as they are consumed during HEM NP nucleation and growth. By precisely

controlling the injection rate, this approach keeps the precursor concentration low, reducing the likelihood of a critical number of atoms of affine elements meeting together to nucleate a more thermodynamically favorable secondary phase.

This approach was recently proposed and experimentally validated by Dey et al.[98] and Soliman et al.[9d] Soliman et al. synthesized (Pd,Rh,Ir,Pt)Sn nanoflowers by slowly injecting a metal reagent solution at 0.25 mL/min into heated oleylamine and octadecene at 315 °C. [9d]To understand the NP formation, they conducted a time-resolved study by quenching the reaction at different stages (**Figure 30**). Initially, at 30 s, Pd-rich cube-like seeds formed, with Rh, Ir, Pt, and Sn depositing at the corners. By 2 min, a high-entropy phase was deposited on the Pd-rich cores, with the emergence of a NiAs intermetallic phase. At 8 min, the particles developed a flower-like structure with outward growth. By 16 min, the synthesis was complete, yielding nanoflowers with a single-phase Ni_2In structure. STEM-EDS mapping confirmed a homogeneous distribution of all five elements, indicating full Sn diffusion into the particle core and the transformation of Pd seeds into (Pd,Rh,Ir,Pt)Sn nanoflowers. Liu et al. used a similar strategy to produce PtPdRhIrRu NPs by introducing the metal precursor solutions into the reaction solution slowly using a syringe pump.[118]

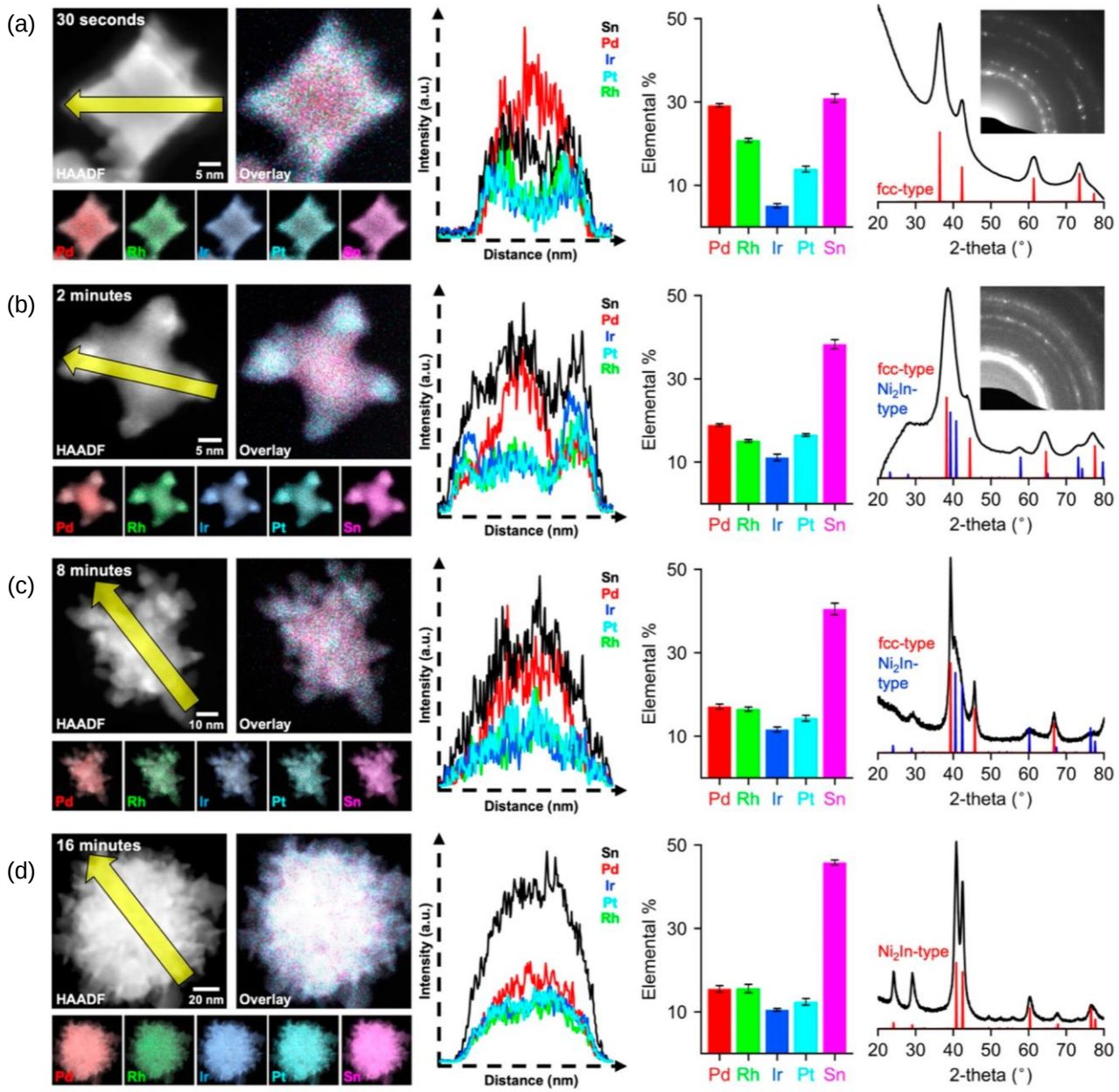

Figure 30. Time-dependent formation of (Pt,Rh,Ir,Pt)Sn NPs at (a) 30 s, (b) 2, (c) 8, and (d) 16 min. Each time point includes a representative HAADF-STEM image with corresponding overlaid STEM-EDS element maps for Pd, Rh, Ir, Pt, and Sn, along with a composite overlay of all elements. Additionally shown are line scan profiles across the particle (indicated by the yellow arrow), a histogram based on ensemble EDS analysis, an XRD pattern, and a corresponding SAED pattern. Reproduced with permission.[9d] Copyright 2023, American Chemical Society.

3.3. Enthalpy-driven HEM formation

Initial attempts to synthesize HEM NPs directly from atomic/ionic/molecular precursors (bottom-up) closely followed the methodologies used for bulk HEMs, based on the assumption that the high entropic contribution would stabilize the multielement phase against potentially more thermodynamically stable phases with lower formation enthalpies. However, unlike bulk synthesis, these NP-focused approaches incorporated additional strategies specifically aimed at preventing

excessive growth, as discussed in section 3.1. A subsequent common approach aimed at kinetically driving HEM NP formation aided by the preorganization of a homogeneous mixture of the elements (section 3.2.1), triggering a rapid reaction (section 3.2.2), or minimizing interactions between affine elements (section 3.2.3).

Over the past two decades, numerous studies have suggested that thermodynamically driven HEM formation can occur with minimal contribution from entropy. Indeed, the enthalpy change associated with forming a HEM from a homogenous mixture of elements can be significantly lower than the energy required to form multiple segregated phases in NP form, where surface, interphase, and solvation energies are substantial. Additionally, enthalpy may play a critical role not only in driving the formation process but also in ensuring stability at ambient temperature, where the contribution of entropy is secondary, for HEM NPs produced at higher temperatures.

In contrast to the synthesis of bulk HEMs where the free energy of mixing, derived from the enthalpy and entropy of mixing ($\Delta G_{mix} = \Delta H_{mix} - T\Delta S_{mix}$),[54] has traditionally been considered the key factor in determining the HEM phase formation, the growth of HEM NPs from a homogeneous mixture of precursors requires consideration of additional factors. In the growth of a HEM NP from a uniform metal ion solution:

$$\Delta G_{HEM} = \Delta H_{HEML} + \Delta H_{HEMS} - \Delta H_{SOL} - T(\Delta S_{HEML} + \Delta S_{HEMS} - \Delta S_{SOL})$$

Where ΔH_{HEML} and ΔH_{HEMS} are the HEM lattice and surface enthalpies, ΔH_{SOL} is the enthalpy of the constituent solvated ions, and ΔS_{HEML}, ΔS_{HEMS}, and ΔS_{SOL} are the corresponding entropies. The change of entropy associated with the formation of a HEM from a uniform metal ion solution at ambient temperature is negligible. Thus, considering the growth of a spherical HEM NP with radius r, lattice atomic density ρ, surface atomic density σ, average lattice atomic energy γ, and surface atomic energy u, from a metal ion solution with average ionic energy, i.e. chemical potential, μ, the total energy of the system can be expressed as follows:

$$\Delta G_{HEM} = 4\pi r^2\sigma\gamma + \frac{4}{3}\pi r^3\rho u - \frac{4}{3}\pi r^3\rho\mu = 4\pi r^2\sigma\gamma + \frac{4}{3}\pi r^3\rho(u-\mu)$$

As expected, the growth of a HEM can be energetically favored ($\Delta G_{HEM} < 0$) only when $u < \mu$, i.e. when the energy per atom within the HEM lattice is lower than within the solution. In this case, when $u < \mu$, the growth of a bulk HEM, i.e. $r \rightarrow \infty$, is always energetically favored. However, it is well known that a critical radius exists below which the formed nuclei are unstable against dissolution (**Figure 31a**). This critical radius is determined by the balance between the surface energy, which favors dissolution, and the bulk energy, which favors growth:

$$r_c = \frac{3\sigma\gamma}{\rho(\mu - u)}$$

To evaluate the energetically more favorable scenario, either the growth of a homogeneous HEM or the formation of multiple phases, we compare the Gibbs free energy of a spherical HEM NP with that of a similar NP containing two distinct phases, A+B. This comparison also determines the stability of an already formed HEM NP against phase segregation. Assuming the entropy change is negligible at ambient temperature, the difference in Gibbs free energy can be expressed as:

$$\Delta G_{A+B} = \Delta H_{AL} + \Delta H_{AS} + \Delta H_{BL} + \Delta H_{BS} + \Delta H_{ABI} - \Delta H_{HEML} - \Delta H_{HEMS}$$

Assuming an interphase energy lower than the surface energy, the most energetically favorable scenario for the formation of A+B is when the two phases maintain the spherical morphology, so the overall surface area remains constant and only an interphase is created between the two materials. In this case, assuming the simplified case of equal volumes for the two phases and similar surface and bulk atomic densities, the change in Gibbs free energy for segregation can be expressed as:

$$\Delta G_{A+B} = 2\pi r^2 \sigma \left(\gamma_A + \gamma_B + \frac{\gamma_I}{2} - 2\gamma_{HEM}\right) + \frac{2}{3}\pi r^3 \rho (u_A + u_B - 2u_{HEM})$$

As expected, for a bulk HEM ($r \rightarrow \infty$), the segregation of the two phases is energetically favorable when the average lattice energy of the segregated phases is lower than that of the HEM ($u_A + u_B < 2u_{HEM}$). However, in HEM NPs, surface and interface energies become significant, leading to a radius below which the HEM NP remains stable against phase segregation even if $u_A + u_B < 2u_{HEM}$ (**Figure 31b**). In this simplified case, the critical radius is given by:

$$r_c = \frac{3\sigma \left(\gamma_A + \gamma_B + \frac{\gamma_I}{2} - 2\gamma_{HEM}\right)}{\rho(2u_{HEM} - u_A - u_B)}$$

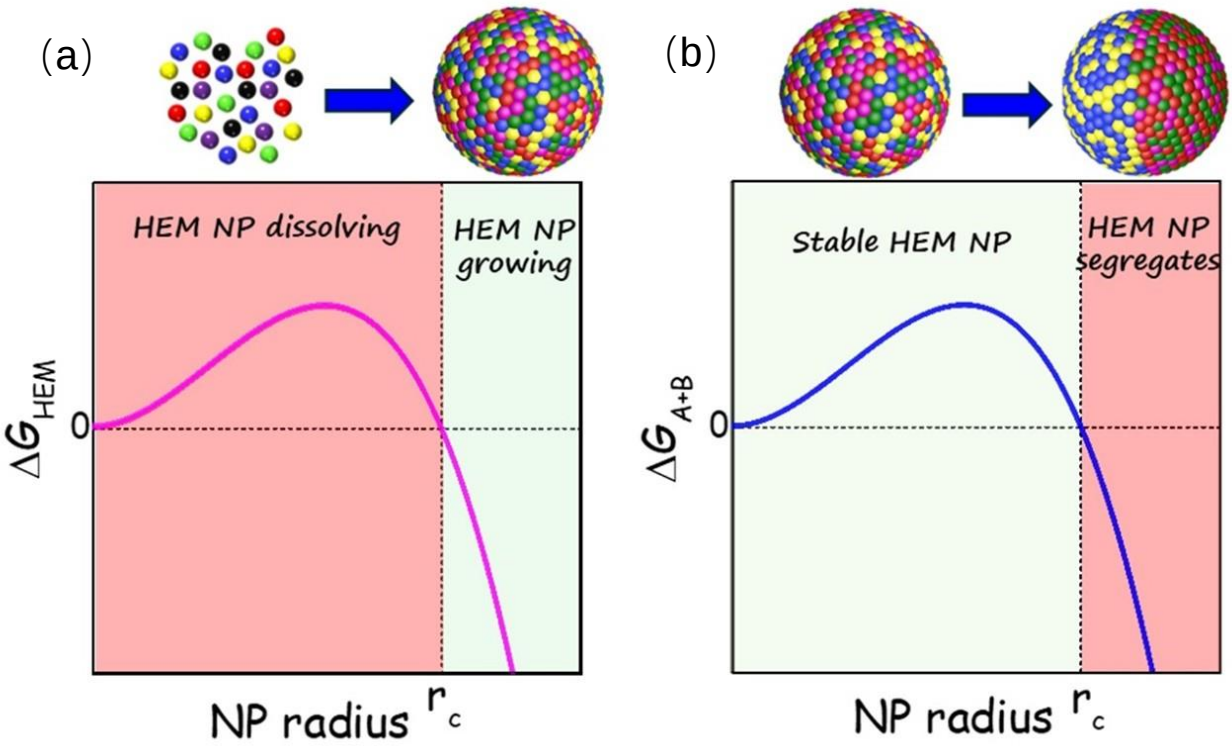

Figure 31. Gibbs free energy change as a function of NP radius for the formation of a spherical HEM NP from a metal ion solution (a) and for the phase segregation of a spherical HEM NP in two hemispherical phases A+B (b).

As anticipated, high interphase energies stabilize the HEM NP against the formation of segregated phases. Additionally, an increase in surface energy with phase formation (not considered in this example) also favors HEM stability. On the other hand, a high HEM surface energy can contribute to destabilizing the HEM structure. However, due to the shorter diffusion lengths and fewer atoms involved, the energy barrier for atomic organization at the HEM surface to minimize surface energy is significantly lower than the energy required to reorganize the entire particle into different phases. In fact, while analyzing the atomic distribution within HEM NPs remains challenging, careful studies of this aspect have revealed that the composition is often far from homogeneous, with certain afine atoms showing preferential organization, particularly at the surface.[9b, 119] In this context, the use of specific ligands could also contribute to stabilizing the HEM NP. Moreover, for a given composition, the average atomic surface energy of smaller NPs tends to be higher than that of larger particles, due to the formation of additional defects and a relatively smaller area of energy-favorable surfaces or facets. This effect further stabilizes smaller HEM NPs against segregation into smaller entities. Nevertheless, in some compositions, lattice energy may be significantly increased by the presence of atoms that differ considerably in terms of charge and/or size, promoting segregation. However, the introduction of additional elements into the HEM can reduce lattice stresses, thereby lowering the lattice energy and stabilizing the HEM through a mechanism different from the

commonly cited entropy-driven stabilization.

Determining the exact mechanisms that stabilize HEM compositions remains challenging; however, numerous studies suggest enthalpy-driven HEM NP formation and stabilization. Particularly illustrative are cases where colloidal NPs evolve compositionally towards a HEM phase, the production of HEM NPs through sequential incorporation of additional elements via galvanic replacement or ion exchange reactions, and the merging of heterostructured NPs into a single-phase HEM (**Figure 32**). These particle-to-particle conversion approaches offer an additional, effective synthesis strategy beyond conventional top-down and bottom-up methods for producing HEM NPs, where the mixing entropy contribution to the HEM's stability is secondary due to the low processing temperatures involved. The atomic diffusion process at the core of this conversion can occur either in one step during NP synthesis or in a two-step process and can be driven by several factors, including entropy increase of the system, reduction of surface or interface energy, decrease in solvation energy, and differences in the redox potentials of the elements. As a common starting point, these strategies use NPs as seeds or templates for growing new NPs with a HEM composition. By carefully controlling the size, shape, and composition of the initial template, these methods allow precise control over the properties of the resulting HEM NPs. This provides a pathway to engineer HEM NPs with tailored functionalities for various applications.

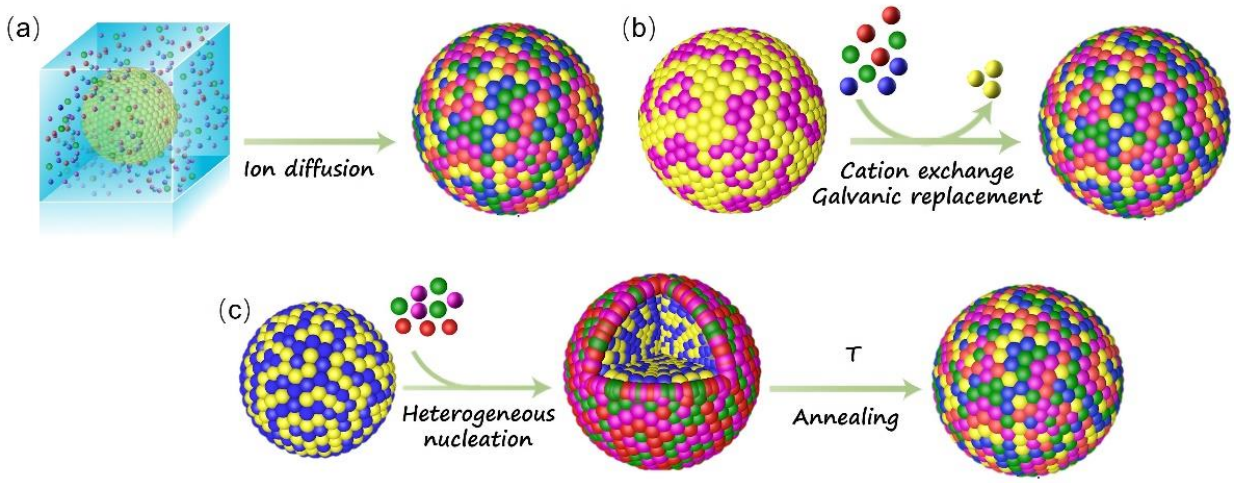

Figure 32. HEM synthesis process by thermodynamic-driven strategies. (a) Ion diffusion during NP synthesis. (b) Ion exchange and galvanic replacement of a pre-prepared NP. (c) Merging of a heterostructured NP during a post-annealing process.

3.3.1. Ion diffusion during NP synthesis

As previously observed in the synthesis of quaternary chalcogenide NPs,[120] HEM NPs often form not from HEM nuclei, but through the sequential incorporation of the different elements into seeds that are initially enriched in one particular component. This heterogeneous NP growth

mechanism does not require the precursors to have identical reduction potentials or reactivities. However, the relative reduction potentials of the elements remain crucial in the formation of metallic HEAs, as they influence the reduction rate and the order in which elements are incorporated, ultimately affecting the final composition and short-range atomic distribution within the NP. [109] Additionally, the progressive incorporation of elements may involve autocatalytic processes that facilitate the reduction of specific ions.[121] Furthermore, *in situ* ion exchange or galvanic replacement reactions during NP growth cannot be ruled out. However, very notably, the final particle composition is homogeneous or quasi-homogeneous, indicating a driving force for the formation of the HEM from an initially heterogenous elemental distribution. This driving force is unlikely related to entropy, but more likely arises from the reduction of interphase or lattice energy in a homogeneous NP composition compared to a graded or core-shell structure.

As an example, Dey et al. synthesized NiPdPtRhIr HEA NPs by slowly injecting precursors over 10 min at 275 °C, followed by a 1 h reaction time.[98] The evolution of particle composition, as shown in **Figure 33a**, revealed that the synthesis initially produced heterogeneous NPs, predominantly composed of Pd-rich Pd-Ni seeds. Subsequently, Pt was incorporated through galvanic replacement and concurrent alloying with PdNi. Rh and Ir were later integrated into the structure, likely via an auto-reduction catalytic process, ultimately resulting in the formation of homogeneous NiPdPtRhIr HEA NPs. Wang et al developed a step-alloying strategy to synthesize the HEA NPs with up to fourteen elements using an ion diffusion process that did not require high temperatures.[122] The process begins with the formation of a Pt-rich core through a liquid-phase reduction reaction using sodium borohydride as a strong reducing agent. Subsequently, an ion diffusion process introduces other metal elements that are otherwise difficult to reduce, followed by heat treatment at 973 K to form a single-phase HEA (**Figure 33 b-c)**. This approach can be extended to incorporate immiscible metals with high mixing enthalpies at relatively low temperatures, offering versatility in HEA synthesis.

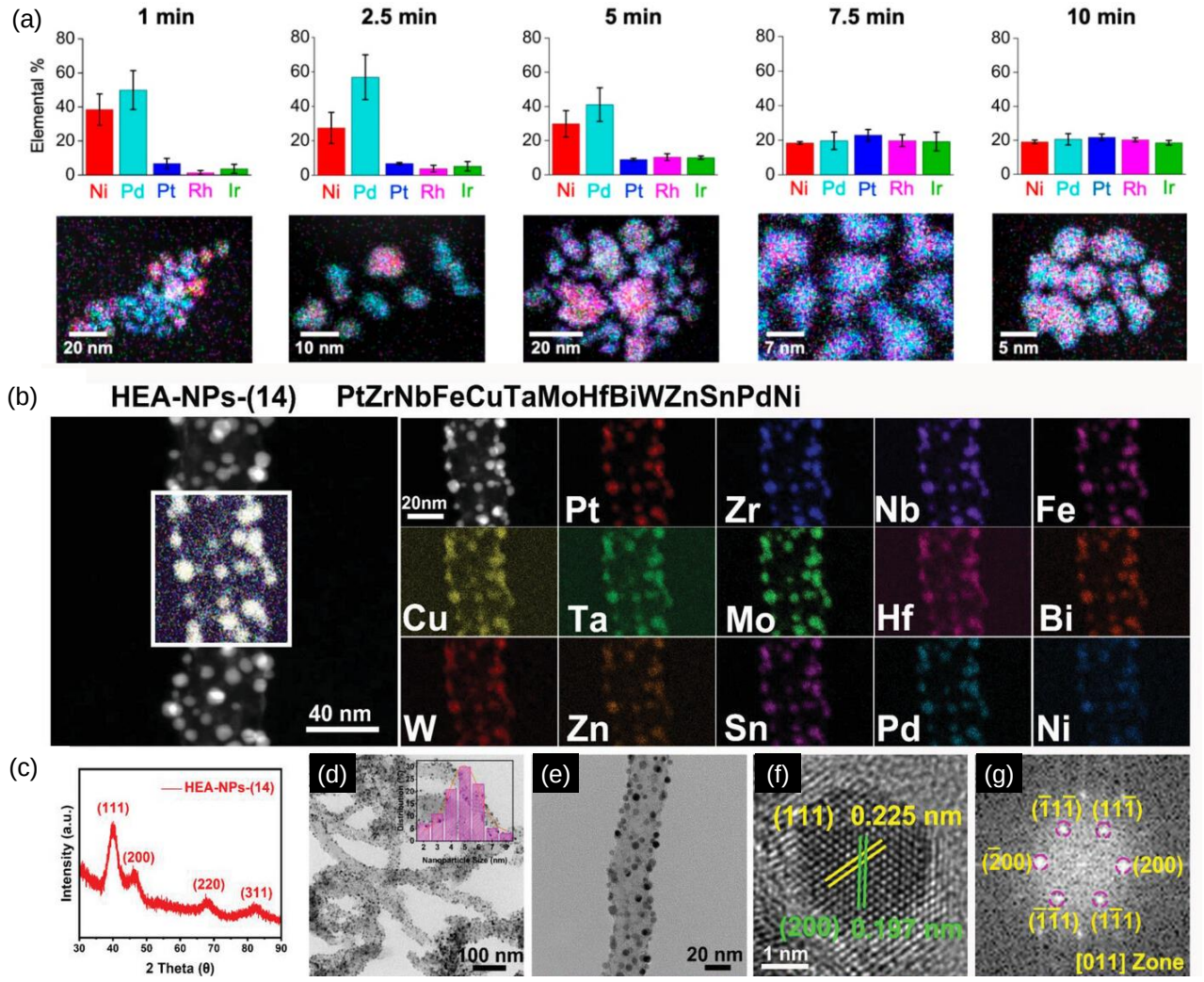

Figure 33. (a) Time-dependent formation of NiPdPtRhIr HEA NPs. Bar charts showing elemental composition (obtained from EDS measurements) and corresponding STEM-EDS element maps. Reproduced with permission.[98] Copyright 2023, American Chemical Society. (b) STEM image and EDS-mapping, (c) XRD pattern, (d, e) TEM images, (f) HRTEM image, and (g) corresponding FFT pattern of HEA NPs containing 14 elements. The inset in (d) shows the size distribution histogram. Reproduced with permission.[122] Copyright 2023, Wiley-VCH GmbH.

3.3.2. Ion exchange

Ionic HEM NPs can be synthesized through a two-step process that involves adding additional elements, typically at ambient temperature, to pre-formed binary, ternary, or quaternary template NPs. This is achieved by partially or fully exchanging one of the ions within the template NP with two or more distinct ions from the solution, without involving a redox process. During this exchange, the lattice structure remains intact. Thus this particle-to-particle conversion strategy effectively decouples the formation of an ordered crystal structure from the random introduction of cations. For HEM formation, cation exchange reactions are generally preferred due to the broader range of cation possibilities available.[123]

Ion exchange reactions can be driven by both enthalpy and entropy changes. In particular,

reactions involving the replacement of two ions from the crystal by one ion from the solution are associated with a notable increase in system entropy, which can drive the reaction.[124] It is important to note that the entropy increase occurs due to the higher number of ions in the solution, rather than in the newly formed NP. Enthalpic contributions, such as the strong solvation of the removed ions, are also commonly leveraged to drive the reaction. Additionally, enthalpy plays a crucial role in determining the final NP structure, whether a single-phase NP or a heterostructure. In some cases, cation exchange can lead to products with phase-segregated regions connected by interfaces. The formation of these interfaces during phase segregation imposes an enthalpic penalty, which grows with the number of segregated phases.

As an example, Wan et al. developed a cation exchange reaction to synthesize hollow cubic $(ZnCdFeMnCu)_xS$ NPs from $Cu_{2-x}S$ NPs.[125] As shown in **Figure 34**, they mixed metal nitrides, $Cu_{2-x}S$, and tributylphosphine (TBP) in toluene for 2 h at 50 °C. TBP effectively solvated Cu^+ ions by forming TBP-Cu^+ complexes, pulling Cu^+ out of the $Cu_{2-x}S$ framework, and allowing other cations in the solution to occupy the resulting metal vacancies within the lattice. The release of multiple Cu^+ cations for each M^{2+} or M^{3+} cation incorporated increases the overall system entropy due to the larger number of ions in the solution.

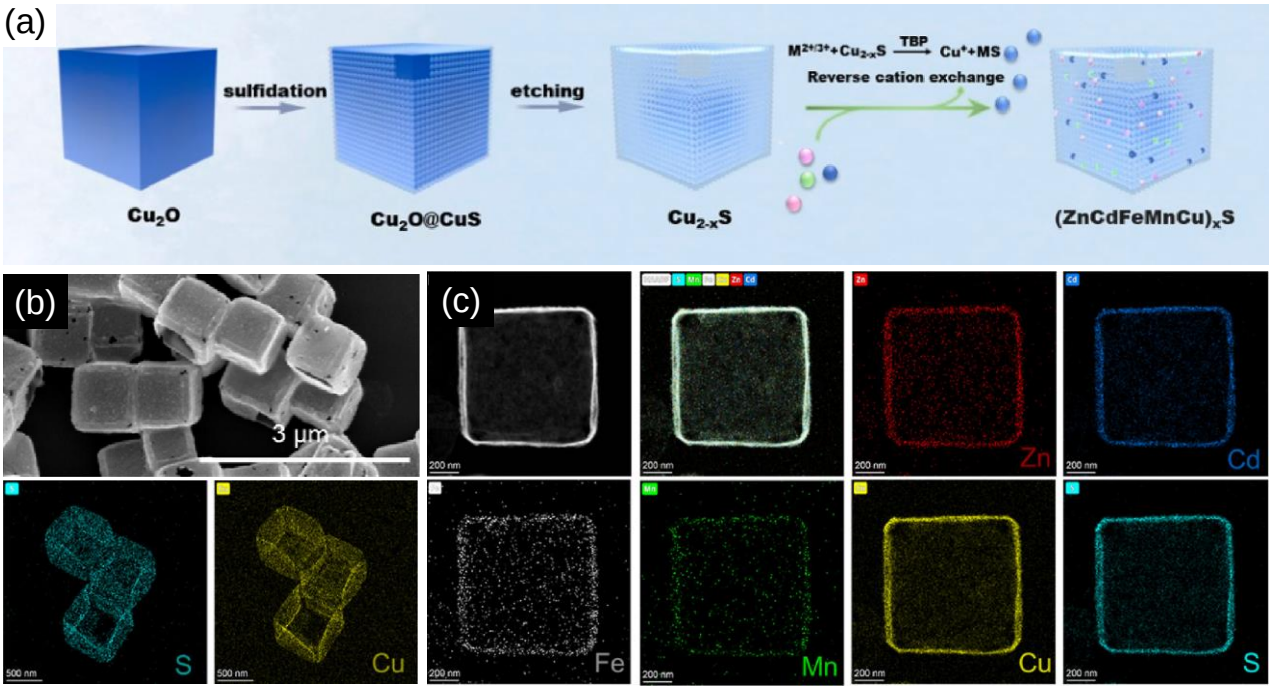

Figure 34. (a) Schematic diagram of the cation exchange process used to produce $(ZnCdFeMnCu)_xS$ NPs. (b) TEM images and (c) EDS mapping of $(ZnCdFeMnCu)_xS$. Reproduced with permission.[125] Copyright 2023, Elsevier B.V.

3.3.3. Galvanic replacement

HEM NPs can also be produced through galvanic replacement, where one metal atom within a

pre-formed template NP is replaced by multiple atoms from the solution. In this process, the reaction is primarily enthalpy-driven due to the differences in the electrochemical potentials of the involved metals, with entropy generally playing a secondary role. The galvanic replacement reaction involves the oxidation of the sacrificial metal in the template NP by a metal ion in the solution with a higher reduction potential.[126] By using solutions containing multiple metal ions with appropriate reduction potentials, the composition of the sacrificial alloy NP can be enriched. This process often results in the formation of a porous structure, which is typically associated with differential atomic diffusivities, differences in chemical reactivity among the metals and/or the shielding of certain regions during the reaction.

As an example, Tao et al. used a galvanic replacement scheme to produce PtPdIrAgRu nanoribbons, using Ag nanowires as templates.[127] As shown in **Figure 35**, different metal atoms nucleated via galvanic exchange reactions when the Ag nanowires were mixed with various metal ion precursors (such as Pt^{2+} and Pd^{2+}). Because the standard reduction potential of the Ag^{+}/Ag pair is lower than those of the Pt^{2+}/Pt and Pd^{2+}/Pd pairs, the outermost Ag atoms on the nanowires were substituted by the precursor metals via a galvanic exchange pathway, such as $Ag + Pd^{2+} \rightarrow 2Ag^{+} + Pd$. Finally, the Ag core was removed using dilute nitric acid.

The galvanic replacement mechanism has also been observed to play a role during the one-step synthesis of HEM NPs. For instance, Chen et al. reported the synthesis of PtRhBiSnSb nanoplates with a uniform element distribution from the reaction of a precursor mixture. [121] Interestingly, they observed a sequential evolution in the particle composition during the synthesis. Initially, Bi nuclei were formed, which subsequently incorporated Pt and Sn atoms. Rh and Sb were then introduced into the nanoplates via galvanic replacement.

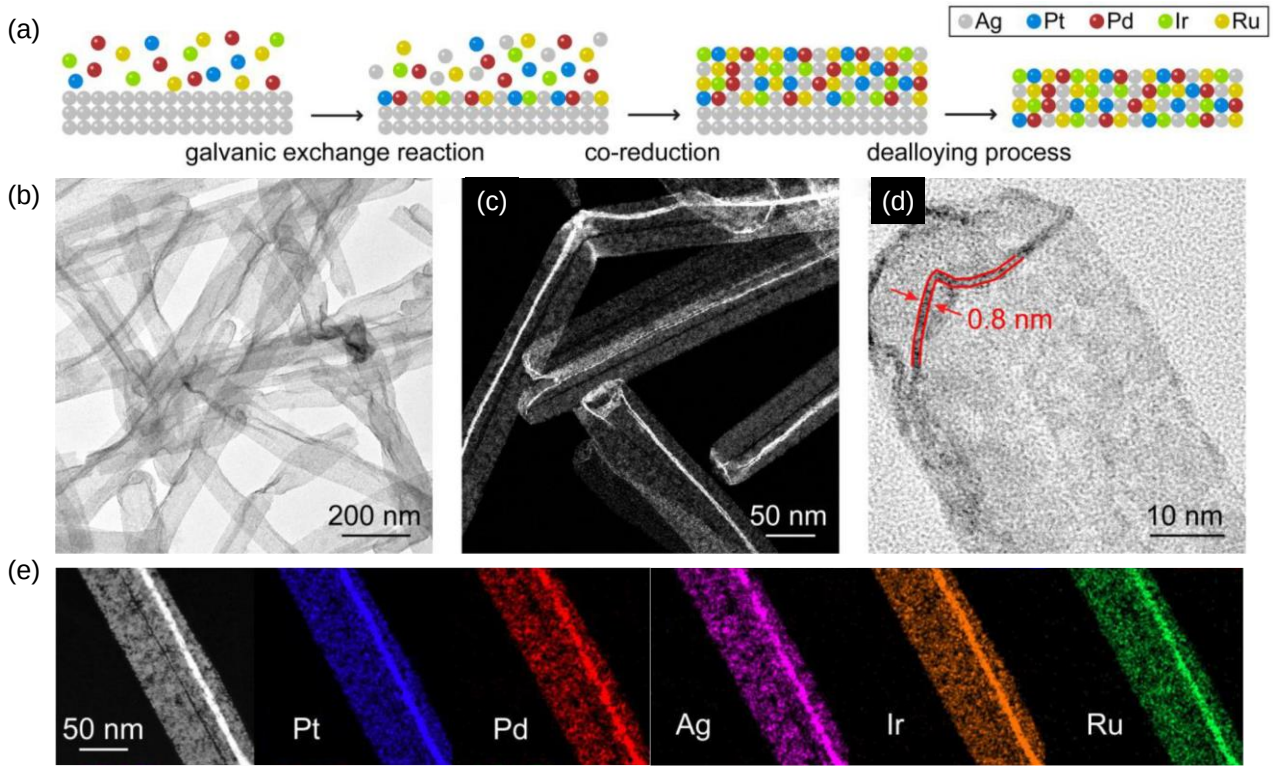

Figure 35. (a) Schematic illustration of the proposed galvanic exchange, co-reduction, and dealloying pathways used to produce the PtPdIrRuAg HEA. (b) Low-magnification TEM image and (c) HAADF-STEM image. (d) HRTEM image. (e) HAADF-STEM image and EDS element mapping images. Reproduced with permission.[127] Copyright 2022, American Chemical Society.

3.3.4. Merging of heterostructured NPs

Another case of potentially enthalpy-driven HEM NP formation is the merging of the different segregated phases within heterostructured NPs, e.g. core-shell structures, into a single-phase HEM NP at moderate temperatures. This two-step approach to producing HEM NPs was designed to overcome the challenging co-reaction/reduction of the different elements in the one-step wet-chemical methods due to differences in the reduction abilities of metal salts. This approach involves the initial synthesis of heterostructured NPs and their subsequent transformation into single-phase HEA NPs through a thermal annealing process. While the synthesis of core-shell NPs of two different elemental/binary/ternary materials may be easier than the direct synthesis of quinary/sexenary ones, the two-step process reduces energy efficiency and production throughput. Notice also, that this strategy differs from the preassembly and annealing approach described in 3.2.1 in that the preassembled particles do not have here a homogeneous element distribution.

As an example, Chen et al. prepared intermetallic 7.5 nm PdCu seeds that were used to grow of 10.4 nm PdCu@PtNiCo core-shell NPs by co-reducing the additional metal salts ($PtBr_2$, $Ni(acac)_2$, and $Co(acac)_2$) in the presence of oleylamine on the core surface.[104c] These core-shell NPs were loaded on carbon support to prevent coalescence and then annealed at 600 °C for 10 h to form the

HEA NPs (**Figure 36)**. They provided three factors contributing to synthesizing the HEA through the annealing process, (i) high interfacial strain between the multicomponent leads to a lower barrier to diffusion, facilitating them to mix together. (ii) The increased entropy of mixing is thermodynamically favorable to promote the formation of the alloy structure. (iii) The lattice distortion and low atomic diffusivity upon mixing can prevent HEAs from phase separation upon cooling. However, given the relatively low annealing temperature, entropy likely plays only a minor role. Instead, the primary driving force for merging the core and shell phases is likely the elimination of the interphase energy between them, which stabilizes the resulting homogeneous HEA structure.

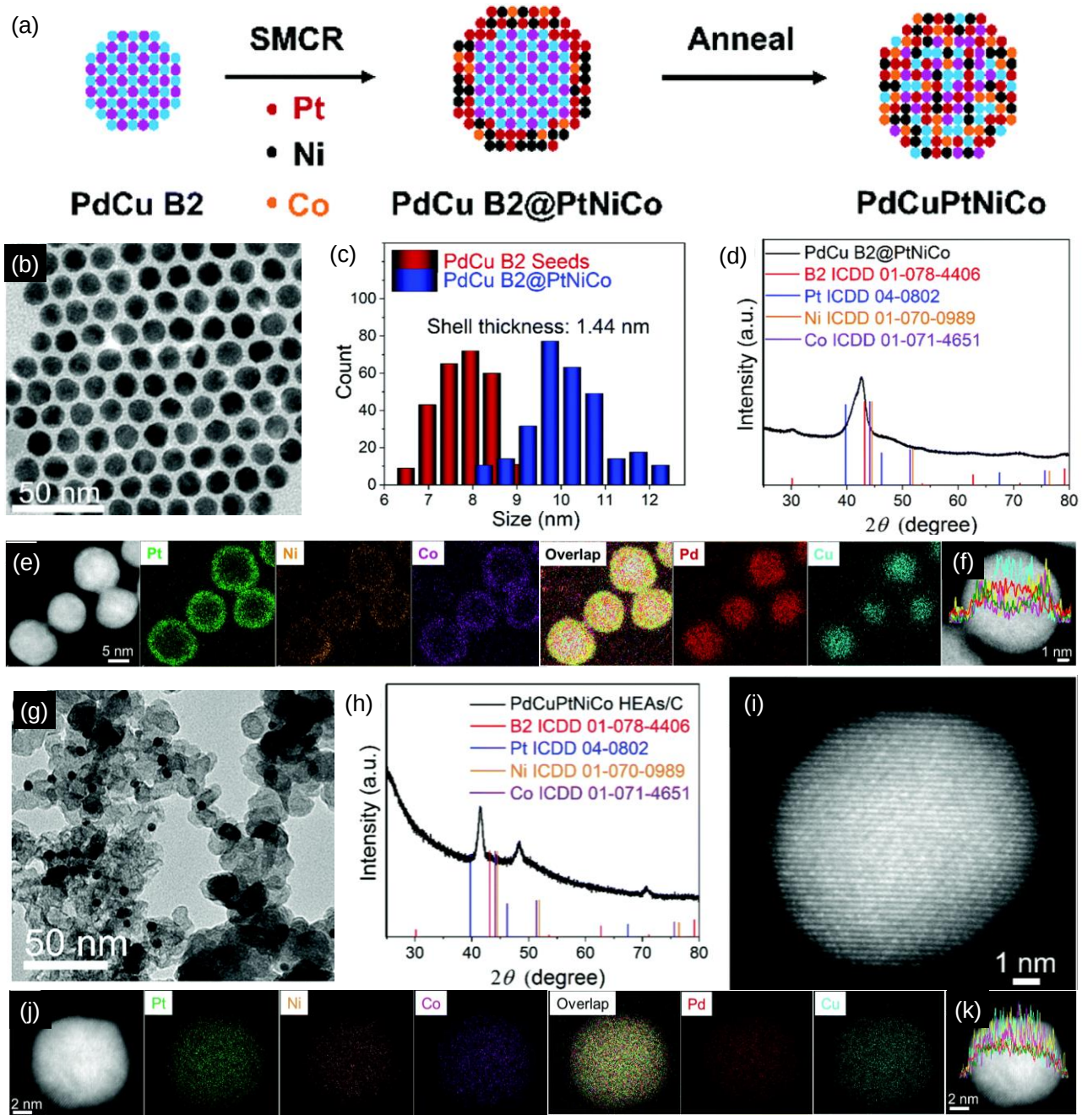

Figure 36. (a) Schematic illustration of the synthetic process for PdCuPtNiCo HEAs. Intermetallic PdCu B2 seeds are first prepared, followed by the deposition of Pt, Ni, and Co onto the PdCu B2

seeds using seed-mediated co-reduction (SMCR), resulting in core@shell PdCu B2@PtNiCo NPs. These core@shell NPs are then annealed to convert them into single-phase PdCuPtNiCo HEA NPs. (b-f) Morphological and compositional characterization of PdCu B2@PtNiCo NPs: (b) TEM image, (c) size distribution histogram, (d) XRD pattern, (e) STEM-EDS elemental mapping images and (f) line scan profile. (g-k) Morphological and compositional characterization of PdCuPtNiCo HEAs/C: (g) TEM image, (h) XRD pattern, (i) STEM-HAADF image, (j) STEM-EDS elemental mapping images, and (k) line scan profile. Reproduced with permission.[104c] Copyright 2016, Royal Society of Chemistry.

4. Conclusion

In this review, we critically discussed various top-down and bottom-up strategies for producing HEM NPs, supported by illustrative examples. For bottom-up approaches, we highlighted three primary synthesis pathways: (i) employing high processing temperatures to thermodynamically drive HEM NP formation via the entropic contribution while simultaneously controlling NP growth; (ii) promoting kinetic growth through preorganization, rapid reactions, or dilute solutions; and (iii) demonstrating enthalpy-driven growth, illustrated by examples of particle compositional evolution. This review addresses current research gaps by providing a structured analysis of the underlying mechanisms driving HEM NP formation in various synthesis approaches, which are often ambiguously reported. By categorizing these pathways based on thermodynamic, kinetic, and enthalpic drivers, the review offers a clearer understanding of HEM formation mechanisms and how they can be tuned to optimize functional properties through the adjustment of specific synthesis parameters. This comprehensive framework not only facilitates more targeted experimental design but also lays the groundwork for developing more efficient and scalable synthesis methods. Future studies can build on this foundation to refine these approaches, optimize HEM NP properties, and explore new compositional possibilities, ultimately enhancing the versatility and applicability of HEM NPs in different fields of application.

5. Prospects

Despite the growing interest in these materials and the significant progress made in recent years, the synthesis of HEM NPs is still in its infancy, and numerous challenges persist. These challenges include controlling NP morphology, size, bulk and surface overall composition and atomic distribution, phase, and defects. Notably, tuning surface chemistry, which is critical for many applications, has rarely been explored in depth in these materials. To address these challenges, a deeper understanding of HEM NP nucleation and growth mechanisms is required. Additionally, advancements in characterizing the NP parameters, particularly atomic distribution, their formation processes, and their evolution during operation are essential. Moreover, there are several additional open research directions in the field of HEM NPs, including establishing structure-property relationships, optimizing performance across a range of applications, integrating these materials into

devices, ensuring their stability under operational conditions, and designing HEMs tailored for specific functional properties. We choose 5 key areas for additional discussion that are critical for advancing the understanding and control of these complex materials, unlocking their full potential for advanced technological applications (**Figure 37**).

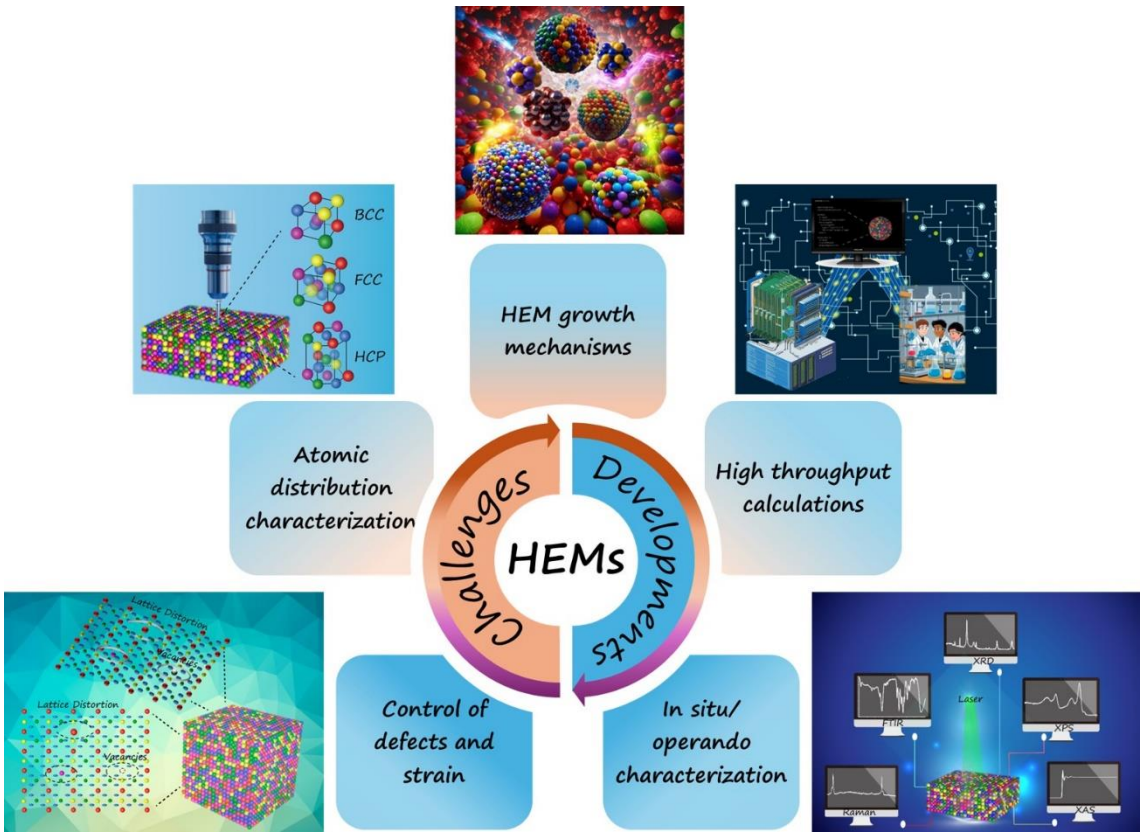

Figure 37. Schematic illustration of key areas for advancing the field of HEMs.

Characterization of composition at the atomic scale, enabling adjustment. One of the primary challenges in controlling the overall composition and elemental distribution within HEM NPs, particularly at the surface, is obtaining accurate feedback through precise atomic-scale characterization. This is crucial for fine-tuning and optimizing these materials. It is important to note that the element arrangement within a HEM NP is unlikely to be entirely random. Both experimental observations and theoretical predictions have revealed that certain elements in HEMs tend to exhibit preferential bonding, leading to short-range order. [9b, 9e, 119] This short-range order may play a critical role in defining the functional properties of the material. However, accurately characterizing this order in HEM NPs is extremely challenging, complicating the establishment of reliable structure-composition-property relationships. Conventional techniques like HAADF-STEM-EDS, commonly used to assess the homogeneity of element distribution in HEM NPs,[9e, 128] may not be sufficiently sensitive to detect preferential short-range ordering. Alternative experimental approaches and advanced data processing methods like non-negative matrix factorization, as demonstrated by

Pittkowski et al.[9b], need to be further developed to gain more precise insights into the atomic distribution within HEM NPs.

Particularly, the surface composition of HEM NPs can differ significantly from the bulk due to varying chemical environments, which could profoundly impact performance in applications involving interaction with the media. [9e, 129] For instance, HEM NPs have garnered significant interest in catalysis due to their wide range of surface sites, offering a nearly continuous distribution of adsorption energies.[32i, 128, 130] As an example, in a HEA formed by just five elements with an FCC crystal structure, considering only the 12 nearest neighbors, over 390,000 distinct chemical environments are possible for each surface site. This translates to nearly 2 million potential surface sites in a five-element compound and 1 billion in a ten-element HEM NP, assuming no short-range order or preferential surface configurations. This quasi-continuous distribution of binding energies can substantially reduce overpotentials in electrocatalytic processes and enable the catalysis of complex, multistep tandem reactions. As a potential drawback, this diversity of surface sites could also pose challenges, such as reducing reaction selectivity. However, some studies have reported improved selectivity using HEM catalysts.[131] A key target in this field is identifying the most effective atomic configurations and finding ways to maximize their presence to enhance performance. Achieving this goal requires not only determining the exact composition and atomic arrangement but also understanding how these features evolve under operational conditions—a challenge that remains far from fully addressed.

NP stability and in situ characterization. The atomic arrangement at the surface, and potentially the overall composition of HEM NPs, is often sensitive to changes in the NP environment and operational conditions. In this context, oxidation and reduction processes in HEM NPs have been shown to induce element rearrangement, [132] following patterns similar to those observed in binary and ternary alloys, primarily driven by the relative oxophilicity of different elements.[133] Despite these dynamic rearrangements, improved stabilities against oxidation, corrosion, leaching, and performance degradation have been frequently reported for HEM NPs, especially in the field of (electro)catalysis. These enhanced stabilities have been attributed to an increased energy barrier for atomic diffusion in the multi-element matrix.[130b, 134] However, this reasoning appears to contradict the formation of HEM NPs through processes like cation exchange, galvanic replacement, and the sequential addition of elements into elemental nuclei, which rely on such diffusion mechanisms. Resistance to corrosion and leaching in HEMs has also been linked to the inclusion of elements like Cr, Al, or Si, which enhance oxidation resistance by forming protective oxide layers, or noble metals that inhibit leaching. [135] This protection can be activated by the initial preferential leaching of certain

elements, thereby increasing the surface concentration of protective noble metals, [136] or by the surface segregation of oxidation-resistant elements like Cr or Al upon exposure to air driven by their higher oxophilicity for instance. A reliable assessment of the stability of HEM NPs and the effects of different media on their surface properties is crucial. This requires precise post-operational characterization and in situ/operando techniques to monitor the materials under actual operating conditions. Furthermore, developing more sophisticated theoretical models and computational simulations to predict the behavior and properties of HEMs under various environmental conditions is vital for advancing this field. These combined efforts will provide deeper insights into the mechanisms governing stability and help optimize HEM NPs for real-world applications.

Control of defects and strain. The engineering of defects and dopants within HEM NPs has largely been overlooked. As extensively studied in bulk HEMs, the near-equiatomic ratios of multiple elements with differing atomic sizes and electronegativities result in substantial lattice distortions and high defect densities. These features contribute to the chemical stability, enhanced mechanical properties, and low thermal conductivity of HEMs, making them promising candidates for a variety of applications, including thermoelectric energy conversion for instance.[137] However, this high defect density and atomic disorder may negatively affect the optical and optoelectronic properties of HEM NPs, potentially degrading performance in areas like photoluminescence and solar energy conversion, similar to what has been observed in quaternary chalcogenide NPs. [138] Additionally, defects and lattice distortions in HEMs are frequently linked to reduced ionic diffusivity. Although there is ongoing debate, normalized activation energies for diffusion in CrMnFeCoNi HEMs do appear to be higher than in conventional alloys, [139] and significantly slower atomic diffusion rates have been calculated for CoNiCuRuPd HEM NPs, for example. [140] Understanding and controlling defects in HEM NPs is critical, as these imperfections can be both beneficial and detrimental depending on the application. Precise characterization of the types, densities, and distributions of defects is crucial for establishing how they influence properties and performance. Moreover, developing strategies to deliberately engineer or mitigate defects to optimize desired functionalities remains an important area of interest. This includes tailoring the defect types and localizations to either enhance specific properties, or minimize adverse effects on electronic, optical, and ionic transport behaviors.

HEM growth mechanisms for reliable synthesis. Understanding the precise nucleation and growth mechanisms of HEM NPs is both a formidable challenge and a critical step toward achieving reliable control over their parameters. The formation of these complex materials involves intricate interactions between thermodynamic and kinetic factors, making it difficult to pinpoint the exact

processes that govern their synthesis. Whether driven by entropy, enthalpy, or kinetic factors, the dominant mechanism depends heavily on the specific synthesis conditions. Accurately identifying which mechanism prevails to be able to control it requires precise calculations of the associated energies and entropies, alongside advanced computational models that can simulate the dynamic processes occurring during synthesis. This improved mechanistic understanding is key to producing HEM NPs with consistently controlled properties in a more reliable, sustainable, efficient, and cost-effective manner. In this direction, a significant challenge remains in developing scalable, high-yield industrial manufacturing methods that can maintain uniformity and compositional control across large batches. Addressing this challenge involves refining top-down and bottom-up synthesis techniques, ensuring that the resulting HEM NPs exhibit the desired structural, chemical, and functional characteristics. Moreover, it is crucial to consider the environmental impact and economic viability of HEM production and utilization from the outset. This involves not only optimizing energy efficiency in synthesis processes but also selecting abundant, non-toxic, and cost-effective precursors. Enhancing sustainability further requires promoting recycling and reuse throughout the lifecycle of HEM-based products. However, a significant challenge lies in the inherent complexity of recycling HEMs. The intimate integration of multiple metals in a single-phase structure complicates the separation, recovery, and purification of individual elements, posing substantial obstacles to effective recycling. Addressing these issues will require innovative strategies and technologies to ensure that the benefits of HEMs are realized without compromising sustainability.

High throughput calculations to determine stable phases, properties, and performance. Despite the debated role of entropy in stabilizing HEM NPs and determining their properties, the true appeal of HEMs lies in the vast array of compounds that can be created by combining five or more distinct elements. With 40 elements deemed useful, there are over 650,000 potential combinations of five elements and more than 1.2 billion combinations when considering between five to ten elements. When the various possible ratios of each element within these combinations are also considered, the number of potential materials becomes virtually limitless.[141] This immense diversity provides unprecedented opportunities for designing and engineering HEM NPs, potentially using abundant and non-toxic elements, to meet the demands of a broad spectrum of existing and emerging applications. However, the investigation into the vast array of potential new alloys represents both the primary interest and the principal challenge of research in HEMs. Probing the extensive spectrum of possible compositions necessitates the use of high-throughput computational techniques to forecast stable HEM compositions, structures, and their associated properties, and performances.[136, 142] This is complemented by extensive experimental synthesis, alongside a thorough screening of properties and performance, [143] and the development of reliable correlations between composition,

structure, and properties. In this direction, HEMs are an ideal platform for showcasing and developing cutting-edge material screening strategies. These include ab initio molecular dynamics combined with density functional theory, [134] combinatorial[144] and automated[145] high-throughput synthesis combined with three-dimensional atomic-scale characterization, and machine-learning tools for guided HEM design and performance optimization.[146] These developments not only aid in understanding HEM formation, stability, and properties but also advance the broader field of material science.

Overall, HEM NPs are a new class of materials that present exciting opportunities, but also significant challenges. As this field is still in its early stages, HEM NPs are just beginning to become accessible, and there remains a substantial amount to learn about their formation mechanisms, the precise control of their atomic distribution, and their chemical coordination, particularly at the surface where many of their functional properties are determined. Understanding how these factors influence the performance of HEM NPs in different applications, whether in catalysis, energy storage, or electronics, is critical for unlocking their full potential. As research progresses, it will be essential to establish clear structure-property relationships and to explore the effects of high configurational entropy and element diversity on the stability, reactivity, and overall functionality of HEM NPs. Additionally, scaling up production for real-world applications while maintaining performance consistency remains a key hurdle. Finally, integrating HEM NPs into existing technologies and evaluating their long-term stability under operational conditions are vital steps toward practical deployment. As more is understood about these novel materials, the possibility of designing tailored HEM NPs with enhanced performance, utilizing abundant and non-toxic elements, and creating multifunctional materials will continue to expand, offering exciting possibilities for next-generation solutions across multiple industries.

6. References

[1] J. W. Yeh, S. K. Chen, S. J. Lin, J. Y. Gan, T. S. Chin, T. T. Shun, C. H. Tsau, S. Y. Chang, *Adv. Eng. Mater.* **2004**, 6, 299.

[2] a) J. Ding, D. Wu, J. Zhu, S. Huang, F. Rodríguez-Hernández, Y. Chen, C. Lu, S. Zhou, J. Zhang, D. Tranca, X. Zhuang, *Chem. Eng. J* **2021**, 426, 131320; b) Y. Huang, J.-W. Yeh, A. C. M. Yang, *Materialia* **2021**, 15, 100978; c) X. Lei, Q. Tang, Y. Zheng, P. Kidkhunthod, X. Zhou, B. Ji, Y. J. N. S. Tang, *Nat. Sustain.* **2023**, 6, 816.

[3] a) S. S. Aamlid, M. Oudah, J. Rottler, A. M. Hallas, *J. Am. Chem. Soc.* **2023**, 145, 5991; b) A. Sarkar, Q. Wang, A. Schiele, M. R. Chellali, S. S. Bhattacharya, D. Wang, T. Brezesinski, H. Hahn, L. Velasco, B. Breitung, *Adv. Mater.* **2019**, 31, 1806236; c) L. Su, J. Ren, T. Lu, K. Chen, J. Ouyang, Y. Zhang, X. Zhu, L. Wang, H. Min, W. Luo, Z. Sun, Q. Zhang, Y. Wu, L. Sun, L. Mai, F. Xu, *Adv. Mater.* **2023**, 35, 2205751; d) A. Abdelhafiz, B. Wang, A. R. Harutyunyan, J. Li, *Adv. Energy Mater.* **2022**, 12, 2200742; e) J. L. Rowell, M. Kang, D. Yoon,

K. Z. Jiang, Y. Jia, H. D. Abruna, D. A. Muller, R. D. Robinson, *J. Am. Chem. Soc.* **2024**, 146, 17613.

[4] a) P.-W. Chien, C.-B. Chang, H.-Y. Tuan, *Energy Storage Mater.* **2023**, 61, 102853; b) R. He, S. Wang, L. Yang, S. Horta, Y. Ding, C. Di, X. Zhang, Y. Xu, M. Ibáñez, Y. Zhou, S. Mebs, H. Dau, J. N. Hausmann, W. Huo, P. W. Menezes, A. Cabot, *Energy Environ. Sci.* **2024**, 17, 7193.

[5] a) M. Cui, C. Yang, B. Li, Q. Dong, M. Wu, S. Hwang, H. Xie, X. Wang, G. Wang, L. Hu, *Adv. Energy Mater.* **2020**, 11, 2002887; b) M. J. Theibault, C. R. McCormick, S. Lang, R. E. Schaak, H. D. Abruna, *ACS Nano* **2023**, 17, 18402.

[6] a) Y. Li, Y. Y. Tay, P. J. S. Buenconsejo, W. Manalastas, W. H. Tu, H. K. Lim, T. Salim, M. O. Thompson, S. Madhavi, C. Y. Tay, K. W. Tan, *Adv. Funct. Mater.* **2023**, 33, 2211279; b) P. Wu, C. Deng, P. Liu, F. Liu, L. Chen, B. Wang, W. Zhu, C. Xu, *Chem. Eng. J.* **2023**, 474, 145850.

[7] a) S. Dong, H. Zhou, X. Hu, J. Zhang, Y. Li, W. Shang, Z. Liu, L. Wan, H. Zhao, *Int. J. Hydrogen Energy* **2023**, 48, 18233; b) X. Wang, Y. Zuo, S. Horta, R. He, L. Yang, A. Ostovari Moghaddam, M. Ibanez, X. Qi, A. Cabot, *ACS Appl. Mater. Interfaces* **2022**, 14, 48212.

[8] a) Y. Zhang, *High entropy materials*, Springer, **2023**; b) C. Oses, C. Toher, S. J. N. R. M. Curtarolo, *Nat. Rev. Mater.* **2020**, 5, 295; c) Y. Ma, Y. Ma, Q. Wang, S. Schweidler, M. Botros, T. Fu, H. Hahn, T. Brezesinski, B. Breitung, *Energ. Environ. Sci.* **2021**, 14, 2883; d) M. C. Gao, D. B. Miracle, D. Maurice, X. Yan, Y. Zhang, J. A. Hawk, *J. Mater. Res.* **2018**, 33, 3138.

[9] a) B. Wang, C. Wang, X. Yu, Y. Cao, L. Gao, C. Wu, Y. Yao, Z. Lin, Z. Zou, *Nat. Synth.* **2022**, 1, 138; b) R. K. Pittkowski, C. M. Clausen, Q. Chen, D. Stoian, W. van Beek, J. Bucher, R. L. Welten, N. Schlegel, J. K. Mathiesen, T. M. Nielsen, J. Du, A. W. Rosenkranz, E. D. Bøjesen, J. Rossmeisl, K. M. Ø. Jensen, M. Arenz, *EES Catal.* **2023**, 1, 950; c) A. Barbero, C. Moreira Da Silva, N. Ortiz Pena, N. Kefane, A. Jaafar, M. Thorey, H. Bouaia, J. Nelayah, G. Wang, H. Amara, C. Ricolleau, V. Huc, D. Alloyeau, *Faraday Discuss.* **2023**, 242, 129; d) S. S. Soliman, G. R. Dey, C. R. McCormick, R. E. Schaak, *ACS Nano* **2023**, 17, 16147; e) S. L. A. Bueno, A. Leonardi, N. Kar, K. Chatterjee, X. Zhan, C. Chen, Z. Wang, M. Engel, V. Fung, S. E. Skrabalak, *ACS Nano* **2022**, 16, 18873; f) A. V. Saghir, S. M. Beidokhti, J. V. Khaki, A. Salimi, *J. Eur. Ceram. Soc.* **2021**, 41, 563.

[10] a) B. Han, J. Wei, F. He, D. Chen, Z. J. Wang, A. Hu, W. Zhou, J. J. Kai, *Entropy* **2018**, 20, 910; b) B. Han, J. Wei, Y. Tong, D. Chen, Y. Zhao, J. Wang, F. He, T. Yang, C. Zhao, Y. Shimizu, K. Inoue, Y. Nagai, A. Hu, C. T. Liu, J. J. Kai, *Scripta Mater.* **2018**, 148, 42; c) Z. Zeng, J. Zhao, X. Zhou, J. Li, B. Liang, *Chem. Phys.* **2019**, 517, 126; d) S.-P. Ju, I. J. Lee, H.-Y. Chen, *J. Alloys Compd.* **2021**, 858, 157681; e) M.-H. Tsai, J.-W. Yeh, *Mater. Res. Lett.* **2014**, 2, 107; f) J.-W. Yeh, *Ann. Chim. Sci. Mat.* **2006**, 31, 633.

[11] a) S. Guo, C. Ng, J. Lu, C. T. Liu, *J. Appl. Phys.* **2011**, 109, 103505; b) S. Guo, *Mater. Sci. Technol.* **2015**, 31, 1223; c) X. Chang, M. Zeng, K. Liu, L. Fu, *Adv. Mater.* **2020**, 32, 1907226.

[12] a) C. Lee, Y. Chou, G. Kim, M. C. Gao, K. An, J. Brechtl, C. Zhang, W. Chen, J. D. Poplawsky, G. Song, Y. Ren, Y. C. Chou, P. K. Liaw, *Adv. Mater.* **2020**, 32, 2004029; b) R. K. Nutor, Q. Cao, X. Wang, D. Zhang, Y. Fang, Y. Zhang, J.-Z. Jiang, *Adv. Eng. Mater.* **2020**, 22, 2000466.

[13] a) H. Wang, Q. He, X. Gao, Y. Shang, W. Zhu, W. Zhao, Z. Chen, H. Gong, Y. Yang, *Adv. Mater.* **2023**, 36, 2305453; b) Q. Chen, X. Han, Z. Xu, Q. Chen, Q. Wu, T. Zheng, P. Wang, Z. Wang, J. Wang, H. Li, Z. Xia, J. Hao, *Nano Energy* **2023**, 110, 108380; c) B. Wang, Y. Yao, X. Yu, C. Wang, C. Wu, Z. Zou, *J. Mater. Chem. A* **2021**, 9, 19410; d) J. Ren, Y. Zhang, D. Zhao, Y. Chen, S. Guan, Y. Liu, L. Liu, S. Peng, F. Kong, J. D. Poplawsky, G. Gao, T. Voisin,

K. An, Y. M. Wang, K. Y. Xie, T. Zhu, W. Chen, *Nature* **2022**, 608, 62; e) Z. Li, S. Zhao, R. O. Ritchie, M. A. Meyers, *Prog. Mater Sci.* **2019**, 102, 296; f) J. Wang, H. Guo, Z. Jiao, D. Zhao, X. Chen, S. Ma, T. Zhang, X. Liu, G. Sha, J. Qiao, J. Brechtl, P. K. Liaw, Z. Wang, *Acta Mater.* **2024**, 276, 120147.

[14] a) Z. Ma, T. Xu, W. Li, Y. Cheng, J. Li, D. Zhang, Q. Jiang, Y. Luo, J. Yang, *Adv. Funct. Mater.* **2021**, 31, 2103197; b) Y. Luo, S. Hao, S. Cai, T. J. Slade, Z. Z. Luo, V. P. Dravid, C. Wolverton, Q. Yan, M. G. Kanatzidis, *J. Am. Chem. Soc.* **2020**, 142, 15187.

[15] a) L. Zendejas Medina, L. Mølmen, E. M. Paschalidou, O. Donzel-Gargand, P. Leisner, U. Jansson, L. Nyholm, *Adv. Funct. Mater.* **2023**, 33, 2307897; b) Z. Chen, Z. Tian, L. Zheng, K. Ming, X. Ren, J. Wang, B. Li, *J. Adv. Ceram.* **2022**, 11, 1279; c) B. Kombaiah, Y. Zhou, K. Jin, A. Manzoor, J. D. Poplawsky, J. A. Aguiar, H. Bei, D. S. Aidhy, P. D. Edmondson, Y. Zhang, *ACS Appl. Mater. Interfaces* **2023**, 15, 3912; b) Y. Yang, Y. Dong, S. Liu, S. Duan, C. Li, P. Zhang, *J. Alloys Compd.* **2024**, 998, 175006.

[16] a) A. R. Mazza, E. Skoropata, Y. Sharma, J. Lapano, T. W. Heitmann, B. L. Musico, V. Keppens, Z. Gai, J. W. Freeland, T. R. Charlton, M. Brahlek, A. Moreo, E. Dagotto, T. Z. Ward, *Adv. Sci.* **2022**, 9, 2270062; b) Z. Rao, B. Dutta, F. Körmann, W. Lu, X. Zhou, C. Liu, A. K. da Silva, U. Wiedwald, M. Spasova, M. Farle, D. Ponge, B. Gault, J. Neugebauer, D. Raabe, Z. Li, *Adv. Funct. Mater.* **2020**, 31, 2007668; c) V. Chaudhary, R. Chaudhary, R. Banerjee, R. V. Ramanujan, *Mater. Today* **2021**, 49, 231.

[17] a) J. Kwon, S. Sun, S. Choi, K. Lee, S. Jo, K. Park, Y. K. Kim, H. B. Park, H. Y. Park, J. H. Jang, H. Han, U. Paik, T. Song, *Adv. Mater.* **2023**, 35, 2300091; b) T. X. Nguyen, Y. H. Su, C. C. Lin, J. Ruan, J. M. Ting, *Adv. Sci.* **2021**, 8, 2002446.

[18] a) R. He, L. Yang, Y. Zhang, X. Wang, S. Lee, T. Zhang, L. Li, Z. Liang, J. Chen, J. Li, A. Ostovari Moghaddam, J. Llorca, M. Ibáñez, J. Arbiol, Y. Xu, A. Cabot, *Energy Storage Mater.* **2023**, 58, 287; b) R. He, L. Yang, Y. Zhang, D. Jiang, S. Lee, S. Horta, Z. Liang, X. Lu, A. O. Moghaddam, J. Li, M. Ibanez, Y. Xu, Y. Zhou, A. Cabot, *Adv. Mater.* **2023**, e2303719.

[19] N. Kumar Katiyar, K. Biswas, J.-W. Yeh, S. Sharma, C. Sekhar Tiwary, *Nano Energy* **2021**, 88, 106261.

[20] a) S. Jo, M. C. Kim, K. B. Lee, H. Choi, L. Zhang, J. I. Sohn, *Adv. Energy Mater.* **2023**, 13, 2301420; b) C. Hu, K. Yue, J. Han, X Liu, L. Liu, Q. Liu, Q. Kong, C-W. Pao, Z. Hu, K. Suenaga, D. Su, Q. Zhang, X. Wang, Y. Tan, X. Huang, *Sci. Adv.* **2023**, 9, eadf9144.

[21] a) H. Huang, J. Zhao, H. Guo, B. Weng, H. Zhang, R. A. Saha, M. Zhang, F. Lai, Y. Zhou, R. Z. Juan, P. C. Chen, S. Wang, J. A. Steele, F. Zhong, T. Liu, J. Hofkens, Y. M. Zheng, J. Long, M. B. J. Roeffaers, *Adv. Mater.* **2024**, 36, 2313209; b) S. Qi, K. Zhu, T. Xu, H. Zhang, X. Guo, J. Wang, F. Zhang, X. Zong, *Adv. Mater.* **2024**, 36, 2403328.

[22] a) Q. Wang, A. Sarkar, D. Wang, L. Velasco, R. Azmi, S. S. Bhattacharya, T. Bergfeldt, A. Düvel, P. Heitjans, T. Brezesinski, H. Hahn, B. Breitung, *Energ. Environ. Sci.* **2019**, 12, 2433; b) Y. Ma, Y. Ma, S. L. Dreyer, Q. Wang, K. Wang, D. Goonetilleke, A. Omar, D. Mikhailova, H. Hahn, B. Breitung, T. Brezesinski, *Adv. Mater.* **2021**, 33, 2101342.

[23] Y. Wang, Y. Wang, *Nano Energy* **2022**, 104, 107958.

[24] A. D. Mendaza, A. Melianas, S. Rossbauer, O. Backe, L. Nordstierna, P. Erhart, E. Olsson, T. D. Anthopoulos, O. Inganas, C. Muller, *Adv. Mater.* **2015**, 27, 7325.

[25] M. Ahn, Y. Park, S. H. Lee, S. Chae, J. Lee, J. T. Heron, E. Kioupakis, W. D. Lu, J. D. Phillips, *Adv. Electron. Mater.* **2021**, 7, 2001258.

[26] D. Castro, P. Jaeger, A. C. Baptista, J. P. Oliveira, *Metals* **2021**, 11, 648.

[27] B. Jiang, Y. Yu, J. Cui, X. Liu, L. Xie, J. Liao, Q. Zhang, Y. Huang, S. Ning, B. Jia, B. Zhu, S. Bai, L. Chen, S. J. Pennycook, J. He, *Science* **2021**, 371, 830–834.
[28] S. Dixit, S. Rodriguez, M. R. Jones, P. Buzby, R. Dixit, N. Argibay, F. W. DelRio, H. H. Lim, D. Fleming, *J. Therm. Spray Technol.* **2022**, 31, 1021.
[29] J. Li, Y. Huang, X. Meng, Y. Xie, *Adv. Eng. Mater.* **2019**, 21, 1900343.
[30] A. Kareer, J. C. Waite, B. Li, A. Couet, D. E. J. Armstrong, A. J. Wilkinson, *J. Nucl. Mater.* **2019**, 526, 151744.
[31] a) Y.-B. Lu, G.-X. Zhang, F.-Y. Yang, M.-Q. Yao, L.-Y. Liu, H. Pang, *Rare. Metals.* **2023**, 42, 3212; b) G. R. Dey, S. S. Soliman, C. R. McCormick, C. H. Wood, R. R. Katzbaer, R. E. Schaak, *ACS Nanosci. Au* **2024**, 4, 3; c) W. Al Zoubi, R. A. K. Putri, M. R. Abukhadra, Y. G. Ko, *Nano Energy* **2023**, 110, 108362; d) Y. Yao, Q. Dong, A. Brozena, J. Luo, J. Miao, M. Chi, C. Wang, I. G. Kevrekidis, Z. J. Ren, J. Greeley, G. Wang, A. Anapolsky, L. Hu, *Science* **2022**, 376, eabn3103; e) G. J. N. R. M. Pacchioni, *Nat. Rev. Mater.* **2022**, 7, 156.
[32] a) C. Oses, C. Toher, S. Curtarolo, *Nat. Rev. Mater.* **2020**, 5, 295; b) H. Zheng, G. Luo, A. Zhang, X. Lu, L. He, *ChemCatChem* **2020**, 13, 806; c) D. Modupeola, P. Popoola, *Frontiers in Energy Research* **2023**, 11; d) G. M. Tomboc, T. Kwon, J. Joo, K. Lee, *J. Mater. Chem. A* **2020**, 8, 14844; e) Y.-C. Qin, F.-Q. Wang, X.-M. Wang, M.-W. Wang, W.-L. Zhang, W.-K. An, X.-P. Wang, Y.-L. Ren, X. Zheng, D.-C. Lv, A. Ahmad, *Rare. Metals* **2021**, 40, 2354; f) S. Ashraf, Y. Liu, H. Wei, R. Shen, H. Zhang, X. Wu, S. Mehdi, T. Liu, B. Li, *Small* **2023**, 19 202303031; g) X. Tong, J. Zheng, S. Xue, S. Guo, *ACS Sustain. Chem. Eng.* **2023**, 11, 10203; h) E. P. George, D. Raabe, R. O. Ritchie, *Nat. Rev. Mater.* **2019**, 4, 515; i) T. A. A. Batchelor, J. K. Pedersen, S. H. Winther, I. E. Castelli, K. W. Jacobsen, J. Rossmeisl, *Joule* **2019**, 3, 834.
[33] K. M. B. Urs, N. K. Katiyar, R. Kumar, K. Biswas, A. K. Singh, C. S. Tiwary, V. Kamble, *Nanoscale* **2020**, 12, 11830.
[34] N. K. Katiyar, S. Nellaiappan, R. Kumar, K. D. Malviya, K. G. Pradeep, A. K. Singh, S. Sharma, C. S. Tiwary, K. Biswas, *Mater. Today Energy* **2020**, 16, 100393.
[35] N. Kumar, C. S. Tiwary, K. Biswas, *J. Mater. Sci.* **2018**, 53, 13411.
[36] C. Xing, Z. Li, Z. Wang, S. Zhang, Z. Xie, X. Zhu, Z. Peng, *Nano-micro Lett.* **2023**, 16, 47.
[37] T. Ying, T. Yu, Y. S. Shiah, C. Li, J. Li, Y. Qi, H. Hosono, *J. Am. Chem. Soc.* **2021**, 143, 7042.
[38] J. Qu, A. Elgendy, R. Cai, M. A. Buckingham, A. A. Papaderakis, H. de Latour, K. Hazeldine, G. F. S. Whitehead, F. Alam, C. T. Smith, D. J. Binks, A. Walton, J. M. Skelton, R. A. W. Dryfe, S. J. Haigh, D. J. Lewis, *Adv. Sci.* **2023**, 10, e2204488.
[39] L. Yang, R. He, X. Wang, T. Yang, T. Zhang, Y. Zuo, X. Lu, Z. Liang, J. Li, J. Arbiol, P. R. Martínez-Alanis, X. Qi, A. Cabot, *Nano Energy* **2023**, 115, 108714.
[40] a) J. Snyder, P. Asanithi, A. B. Dalton, J. Erlebacher, *Adv. Mater.* **2008**, 20, 4883; b) C. Xu, R. Wang, Y. Zhang, Y. Ding, *Nanoscale* **2010**, 2, 906.
[41] M. Naguib, J. Come, B. Dyatkin, V. Presser, P.-L. Taberna, P. Simon, M. W. Barsoum, Y. J. E. C. Gogotsi, *Electrochem. Commun.* **2012**, 16, 61.
[42] S. K. Nemani, B. Zhang, B. C. Wyatt, Z. D. Hood, S. Manna, R. Khaledialidusti, W. Hong, M. G. Sternberg, S. Sankaranarayanan, B. Anasori, *ACS Nano* **2021**, 15, 12815.
[43] a) Z. Du, C. Wu, Y. Chen, Q. Zhu, Y. Cui, H. Wang, Y. Zhang, X. Chen, J. Shang, B. Li, W. Chen, C. Liu, S. Yang, *Adv. Energy Mater.* **2021**, 12, 2103228; b) Z. Du, C. Wu, Y. Chen, Z. Cao, R. Hu, Y. Zhang, J. Gu, Y. Cui, H. Chen, Y. Shi, J. Shang, B. Li, S. Yang, *Adv. Mater.* **2021**, 33, 2101473.
[44] a) H.-J. Qiu, G. Fang, Y. Wen, P. Liu, G. Xie, X. Liu, S. Sun, *J. Mater. Chem. A* **2019**, 7, 6499;

b) Z. Jin, J. Lyu, Y.-L. Zhao, H. Li, X. Lin, G. Xie, X. Liu, J.-J. Kai, H.-J. Qiu, *ACS Materials Lett.* **2020**, 2, 1698.
[45] S. Niu, Z. Yang, F. Qi, Y. Han, Z. Shi, Q. Qiu, X. Han, Y. Wang, X. Du, *Adv. Funct. Mater.* **2022**, 32, 2203787.
[46] Q. Wu, Z. Wang, F. He, L. Wang, J. Luo, J. Li, J. Wang, *Metall. Mater. Trans. A* **2018**, 49, 4986.
[47] a) G. W. Yang, *Prog. Mater. Sci.* **2007**, 52, 648; b) C. Schäfer, H. M. Urbassek, L. V. Zhigilei, *Phys. Rev. B* **2002**, 66, 115404.
[48] N. G. Semaltianos, *Crit. Rev. Solid State Mater. Sci.* **2010**, 35, 105.
[49] F. Waag, Y. Li, A. R. Ziefuss, E. Bertin, M. Kamp, V. Duppel, G. Marzun, L. Kienle, S. Barcikowski, B. Gokce, *RSC Adv.* **2019**, 9, 18547.
[50] H. Jahangiri, Y. Morova, A. Asghari Alamdari, Z. Eroğlu, A. Sennaroğlu, S. Guo, O. Metin, A. Motallebzadeh, *Intermetallics* **2023**, 156, 107834.
[51] A. Garzon-Manjon, H. Meyer, D. Grochla, T. Loffler, W. Schuhmann, A. Ludwig, C. Scheu, *Nanomaterials* **2018**, 8, 903.
[52] a) A. G. Manjon, T. Loffler, M. Meischein, H. Meyer, J. Lim, V. Strotkotter, W. Schuhmann, A. Ludwig, C. Scheu, *Nanoscale* **2020**, 12, 23570; b) T. Löffler, H. Meyer, A. Savan, P. Wilde, A. Garzón Manjón, Y. T. Chen, E. Ventosa, C. Scheu, A. Ludwig, W. Schuhmann, *Adv. Energy Mater.* **2018**, 8, 1802269.
[53] T. Wang, Q. He, J. Zhang, Z. Ding, F. Li, Y. Yang, *Mater. Today* **2020**, 36, 30.
[54] Y. Zhang, Y. J. Zhou, J. P. Lin, G. L. Chen, P. K. Liaw, *Adv. Eng. Mater.* **2008**, 10, 534.
[55] J. W. Yeh, S. K. Chen, S. J. Lin, J. Y. Gan, T. S. Chin, T. T. Shun, C. H. Tsau, S. Y. Chang, *Adv. Eng. Mater.* **2004**, 6, 299.
[56] P. Xie, Y. Yao, Z. Huang, Z. Liu, J. Zhang, T. Li, G. Wang, R. Shahbazian-Yassar, L. Hu, C. Wang, *Nat. Commun.* **2019**, 10, 4011.
[57] Y. Yao, Z. Huang, P. Xie, S. D. Lacey, R. Jacob, H. Xie, F. Chen, A. Nie, T. Pu, M. Rehwoldt, D. Yu, M. R. Zachariah, C. Wang, R. Shahbazian-Yassar, J. Li, L. Hu, *Science*, **2018**, 359, 1489–1494.
[58] K. Zeng, J. Zhang, W. Gao, L. Wu, H. Liu, J. Gao, Z. Li, J. Zhou, T. Li, Z. Liang, B. Xu, Y. Yao, *Adv. Funct. Mater.* **2022**, 32, 2204643.
[59] H. Qiao, M. T. Saray, X. Wang, S. Xu, G. Chen, Z. Huang, C. Chen, G. Zhong, Q. Dong, M. Hong, H. Xie, R. Shahbazian-Yassar, L. Hu, *ACS Nano* **2021**, 15, 14928.
[60] Y. Chu, R. Yu, G. He, T. Zhang, H. Dong, S. Deng, J. Li, *Sci. China Mater.* **2022**, 65, 3144.
[61] L. A. Chick, L. R. Pederson, G. D. Maupin, J. L. Bates, L. E.Thomas, G. J. Exarhos, *Mater. Lett.***1990**, 10, 6-12.
[62] a) C. Siriwong, S. Phanichphant, *Mater. Lett.* **2011**, 65, 2007; b) H. K. Kammler, L. Mädler, S. E. Pratsinis, *Chem. Eng. Technol.* **2001**, 24, 583; c) T. Rudin, K. Wegner, S. E. Pratsinis, *J. Nanopart. Res.* **2011**, 13, 2715.
[63] a) L. He, H. Kang, G. Hou, X. Qiao, X. Jia, W. Qin, X. Wu, *Chem. Eng. J.* **2023**, 460, 141675; b) L. M. Bui, S. T. Cam, I. V. Buryanenko, V. G. Semenov, D. V. Nazarov, P. E. Kazin, V. N. Nevedomskiy, E. Y. Gerasimov, V. I. Popkov, *Dalton Trans.* **2023**, 52, 4779.
[64] S. Zhu, Y. Chen, V. Somayaji, P. Novello, D. Chacko, F. Li, J. Liu, *ACS Appl. Mater. Interfaces* **2023**, 15, 31384.
[65] Z. Lin, B. Ma, Z. Chen, Y. Zhou, *Ceram. Int.* **2023**, 49, 23057.
[66] a) A. Moghtada, R. Ashiri, *Ultrason. Sonochem.* **2018**, 41, 127; b) A. Gedanken, *Ultrason.*

Sonochem. **2004**, 11, 47.
[67] A. Moghtada, A. Shahrouzianfar, R. Ashiri, *Adv. Powder Technol.* **2017**, 28, 1109.
[68] M. Liu, Z. Zhang, F. Okejiri, S. Yang, S. Zhou, S. Dai, *Adv. Mater. Interfaces* **2019**, 6, 1900015.
[69] F. Okejiri, Z. Yang, H. Chen, C.-L. Do-Thanh, T. Wang, S. Yang, S. Dai, *Nano Res.* **2021**, 15, 4792.
[70] a) K.-S. Kim, S. Choi, J.-H. Cha, S.-H. Yeon, H. Lee, *J. Mater. Chem.* **2006**, 16, 1315; b) F. Okejiri, Z. Zhang, J. Liu, M. Liu, S. Yang, S. Dai, *ChemSusChem* **2020**, 13, 111.
[71] a) A. Mao, P. Ding, F. Quan, T. Zhang, X. Ran, Y. Li, X. Jin, X. Gu, *J. Alloys Compd.* **2018**, 735, 1167; b) A. Mao, H. Xiang, X. Ran, Y. Li, X. Jin, H. Yu, X. Gu, *J. Alloys Compd.* **2019**, 775, 1177.
[72] Y. Liao, Y. Li, R. Zhao, J. Zhang, L. Zhao, L. Ji, Z. Zhang, X. Liu, G. Qin, X. Zhang, *Natl. Sci. Rev.* **2022**, 9, nwac041.
[73] J. Feng, D. Chen, P. V. Pikhitsa, Y.-h. Jung, J. Yang, M. Choi, *Matter* **2020**, 3, 1646.
[74] a) G. Zhu, Y. Jiang, H. Yang, H. Wang, Y. Fang, L. Wang, M. Xie, P. Qiu, W. Luo, *Adv. Mater.* **2022**, 34, 2110128; b) G. Feng, F. Ning, J. Song, H. Shang, K. Zhang, Z. Ding, P. Gao, W. Chu, D. Xia, *J. Am. Chem. Soc.* **2021**, 143, 17117; c) Y. Yao, Z. Li, Y. Dou, T. Jiang, J. Zou, S. Y. Lim, P. Norby, E. Stamate, J. O. Jensen, W. Zhang, *Dalton Trans.* **2023**, 52, 4142.
[75] D. Feng, Y. Dong, P. Nie, L. Zhang, Z.-A. Qiao, *Chem. Eng. J.* **2022**, 430, 132883.
[76] a) I. Liashenko, J. Rosell-Llompart, A. Cabot, *Nat. Commun.* **2020**, 11, 753; b) I. Liashenko, A. Ramon, A. Cabot, J. Rosell-Llompart, *Mater. Des.* **2021**, 206, 109791; c) S. Wang, G. Zeng, Q. Sun, Y. Feng, X. Wang, X. Ma, J. Li, H. Zhang, J. Wen, J. Feng, L. Ci, A. Cabot, Y. Tian, *ACS Nano* **2023**, 17, 13256; d) A. Ramon, I. Liashenko, J. Rosell-Llompart, A. Cabot, *Nanomaterials* **2024**, 14, 273; e) I. Liashenko, A. Ramon, J. Rosell-Llompart, A. Cabot, *Adv. Eng. Mater.* **2022**, 24, 2101804.
[77] J. Hao, Z. Zhuang, K. Cao, G. Gao, C. Wang, F. Lai, S. Lu, P. Ma, W. Dong, T. Liu, M. Du, H. Zhu, *Nat. Commun.* **2022**, 13, 2662.
[78] W. Li, Y. Sun, L. Ye, W. Han, F. Chen, J. Zhang, T. Zhao, *J. Am. Ceram. Soc.* **2022**, 105, 3729.
[79] M. Wei, J. Xu, R. Yang, J. Zhu, X. Meng, J. Yang, F. Gao, *J. Am. Ceram. Soc.* **2022**, 105, 4449.
[80] H. Wang, J. Xu, M. Wei, X. Feng, J. Wu, P. Zhang, F. Gao, *J. Am. Ceram. Soc.* **2024**, 107, 3857.
[81] S. Hou, X. Ma, Y. Shu, J. Bao, Q. Zhang, M. Chen, P. Zhang, S. Dai, *Nat. Commun.* **2021**, 12, 5917.
[82] H. Wei, Q. Wang, Y. Zhang, J. Li, P. Liu, N. Wang, X. Gong, *Fuel* **2024**, 358, 130011.
[83] H. Xu, Z. Zhang, J. Liu, C. L. Do-Thanh, H. Chen, S. Xu, Q. Lin, Y. Jiao, J. Wang, Y. Wang, Y. Chen, S. Dai, *Nat. Commun.* **2020**, 11, 3908.
[84] S. Zhao, P. Wei, L. Zhuang, H. Yu, Y. Chu, *Ceram. Int.* **2024**, 50, 31006.
[85] Y. Yang, B. Song, X. Ke, F. Xu, K. N. Bozhilov, L. Hu, R. Shahbazian-Yassar, M. R. Zachariah, *Langmuir* **2020**, 36, 1985.
[86] A. H. Phakatkar, M. T. Saray, M. G. Rasul, L. V. Sorokina, T. G. Ritter, T. Shokuhfar, R. Shahbazian-Yassar, *Langmuir* **2021**, 37, 9059.
[87] M. C. Heine, L. Mädler, R. Jossen, S. E. Pratsinis, *Combust. Flame* **2006**, 144, 809.
[88] W. Y. Teoh, R. Amal, L. Madler, *Nanoscale* **2010**, 2, 1324.
[89] R. Koirala, S. E. Pratsinis, A. Baiker, *Chem. Soc. Rev.* **2016**, 45, 3053.
[90] P.-C. Chen, X. Liu, J. L. Hedrick, Z. Xie, S. Wang, Q.-Y. Lin, M. C. Hersam, V. P. Dravid, C. A. Mirkin, *Science* **2016**, 352, 1565.

[91] C. Hegde, C. H. J. Lim, T. H. Teng, D. Liu, Y. J. Kim, Q. Yan, H. Li, *Small* **2022**, 18, 2203126.
[92] J. X. Yang, B. H. Dai, C. Y. Chiang, I. C. Chiu, C. W. Pao, S. Y. Lu, I. Y. Tsao, S. T. Lin, C. T. Chiu, J. W. Yeh, P. C. Chang, W. H. Hung, *ACS Nano* **2021**, 15, 12324.
[93] a) C. Suryanarayana, *Prog Mater Sci.* **2001**, 46,1-184; b) Y-S. Kwon, K. B. Gerasimov, S-K. Yoon, *J. Alloy Compd.* **2002**, 346276–281; c) A. Tonejc, M. Stubicar, A. M. Tonejc, *J. Mater. Sci. Lett.* **1994**, 13, 519; d) A. Tonejc, A. M. Tonejcm, D. Bagovic, *Mater. Sci. and Engng.* **1994**, A181/A182, 1227.
[94] Y. Wei, X. Liu, R. Yao, J. Qian, Y. Yin, D. Li, Y. Chen, *J. Alloys Compd.* **2023**, 938, 168610.
[95] Y. Zhang, W. Dai, P. Zhang, T. Lu, Y. Pan, *J. Alloys Compd.* **2021**, 868, 159064.
[96] R. Ashwini, M. K. P. Kumar, M. Y. Rekha, M. S. Santosh, C. Srivastava, *J. Alloys Compd.* **2022**, 903, 163846.
[97] Z. Yingzhe, C. Yudao, Q. Qingdong, L. Wei, *J. Magn. Magn. Mater.* **2020**, 498, 166151.
[98] G. R. Dey, C. R. McCormick, S. S. Soliman, A. J. Darling, R. E. Schaak, *ACS Nano* **2023**, 17, 5943.
[99] a) C. He, L. Yang, X. Peng, S. Liu, J. Wang, C. Dong, D. Du, L. Li, L. Bu, X. Huang, *ACS Nano* **2023**, 17, 5861; b) L. Yang, R. He, M. Botifoll, Y. Zhang, Y. Ding, C. Di, C. He, Y. Xu, L. Balcells, J. Arbiol, Y. Zhou, A. Cabot, *Adv. Mater.* **2024**, 36, e2400572; c) C. He, L. Yang, J. Wang, T. Wang, J. Ju, Y. Lu, W. Chen, *Carbon Energy* **2024**, 6, e573.
[100] a) P. R. Jothi, W. Liyanage, B. Jiang, S. Paladugu, D. Olds, D. A. Gilbert, K. Page, *Small* **2022**, 18, 2101323; b) S. Lee, L. Bai, J. Jeong, D. Stenzel, S. Schweidler, B. Breitung, *Electrochim. Acta* **2023**, 463, 142775; c) T. X. Nguyen, Y. C. Liao, C. C. Lin, Y. H. Su, J. M. Ting, *Adv. Funct. Mater.* **2021**, 31, 2101632; d) D. Lai, Q. Kang, F. Gao, Q. Lu, *J. Mater. Chem. A* **2021**, 9, 17913; e) M. Kheradmandfard, H. Minouei, N. Tsvetkov, A. K. Vayghan, S. F. Kashani-Bozorg, G. Kim, S. I. Hong, D.-E. Kim, *Mater. Chem. Phys.* **2021**, 262, 124265; f) T. X. Nguyen, J. Patra, J.-K. Chang, J.-M. Ting, *J. Mater. Chem. A* **2020**, 8, 18963; g) Y.-J. Liao, W.-W. Shen, C.-B. Chang, H.-Y. Tuan, *Chem. Eng. J.* **2023**, 469, 143942.
[101] B. Talluri, K. Yoo, J. Kim, *J. Environ. Chem. Eng.* **2022**, 10, 106932.
[102] S. Gao, S. Hao, Z. Huang, Y. Yuan, S. Han, L. Lei, X. Zhang, R. Shahbazian-Yassar, J. Lu, *Nat. Commun.* **2020**, 11, 2016.
[103] C. Xing, L. Yang, R. He, M. C. Spadaro, Y. Zhang, J. Arbiol, J. Li, B. Poudel, A. Nozariasbmarz, W. Li, K. H. Lim, Y. Liu, J. Llorca, A. Cabot, *Small* **2023**, 19, e2303639.
[104] a) M. P. Singh, C. Srivastava, *Mater. Lett.* **2015**, 160, 419; b) Y. Yu, F. Xia, C. Wang, J. Wu, X. Fu, D. Ma, B. Lin, J. Wang, Q. Yue, Y. Kang, *Nano Res.* **2022**, 15, 7868; c) Y. Chen, X. Zhan, S. L. A. Bueno, I. H. Shafei, H. M. Ashberry, K. Chatterjee, L. Xu, Y. Tang, S. E. Skrabalak, *Nanoscale Horiz.* **2021**, 6, 231; d) Y. Maruta, K. Kusada, D. Wu, T. Yamamoto, T. Toriyama, S. Matsumura, O. Seo, S. Yasuno, S. Kawaguchi, O. Sakata, Y. Kubota, H. Kitagawa, *Chem. Commun.* **2022**, 58, 6421; e) C. M. D. Silva, H. Amara, F. Fossard, A. Girard, A. Loiseau, V. Huc, *Nanoscale* **2022**, **14**, 9832-9841; f) K. Kusada, T. Yamamoto, T. Toriyama, S. Matsumura, K. Sato, K. Nagaoka, K. Terada, Y. Ikeda, Y. Hirai, H. Kitagawa, *J. Phys. Chem. C* **2020**, 125, 458.
[105] D. Wu, K. Kusada, T. Yamamoto, T. Toriyama, S. Matsumura, S. Kawaguchi, Y. Kubota, H. Kitagawa, *J. Am. Chem. Soc.* **2020**, 142, 13833.
[106] D. Wu, K. Kusada, T. Yamamoto, T. Toriyama, S. Matsumura, I. Gueye, O. Seo, J. Kim, S. Hiroi, O. Sakata, S. Kawaguchi, Y. Kubota, H. Kitagawa, *Chem. Sci.* **2020**, 11, 12731.
[107] D. Wu, K. Kusada, Y. Nanba, M. Koyama, T. Yamamoto, T. Toriyama, S. Matsumura, O. Seo,

I. Gueye, J. Kim, L. S. Rosantha Kumara, O. Sakata, S. Kawaguchi, Y. Kubota, H. Kitagawa, *J. Am. Chem. Soc.* **2022**, 144, 3365.
[108] J. Sun, A. Leff, Y. Li, T. J. Woehl, *Nanoscale* **2023**, 15, 10447.
[109] N. L. N. Broge, M. Bondesgaard, F. Sondergaard-Pedersen, M. Roelsgaard, B. B. Iversen, *Angew. Chem. Int. Ed.* **2020**, 59, 21920.
[110] H. Minamihara, K. Kusada, D. Wu, T. Yamamoto, T. Toriyama, S. Matsumura, L. S. R. Kumara, K. Ohara, O. Sakata, S. Kawaguchi, Y. Kubota, H. Kitagawa, *J. Am. Chem. Soc.* **2022**, 144, 11525.
[111] G. Lee, N.-A. Nguyen, V.-T. Nguyen, L. L. Larina, E. Chuluunbat, E. Park, J. Kim, H.-S. Choi, M. Keidar, *J. Solid State Chem.* **2022**, 314, 123388.
[112] D. Wu, L. Yao, M. Ricci, J. Li, R. Xie, Z. Peng, *Chem. Mater.* **2021**, 34, 266.
[113] a) A. Aliyu, C. Srivastava, *Surf. Coat. Tech.* **2022**, 429, 127943; b) H. Bian, R. Wang, K. Zhang, H. Zheng, M. Wen, Z. Li, Z. Li, G. Wang, G. Xie, X. Liu, L. Jiang, *Surf. Coat. Tech.* **2023**, 459, 129407.
[114] T. G. Ritter, A. H. Phakatkar, M. G. Rasul, M. T. Saray, L. V. Sorokina, T. Shokuhfar, J. M. Gonçalves, R. Shahbazian-Yassar, *Cell Rep. Phys. Sci.* **2022**, 3, 100847.
[115] W. Dong, Q. Pan, Z. Liu, H. Sun, Z. Shi, J. Xu, *Int. J. Hydrogen Energy* **2023**, 48, 35493.
[116] Z. Zhu, H. Meng, P. Ren, *Colloids Surf. A: Physicochem. Eng. Aspects* **2022**, 648, 129404.
[117] M. W. Glasscott, A. D. Pendergast, S. Goines, A. R. Bishop, A. T. Hoang, C. Renault, J. E. Dick, *Nat. Commun.* **2019**, 10, 2650.
[118] Y.-H. Liu, C.-J. Hsieh, L.-C. Hsu, K.-H. Lin, Y.-C. Hsiao, C.-C. Chi, J.-T. Lin, C.-W. Chang, S.-C. Lin, C.-Y. Wu, J.-Q. Gao, C.-W. Pao, Y.-M. Chang M.-Y. Lu, S. Zhou, T.-H. Yang, *Sci. Adv.* **2023**, 9, eadf9931.
[119] F. Calvo, *Phys. Chem. Chem. Phys.* **2023**, 25, 18439.
[120] a) M. Ibáñez, R. Zamani, A. LaLonde, D. Cadavid, W. Li, A. Shavel, J. Arbiol, J. R. Morante, S. Gorsse, G. J. Snyder, A. Cabot, *J. Am. Chem. Soc.* **2012**, 134, 4060.
[121] W. Chen, S. Luo, M. Sun, X. Wu, Y. Zhou, Y. Liao, M. Tang, X. Fan, B. Huang, Z. J. A. M. Quan, **2022**, 34, 2206276.
[122] Y. Wang, W. Luo, S. Gong, L. Luo, Y. Li, Y. Zhao, Z. Li, *Adv. Mater.* **2023**, 35, 2302499.
[123] C. R. McCormick, R. E. Schaak, *J. Am. Chem. Soc.* **2021**, 143, 1017.
[124] L. De Trizio, L. Manna, *Chem. Rev.* **2016**, 116, 10852.
[125] X. Wan, R. Zeng, X. Wang, H. Wang, Q. Wei, D. Tang, *Biosens. Bioelectron.* **2023**, 237, 115535.
[126] a) X. Xia, Y. Wang, A. Ruditskiy, Y. Xia, *Adv. Mater.* **2013**, 25, 6313; b) Y. Hong, S. Venkateshalu, S. Jeong, G. M. Tomboc, J. Jo, J. Park, K. Lee, *B. Korean Chem. Soc.* **2022**, 44, 4; c) H. Cheng, C. Wang, D. Qin, Y. Xia, *Acc. Chem. Res.* **2023**, 56, 900.
[127] L. Tao, M. Sun, Y. Zhou, M. Luo, F. Lv, M. Li, Q. Zhang, L. Gu, B. Huang, S. Guo, *J. Am. Chem. Soc.* **2022**, 144, 10582.
[128] T. Loffler, A. Savan, H. Meyer, M. Meischein, V. Strotkotter, A. Ludwig, W. Schuhmann, *Angew. Chem. Int. Ed. Engl.* **2020**, 59, 5844.
[129] C. Zhan, L. Bu, H. Sun, X. Huang, Z. Zhu, T. Yang, H. Ma, L. Li, Y. Wang, H. Geng, W. Wang, H. Zhu, C. W. Pao, Q. Shao, Z. Yang, W. Liu, Z. Xie, X. Huang, *Angew. Chem. Int. Ed. Engl.* **2023**, 62, 202213783.
[130] a) J. Johny, Y. Li, M. Kamp, O. Prymak, S.-X. Liang, T. Krekeler, M. Ritter, L. Kienle, C. Rehbock, S. Barcikowski, S. Reichenberger, *Nano Res.* **2021**, 15, 4807; b) T. Loffler, A.

Ludwig, J. Rossmeisl, W. Schuhmann, *Angew. Chem. Int. Ed. Engl.* **2021**, 60, 26894.
[131] a) G. Gao, Y. Yu, G. Zhu, B. Sun, R. He, A. Cabot, Z. Sun, *J. Energy Chem.* **2024**, 99, 335; b) A. Ostovari Moghaddam, S. Mehrabi-Kalajahi, X. Qi, R. Salari, R. Fereidonnejad, A. Abdollahzadeh, D. A. Uchaev, E. A. Kazakova, M. A. Varfolomeev, A. Cabot, A. S. Vasenko, E. A. Trofimov, *J. Phys. Chem. Lett.* **2024**, 15, 7577; c) A. Ostovari Moghaddam, S. Mehrabi-Kalajahi, A. Abdollahzadeh, R. Salari, X. Qi, R. Fereidonnejad, S. A. Akaahimbe, M. Nangir, D. A. Uchaev, M. A. Varfolomeev, A. Cabot, A. S. Vasenko, E. A. Trofimov, *J. Phys. Chem. Lett.* **2024**, 15, 5535; d) S. Mehrabi-Kalajahi, A. Ostovari Moghaddam, F. Hadavimoghaddam, R. Salari, M. A. Varfolomeev, A. L. Zinnatullin, K. R. Minnebaev, D. A. Emelianov, D. A. Uchaev, R. Fereidonnejad, O. Zaitseva, G. R. Khasanova, E. A. Trofimov, A. Rozhenko, A. Cabot, F. G. Vagizov, *ACS Appl. Nano Mater.* **2024**, 7, 5513; e) ; f) Z. Shi, L. Wang, Y. Huang, X. Y. Kong, L. Ye, *Mater. Chem. Front.* **2024**, 8, 179.
[132] a) B. Song, Y. Yang, M. Rabbani, T. T. Yang, K. He, X. Hu, Y. Yuan, P. Ghildiyal, V. P. Dravid, M. R. Zachariah, W. A. Saidi, Y. Liu, R. Shahbazian-Yassar, *ACS Nano* **2020**, 14, 15131; b) J. Gao, J. Ding, Y. Zhang, T. Zhu, Q. Yu, *Nano Res.* **2021**, 15, 3569; c) H. Bai, R. Su, R. Z. Zhao, C. L. Hu, L. Z. Ji, Y. J. Liao, Y. N. Zhang, Y. X. Li, X. F. Zhang, *J. Mater. Sci. Technol.* **2024**, 177, 133; d) B. Song, Y. Yang, T. T. Yang, K. He, X. Hu, Y. Yuan, V. P. Dravid, M. R. Zachariah, W. A. Saidi, Y. Liu, R. Shahbazian-Yassar, *Nano Lett.* **2021**, 21, 1742.
[133] a) R. Nafria, A. Genc, M. Ibanez, J. Arbiol, P. R. de la Piscina, N. Homs, A. Cabot, *Langmuir* **2016**, 32, 2267; b) Z. Luo, J. Lu, C. Flox, R. Nafria, A. Genç, J. Arbiol, J. Llorca, M. Ibáñez, J. R. Morante, A. Cabot, *J. Mater. Chem. A* **2016**, 4, 16706; c) Q. Wang, J. Liu, T. Li, T. Zhang, J. Arbiol, S. Yan, Y. Wang, H. Li, A. Cabot, *Chem. Eng. J.* **2022**, 446, 136878.
[134] X. Fu, J. Zhang, S. Zhan, F. Xia, C. Wang, D. Ma, Q. Yue, J. Wu, Y. Kang, *ACS Catal.* **2022**, 12, 11955.
[135] A. L. Maulana, P. C. Chen, Z. Shi, Y. Yang, C. Lizandara-Pueyo, F. Seeler, H. D. Abruna, D. Muller, K. Schierle-Arndt, P. Yang, *Nano Lett.* **2023**, 23, 6637.
[136] F. Zhang, C. Zhang, S. L. Chen, J. Zhu, W. S. Cao, U. R. Kattner, *Calphad* **2014**, 45, 1.
[137] a) A. Ostovari Moghaddam, A. Cabot, E. A. Trofimov, *Int. J. Refract. Met. Hard Mater.* **2021**, 97, 105504; b) B. Jiang, Y. Yu, J. Cui, X. Liu, L. Xie, J. Liao, Q. Zhang, Y. Huang, S. Ning, B. Jia, B. Zhu, S. Bai, L. Chen, S. J. Pennycook, J. He, *Science* **2021***,* 371, 830–834; c) M. G. Kanatzidis, *Materials Lab* **2022**, 1, 220052.
[138] a) B. Ward-O'Brien, P. D. McNaughter, R. Cai, A. Chattopadhyay, J. M. Flitcroft, C. T. Smith, D. J. Binks, J. M. Skelton, S. J. Haigh, D. J. Lewis, *Nano Lett.* **2022**, 22, 8045; b) D. Shin, B. Saparov, D. B. Mitzi, *Adv. Energy Mater.* **2017**, 7, 1602366.
[139] K. Sugita, R. Ogawa, M. Mizuno, H. Araki, A. Yabuuchi, *Scripta Mater.* **2022**, 208, 114339.
[140] K. Mori, N. Hashimoto, N. Kamiuchi, H. Yoshida, H. Kobayashi, H. Yamashita, *Nat. Commun.* **2021**, 12, 3884.
[141] B. Cantor, *Entropy* **2014**, 16, 4749.
[142] a) O. N. Senkov, J. D. Miller, D. B. Miracle, C. Woodward, *Nat. Commun.* **2015**, 6, 6529; b) A. Abu-Odeh, E. Galvan, T. Kirk, H. Mao, Q. Chen, P. Mason, R. Malak, R. Arróyave, *Acta Mater.* **2018**, 152, 41; c) A. Anand, S. J. Liu, C. V. Singh, *iScience* **2023**, 26, 107751.
[143] Y. Yao, Z. Huang, T. Li, H. Wang, Y. Liu, H. S. Stein, Y. Mao, J. Gao, M. Jiao, Q. Dong, J. Dai, P. Xie, H. Xie, S. D. Lacey, I. Takeuchi, J. M. Gregoire, R. Jiang, C. Wang, A. D. Taylor, R. Shahbazian-Yassar, L. Hu, *Proc. Natl. Acad. Sci. USA* **2020**, 117, 6316.
[144] L. Banko, E. B. Tetteh, A. Kostka, T. H. Piotrowiak, O. A. Krysiak, U. Hagemann, C.

Andronescu, W. Schuhmann, A. Ludwig, *Adv. Mater.* **2023**, 35, 2207635.
[145] a) Y. Xie, K. Sattari, C. Zhang, J. Lin, *Prog. Mater. Sci.* **2023**, 132, 101043; b) E. Stach, B. DeCost, A. G. Kusne, J. Hattrick-Simpers, K. A. Brown, K. G. Reyes, J. Schrier, S. Billinge, T. Buonassisi, I. Foster, C. P. Gomes, J. M. Gregoire, A. Mehta, J. Montoya, E. Olivetti, C. Park, E. Rotenberg, S. K. Saikin, S. Smullin, V. Stanev, B. Maruyama, *Matter.* **2021**, 4, 2702.
[146] a) E. M. Williamson, R. L. Brutchey, *Inorg. Chem.* **2023**, 62, 16251; b) X. Wan, Z. Li, W. Yu, A. Wang, X. Ke, H. Guo, J. Su, L. Li, Q. Gui, S. Zhao, J. Robertson, Z. Zhang, Y. Guo, *Adv. Mater.* **2023**, 2305192; c) X. Liu, J. Zhang, Z. Pei, *Prog. Mater. Sci.* **2023**, 131, 101018; d) S. Singh, N. K. Katiyar, S. Goel, S. N. Joshi, *Sci. Rep.* **2023**, 13, 4811; e) Z. Rao, P-Y. Tung, R. Xie, Y. Wei, H. Zhang, A. Ferrari, T. P. C. Klaver, F. Körmann, P. T. Sukumar, A. K. Silva, Y. Chen, Z. Li, D. Ponge, J. Neugebauer, O. Gutfleisch, S. Bauer, D. Raabe, *Science* **2022**, 378, 78–85.

7. Acknowledgements

This work was financially supported by the SyDEC at project from the Spanish MCIN/AEI/FEDER (PID2022-136883OB-C22). The authors acknowledge funding from Generalitat de Catalunya 2021SGR01581 and European Union NextGenerationEU/PRTR. L. L.Yang, J. L. Chai, X. Y. Bi and J. Yu thank the China Scholarship Council (CSC) for the scholarship support.